An Integrated Capacitive Brushless Excitation System for Wound Field Synchronous Machines Using Low-Cost Printed Circuit Boards

by

Skyler Hagen

A dissertation submitted in partial fulfillment of the requirements for the degree of

Doctor of Philosophy

(Electrical Engineering)

at the

UNIVERSITY of WISCONSIN - MADISON

2019

Date of final oral examination: 12/02/2019

The dissertation is approved by the following members of the Final Oral Committee:

1. Daniel Ludois (advisor) – Associate Professor – ECE
2. Giri Venkataramanan – Professor – ECE
3. Bulent Sarlioglu – Associate Professor – ECE
4. Eric Severson – Assistant Professor – ECE, ME

Abstract

With the current proliferation of electric machines taking over roles that were historically performed by mechanical transmissions and combustion engines, strides are being taken to make electric machines more power and torque dense, as well as less expensive.

The wound field synchronous machine (WFSM) has advantages in power density, controllability, as well as cost of manufacturing, over other types including induction machines and permanent magnet synchronous machines [1], [2]. Its use for vehicle and traction applications has been limited due to the requirement of electrical power on the rotor field windings throughout the machine's entire range of speed, including stall.

Field excitation requirements at stall and low speeds prohibit the use of conventional brushless exciters, commonly used in gen-sets, which rely on shaft rotation and torque to produce field current. Gapped rotating electromagnetic transformers allow excitation at stall but suffer from complexity of manufacturing and added volume to accommodate the ferrous core materials required to complete a magnetic circuit. All contactless field excitation methods require a rotating rectifier diode board or assembly to be installed on the rotor, alongside the brushless exciter or rotating transformer, in order to provide direct current to the field winding, from a contactless power coupler which is inherently alternating current.

Capacitive power transfer (CPT) has been shown to be competitive with inductive power transfer in supplying full field excitation to wound rotor synchronous machines [1]–[3]. In this thesis, a capacitive power transfer system is described in which the rotating rectifier board, manufactured using conventional printed circuit board techniques, dual-purposes as the capacitive power coupling structure, resulting in an efficient, low cost and compact means for transferring kilowatt

scale electrical power to a wound field synchronous machine. A design process for the capacitive coupler itself in conjunction with necessary passive components and controls is laid out, and experimental results are given for a CPT system being used to provide full field excitation to a 55kW WFSM.

Acknowledgements

I would like to thank my advisor, Professor Daniel Ludois, for his continued guidance and support through the course of my research work here at UW Madison the last few years. Unlike most students in our graduate program, I did not enter with an electrical or mechanical engineering degree. Professor Ludois showed me how to apply my educational background in physics and mathematics to solving complex multidisciplinary electrical and mechanical engineering problems and helped me develop a broad skill set for approaching these engineering challenges that will benefit me throughout my career.

I also extend my gratitude to the faculty, staff, and students in the Wisconsin Electric Machines and Power Electronics Consortium (WEMPEC). Their family-like community, wealth of knowledge, and advanced laboratory facilities have provided an excellent atmosphere in which to carry out the work that has led up to the research presented in this thesis.

Finally, my deepest appreciation goes to my family, and especially to my parents Dr. Ethan and Lynn Hagen. Over the years they have taught and reinforced the importance of hard work, good morals, and the ability to collaborate effectively with others. Their constant support has been the driving force that has gotten me where I am today.

"the book of nature, which we have to read, is written by the finger of God."

Sir Michael Faraday, 1859

Table of Contents

List of Figures

List of Tables

Nomenclature

I, I_{ac}	current, alternating current (amperes)
C	capacitance (farad, picofarad)
I_{peak}	peak ac current (amperes)
E	electric field (V/m)
V_{in}, V_{out}	input voltage, output voltage (volts)
R	resistance (ohms)
Z	Impedance (ohms)
ε, ε_o	permittivity, permittivity of free space (farad/meter)
ε_r , K	relative permittivity/dielectric constant (dimensionless)
f	frequency (hertz, megahertz)
A	area of capacitor electrode overlap (m^2)
V_C	coupling capacitor voltage (volts)
g	coupler gap thickness (inches)
d	Radial distance between coupling electrodes (inches)
r_o	electrode outer radius (inches)
r_i	electrode inner radius (inches)
D	displacement field intensity (coulombs/$meter^2$)
$D.F.$, D_f	dissipation factor (unitless)
D_{buck}	Buck converter duty ratio (unitless, or may be expressed as %)

Chapter 1 Motivation and Review of Capacitive Power Transfer

1.1 WFSM Rotational Power Coupling Requirement

In a wound field synchronous machine (WFSM), kilowatt scale electrical power is required on the rotating field winding to develop the magnetic field necessary for torque production. In vehicle traction applications specifically, this field winding must be able to receive full power whether the rotor shaft is stationary or spinning at a wide range of speeds in either rotational direction.

This thesis will focus on a method for powering the rotating field winding which uses capacitive power transfer (CPT). Examples of non-capacitive rotational coupling methods will be reviewed first in this chapter. Next, the state of the art in capacitive power transfer will be discussed. Capacitive power transfer examples for both rotational (as is the topic of this thesis) and stationary power transfer applications will be given, in order to cover the full breadth of power transfer levels to which CPT has been applied.

1.1.1 Alternatives to CPT for Rotational Power Transfer

Carbon brushes and slip rings, as shown in Figure 1-1, are a simple low cost solution for transferring power to a rotating electrical load [4]. Unfortunately, because the brush-slip ring interface experiences friction during rotation, the brushes wear and require periodic replacement. Brush excitation of synchronous machines still finds use in low-cost low-power applications such as charging system alternators in internal combustion engine vehicles. However, the problem of brush wear excludes them from use in high-reliability, high-longevity, and low-maintenance

applications such as electric vehicle traction motors, or aircraft power generation. It is clear from the maintenance requirements of brushes and slip rings that some form of brushless field excitation method is needed.

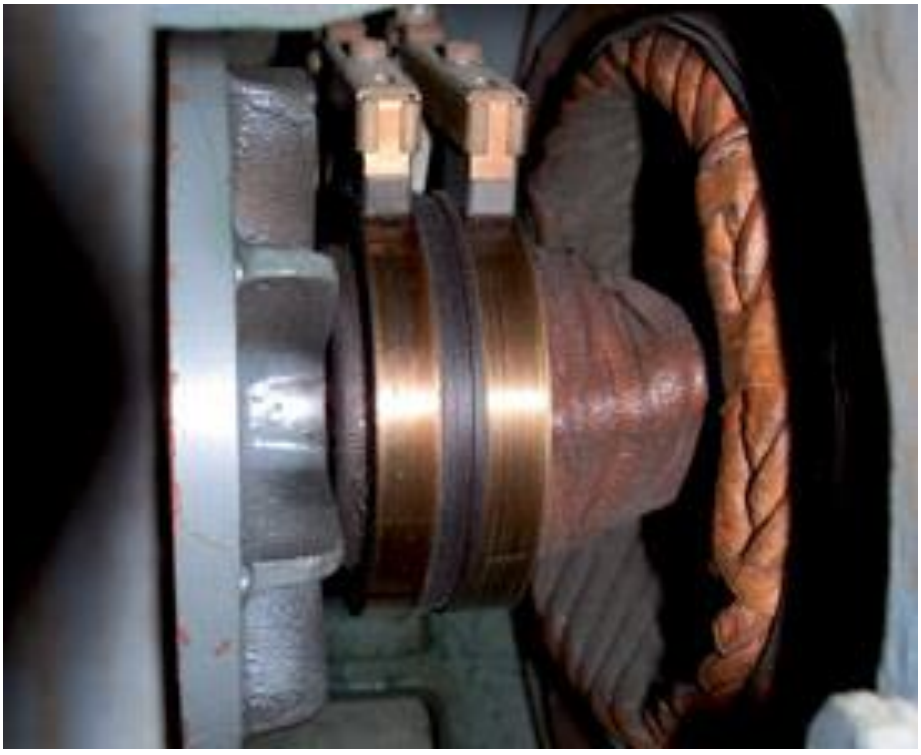

Figure 1-1: Photograph of carbon brushes sliding on rotating slip rings. [5]

An exhaustive review of WFSM field excitation methods was carried out in [6]. While [6] covers a wide range of WFSM applications, ranging from kW to multi-MW power levels, the focus of this thesis is on the use of WFSM's for electric vehicle traction applications. Before discussing the use of capacitive power transfer for WFSM excitation, several electromagnetic brushless excitation methods relevant to the rotational speeds and power levels seen in typical traction WFSM's will be discussed here.

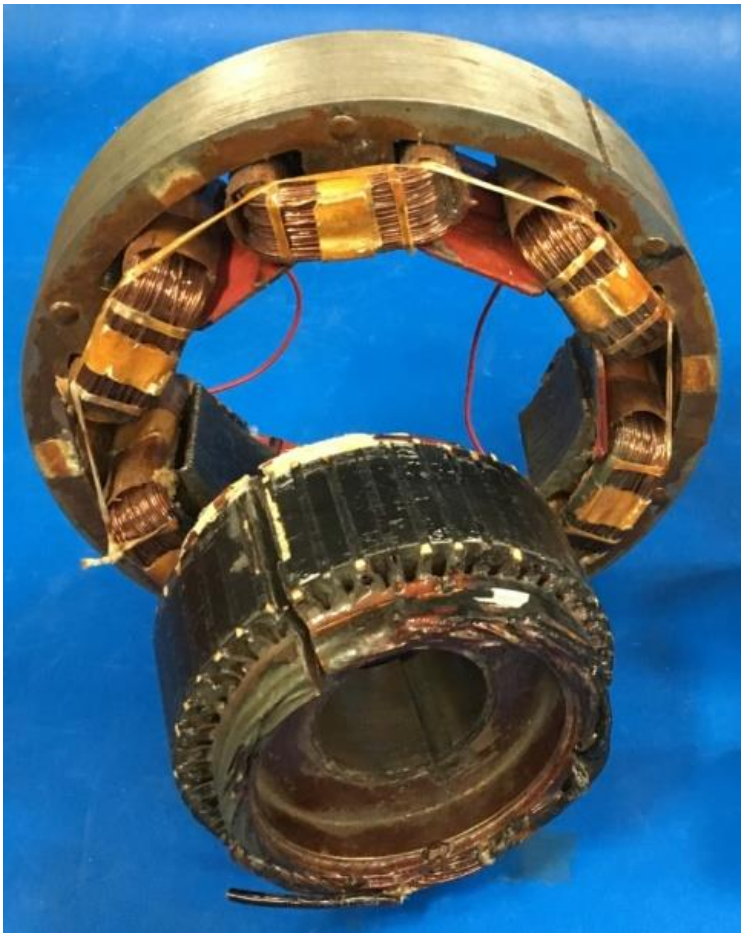

Figure 1-2: Conventional shaft driven brushless exciter, stator (rear) and rotor (front). Separate rotating diode board not shown.

Electromagnetic means for contactless energy transfer have existed for many years [7]. Among the most common methods used (since the advent of reliable solid state rectifying diodes) is the use of a shaft driven electromagnetic brushless exciter [8]–[10]. Traditional brushless exciters as shown in Figure 1-2 add a great deal of weight and volume to the overall machine, due to their use of steel laminations and copper windings [11]. The most basic form of brushless exciter, of the type used on portable generator sets (as shown in Figure 1-2) requires rotation to generate rotor field current. It converts mechanical shaft power into electrical field power, rather than sourcing

the excitation power externally, so it cannot be used under stall and low speed conditions. Though this type of brushless exciter is capable of the field power levels required in traction WFSM's, the inability to provide field power at stall and low speed prevents its use in traction drives.

More advanced systems, for example those used in the aircraft starter/generator applications discussed in [8], [9], [12] are able to source power externally and excite the field at stall. The three stage synchronous machine topology, shown in the diagram of Figure 1-3 utilizes three separate machine sections, mounted on a common rotating shaft to accomplish this goal. A control unit supplies alternating current from an external power source to the field winding of the main exciter section. At stall, such as during startup, this alternating current provides an alternating magnetic field which couples to the main exciter rotor windings. The induced AC voltage on the main exciter armature is then rectified by a rotating diode bridge to feed the main field winding. Once rotating, the permanent magnet pre-exciter section is able to source the power required for the main exciter field, at which point the external power source is no longer necessary.

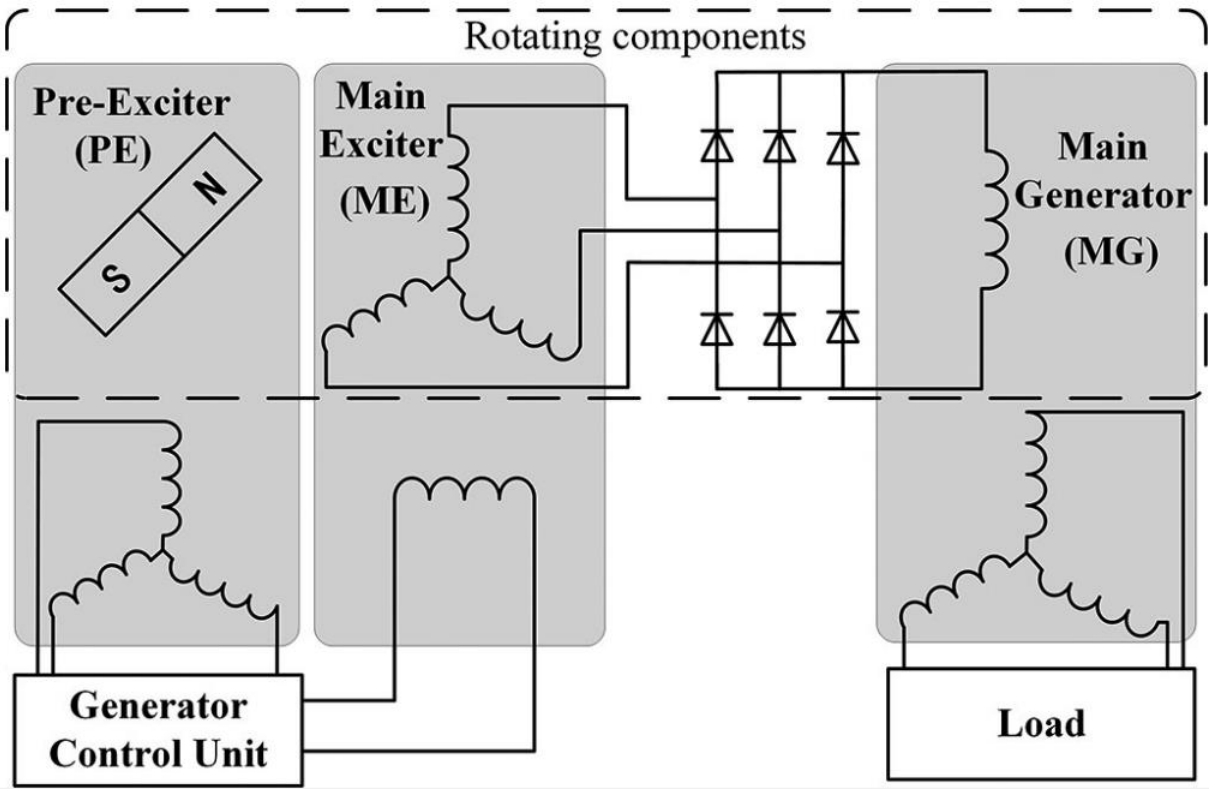

Figure 1-3: Schematic of three-stage brushless excitation system for a wound field synchronous machine [8].

Though such systems can excite the main field winding at zero rotational speed, as required by traction drive applications, they do still require laminations and several additional windings to be added to the WFSM. The necessity of three individual electric machines located along a common shaft increases the length and overall volume/weight of the machine.

With more recent advances in wide bandgap semiconductor technology, high power and high frequency gapped transformers (both large and small gap) have been used in contactless power transfer for electric vehicle charging [13]–[19], mobile electronics charging [20], [21], and, as shown in Figure 1-4, excitation of WFSM field windings or other rotating loads [22]–[26].

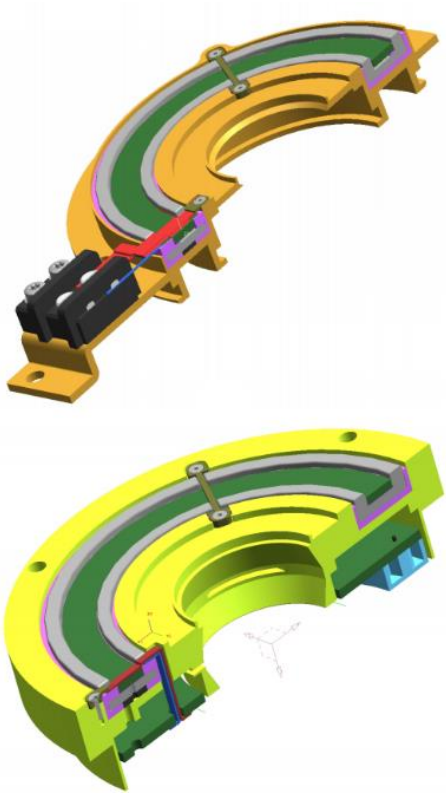

Figure 1-4: Computer rendering of a high frequency gapped rotating electromagnetic transformer, for wound field synchronous machine excitation [27].

Fundamental requirements of magnetic circuits require permeable core materials to form a closed path for magnetic flux to flow between the primary and secondary side of the transformer. These high frequency transformers, when used for rotating applications may also require complex copper winding designs in order to efficiently transfer energy across the gap. Placing the required magnetic core materials on rotating shafts potentially limits the shaft rotational speed, due to centrifugal forces acting on fragile powdered iron or ferrite core materials.

One additional electromagnetic brushless excitation method in [28] involves the switching of thyristors connected across WFSM stator windings to inject a spatial third harmonic current

component into the stator winding of a WFSM. This third harmonic current component electromagnetically couples to special windings (additional to the main field winding) located on the rotor, where it is rectified to feed the main field winding as shown in Figure 1-5. However, because this method requires extra windings on the rotor, it sacrifices copper cross section in the machine which could otherwise be used for torque production.

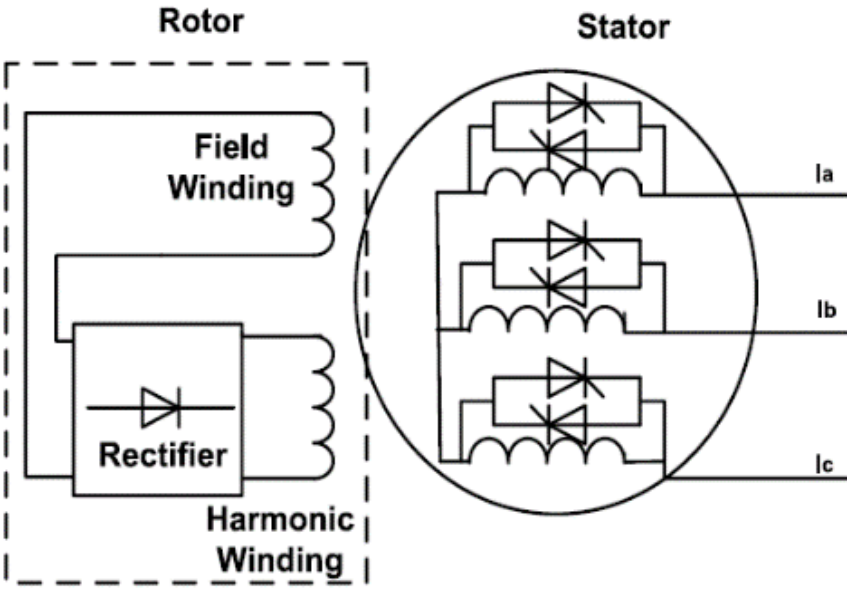

Figure 1-5: Method for contactless field excitation by transformer-coupling stator 3rd harmonic current content to the an additional winding on the rotor [28].

1.1.2 Motivation for the Use of Capacitive Power Transfer

A system that can be manufactured inexpensively, is mechanically robust at high speeds, and has comparatively small volume, without sacrificing system efficiency, would be a desirable option for wound field synchronous machine rotor excitation.

Electromagnetic brushless excitation systems have low characteristic impedance when compared to similar power level capacitive systems which makes their output well-suited for direct connection (through a rectifier) to low impedance loads like the WFSM field winding. However, it will be shown that with the proper secondary/power-receiving side power electronics, capacitive coupling systems can easily be impedance-matched to low impedance loads without adding much additional component cost or bulk to the system.

All the above-mentioned electromagnetic brushless excitation systems require a rotating rectifier board mounted on the same shaft as the magnetic field coupling structures. It will be shown in the following chapters that by using capacitive power coupling, rather than electromagnetic coupling, the printed circuit board that houses the rotating rectifier functionality can be dual purposed as the electric field coupling structure. The result is a compact, lightweight and fully integrated brushless exciter assembly using only low cost printed circuit boards for its construction.

1.2 Review of Capacitive Power Coupling

1.2.1 Beginnings of Capacitive Power Transfer

Electrostatic (capacitive) energy transfer research extends back to the early days of electrification, when Nikola Tesla demonstrated the illumination of gas discharge lamps in an alternating electric field in 1891 [29]. Due to the comparatively low frequencies available from rotating ac generators and mechanically switched pulse generators during Tesla's time, extremely high voltages were required to demonstrate this type of capacitive power transfer, making the technology unsuitable for practical use, especially from a safety perspective. After Tesla's time, capacitive power transfer development was relatively dormant until the twenty first century when solid state electronic component technology caught up with the frequencies and voltages required in order to make capacitive power transfer practical. Around 2008, some preliminary experiments into capacitive power transfer occurred [30], which sparked a great deal of additional research into the topic in the decade to follow [31].

1.2.2 Fundamental Concepts of Capacitive Power Transfer

The basic components of a capacitive power transfer system are laid out in Figure 1-6. An input voltage V_{in} represents the power source feeding the system. The primary electronics convert input power (usually in the form of DC) to a high frequency alternating voltage which is applied to the primary-side coupling electrodes (center of Figure 1-6). The coupling capacitor structure itself provides the most variety and diversity between different capacitive power transfer systems, as will be seen in later sections. Because capacitors have low impedance at high frequency, the

coupling capacitors form an effective path for alternating current to flow between the primary and secondary side of the circuit. The secondary side of the coupler capacitor structure is then connected to secondary power electronics. This usually consists of a fast switching rectifier along with any filter and power conditioning components that may be required based on the characteristics of the load. This same general setup is used in all capacitive coupling schemes.

Typically, inductors or other passive components are included in the output stage of the primary electronics and/or input stages of the secondary electronics. These passive matching components, when properly tuned for the desired operating frequency, greatly reduce the series impedance that exists between the primary and secondary power converters, by forming a resonant link. The resonant circuit also results in near-unity power factor at the primary converter output and secondary converter input, which reduces switching losses in the respective semiconductor components, typically through zero current switching for h-bridge systems. The specific physical construction of the coupling capacitors, as well as the details of the primary and secondary electronics, along with inductors or other matching components differ between different power electronic designs [32].

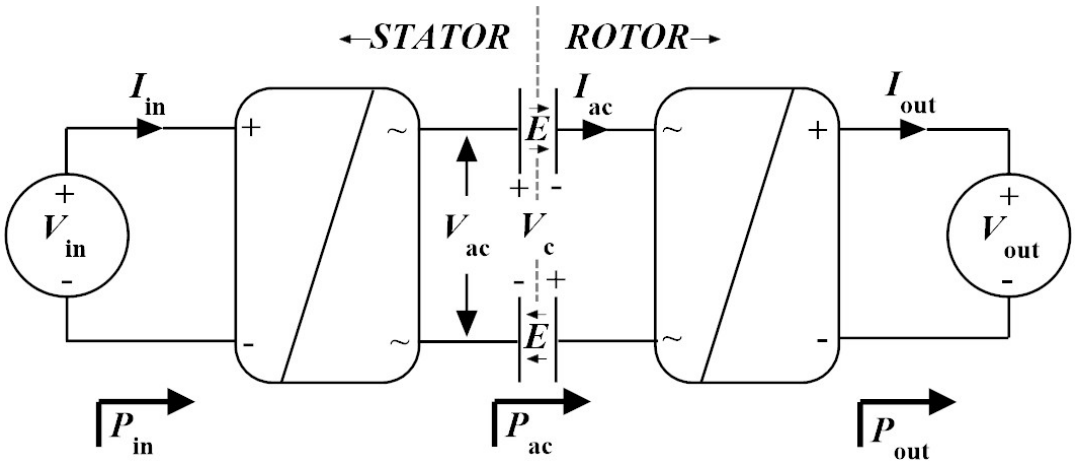

Figure 1-6: Basic conceptual diagram for capacitive power transfer, with key electrical quantities labelled.

1.2.2.1 Amps Per MHz Limitation

A given capacitive power coupler structure has a maximum allowable electric field that can exist between opposing capacitor electrodes, depending on the dielectric material that lies between them, which if exceeded would result in arc breakdown and damage to the coupler. The electric field E in the coupler gap is given as

$$E = \frac{V_c}{g} \tag{1.1}$$

where V_c is the voltage across the coupling capacitor, and g is the physical gap distance between the primary and secondary side capacitor electrodes. Capacitor voltage V_c can be expressed in terms of current I_{ac}, frequency ω, and capacitance C, where RMS or Peak quantities can be used as needed.

$$V_c = I_{ac}X_c = \frac{I_{ac}}{\omega C} \tag{1.2}$$

Based on the coupling electrode area A, gap g, and dielectric permittivity ϵ, the quantity $1/C$ can be found to be:

$$C = \frac{A\epsilon}{g} \quad \rightarrow \quad \frac{1}{C} = \frac{g}{A\epsilon}. \tag{1.3}$$

Combining (1.2) and (1.3) the expression for V_c becomes:

$$V_c = \frac{I_{ac} g}{\omega A \epsilon}. \tag{1.4}$$

Substituting (1.4) into (1.1), the electric field can now be written:

$$E = \frac{I_{ac} g}{\omega A \epsilon g} = \frac{I_{ac}}{\omega A \epsilon} = \frac{I_{ac}}{2\pi f A \epsilon}. \tag{1.5}$$

Area A and permittivity ϵ are fixed by the capacitive coupler design. The limitation on E then implies a limitation on I_{ac}/f. which can be given units of Amps/MHz. This says that a given capacitive coupler design's fundamental limitation is the AC current that it can pass, at a given frequency f (which is generally limited by the power electronics). This is analogous to Volts/Hz limitations in magnetic coupled systems.

The fact that I_{ac} is a fundamental bottleneck of any CPT system has implications on the design of the surrounding power electronics and matching components which are necessary to maximize power transfer and efficiency.

Power at each stage in the circuit can be defined by the following three equations.

$$P_{in} = V_{in} I_{in} = I_{in}^2 Z_{in}. \tag{1.6}$$

$$P_{ac} = V_{ac} I_{ac} \cos(\theta_{ac}) = I_{out}^2 Z_{out} \cos(\theta_{ac}). \quad (1.7)$$

$$P_{out} = V_{out} I_{out} = I_{out}^2 Z_{out}. \quad (1.8)$$

In the case of WFSM field excitation, Z_{out} is relatively low, because winding wire can only be made so small before the mechanical integrity of the rotating winding would be compromised. Because of this, I_{out} must be high in order to achieve high P_{out}. For simplicity of explanation, the approximation can be made that power factor angle in the AC portion of the circuit θ_{ac} is zero, and that efficiencies in the system are 100%, i.e.

$$\cos(\theta_{ac}) = 1 \qquad \text{and} \qquad P_{out} = P_{ac} = P_{in}. \quad (1.9)$$

With the knowledge that I_{ac} must be constrained to prevent electric breakdown (E < 3.0 kV/mm) , we can see that the characteristic impedance in the AC power coupling section, Z_{ac} must be high, because

$$Z_{ac} \approx \frac{V_{ac}}{I_{ac}} \quad \text{so} \quad \downarrow I_{ac} \rightarrow \uparrow Z_{ac}. \quad (1.10)$$

We have shown that Z_{out}, in the case of WFSM field excitation applications, is low, while Z_{ac} in the coupling circuit is high. This necessitates some form of impedance matching circuitry to be present within the secondary side electronics. In the WFSM case, the secondary electronics are located on the rotor of the machine. The use of passive matching (i.e. AC matching transformer or other passive impedance matching elements) inserted between the secondary side capacitive

coupler plates and the rectifier, as in the stationary CPT experimentation of [33]–[35], would likely be prohibitively bulky and difficult to build for high speed rotation.

Alternatively, a better option is to rectify the high impedance AC coming from the coupling capacitors to DC, and use a compact solid state "buck" converter to adapt this high voltage, low current rectifier output to low voltage, high current as required by the low impedance load, Z_{out}, as suggested in [36].

1.2.2.2 Limited Coupling Capacitance

Especially evident in the area of rotational or otherwise moving capacitive coupling interfaces, sizable gaps must exist between primary and secondary surfaces of the coupler structure in order to avoid friction and wear. The gap usually contains air, which has a low permittivity very close to that of free space, $\epsilon_0 = 8.85 \times 10^{-12}\,\text{Farads/meter}$, or $\epsilon_r = 1$ [37]. Air's low dielectric constant, in combination with the large gap between electrodes results in a rather limited capacitance between the primary and secondary side of the capacitive coupling system.

Dielectric coatings with much greater dielectric constants could be applied to the surfaces of the electrodes; however, as shown in [38] dielectric coatings do not provide much benefit in systems where the coating thickness is small compared to a large air gap. As will be seen later, this limited coupling capacitance, along with the limitations in electric field intensity to avoid arc breakdown, can be compensated for in the power electronics.

1.2.2.3 Parasitic/Leakage Capacitance

In an ideal capacitive coupling system, the only capacitance that exists would be the desired capacitance between corresponding electrodes of the primary and secondary coupler surfaces, as shown in Figure 1-6. A nearly-ideal CPT system was demonstrated experimentally in [39] using linear bearings riding on conductive rails, where leakage capacitances were orders of magnitude smaller than the coupling capacitances.

In more compact systems, such as the WFSM excitation system presented here, the various electrodes of the coupling structures must be placed near each other, as well as being placed near other external conductive surfaces (i.e. housings, enclosures, shafts, mounting hardware). Because any two conductors, when separated by a dielectric material, form a capacitor, there are unavoidably a multitude of leakage capacitances which develop as shown in Figure 1-7.

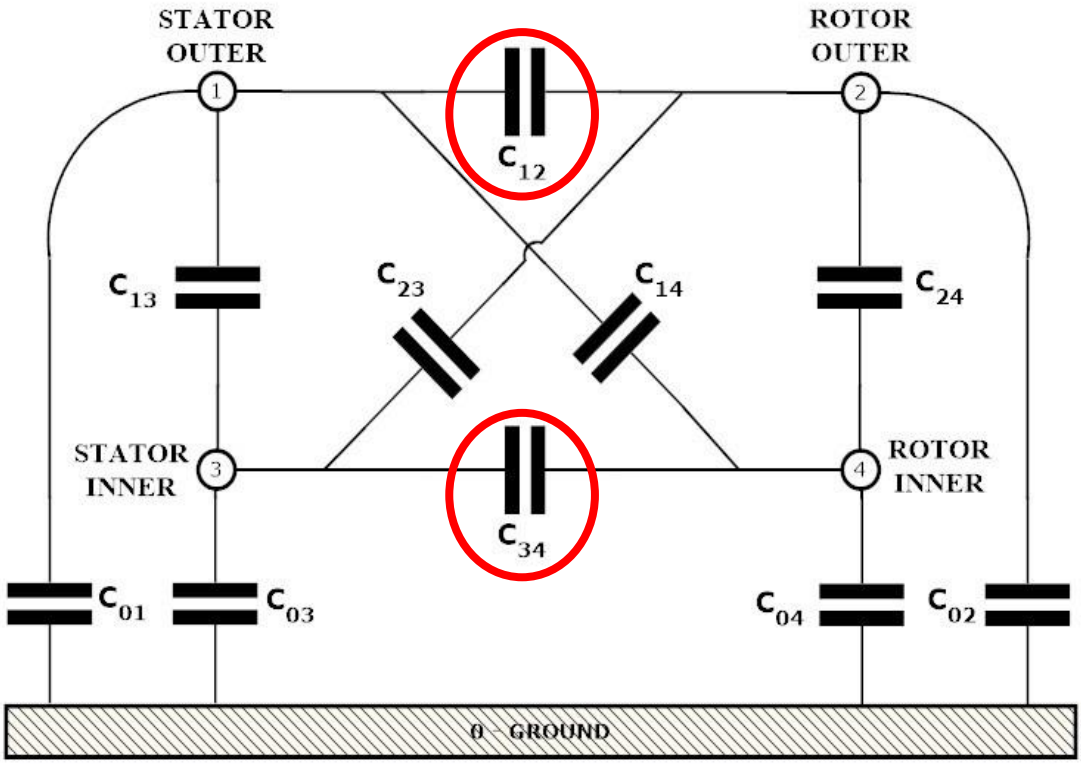

Figure 1-7: Undesired leakage capacitances in a capacitive coupling system for a wound field synchronous machine rotor winding. Desired coupling capacitances (the ones shown in Figure 1-6) are circled in red, while all other capacitances shown are considered undesirable parasitics of the system.

These leakage capacitances do not add to the power throughput capability of the coupler. Instead, they add paths for leakage current to circulate, which reduces efficiency by generating extra conduction loss and dielectric loss. As will be discussed further in the design section, these leakage capacitances can be minimized using good design techniques, to peak system performance.

1.2.3 Categories of Capacitive Power Transfer

Capacitive power transfer can be segregated into two primary categories: large gap, and small gap – depending on the physical construction of the coupling capacitor structure.

Large gap (here considered to be anything >1mm gap) is typically intended for applications like wireless charging of electric vehicles from the road [33]–[35], [40]–[51], energizing of low power electronic devices inaccessible by wires [52], [53], etc. Large gap CPT is inherently has very low coupling capacitance, requiring that very high coupler voltages and frequencies must be applied to obtain a useable power throughput.

Small gap (here considered to be anything <1mm gap) has the advantage of higher coupling capacitance, avoiding some of the negative implementation characteristics of large gap CPT. Although the distance across which power is transferred is not as large, the presence of any gap between primary and secondary electrodes allows for relative motion between the two surfaces, without any friction or wear. An exhaustive survey of small-gap CPT methods was carried out in [31]. Small gap CPT work for rotating loads specifically was carried out in [32], [54], [55] among others. This technology opens up a wide range of possibilities for power transfer between stationary sources and moving loads (whether they are moving translationally or rotationally.)

Examples of both large gap and small gap capacitive power transfer which have been demonstrated previously will be described in the following sections.

1.2.4 Review of Large Gap Capacitive Power Transfer

Because the focus of this work is in small gap capacitive power transfer, less time will be spent discussing large gap CPT. However, a few examples will be given in order to show the capabilities of large gap CPT systems, as well as their drawbacks.

In 2017, research was done in the area of wireless charging of vehicles from electrodes recessed in the roadway, using capacitive power transfer [41]. The gap in this case was the clearance between electrodes on the bottom surface of the automobile and the roadway. The general layout of the intended application is shown in Figure 1-8.

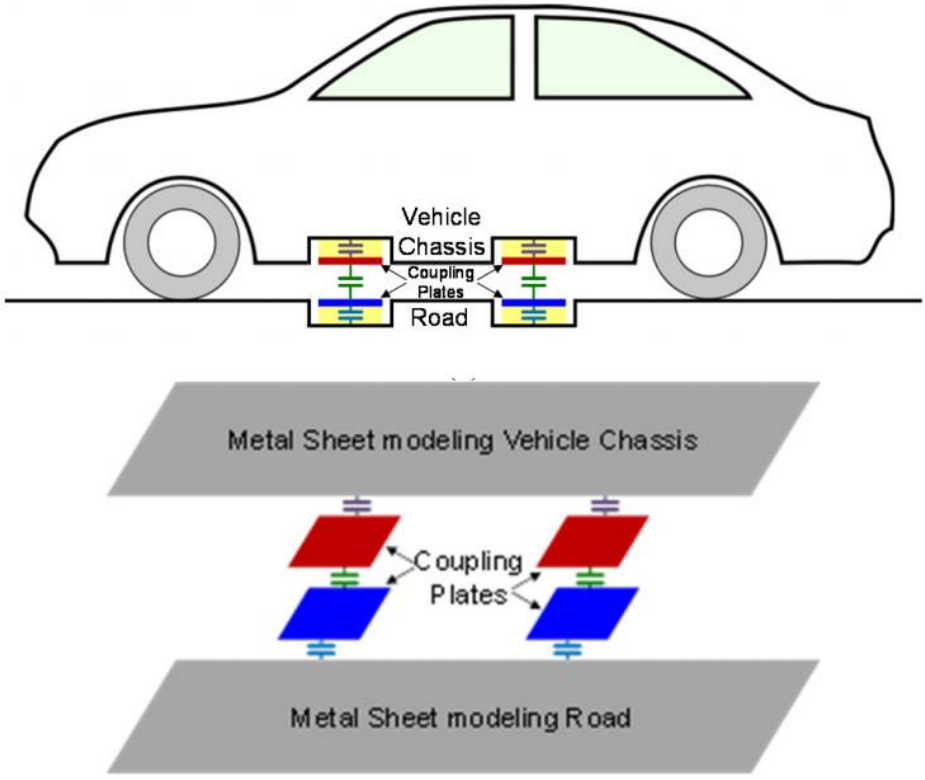

Figure 1-8: Capacitive wireless vehicle charging scheme laid out by Regensburger et al. [41].

In order to reduce the effects of fringing fields, as a result of the large distance between coupling electrodes (compared to their area), the road and the chassis of the vehicle are used as “ground planes” in close proximity to the primary and secondary side coupling plates. The setup used to simulate the roadway and vehicle ground planes in addition to the actual capacitive coupler plates, is shown in Figure 1-9.

Using this setup, the group was able to transfer 557 watts at 82% efficiency from the simulated roadway to the simulated vehicle underside. Unfortunately, approximately 10kV was required on the coupler plates, causing a serious safety concern if this was to be implemented in the presence of humans and animals in a real application.

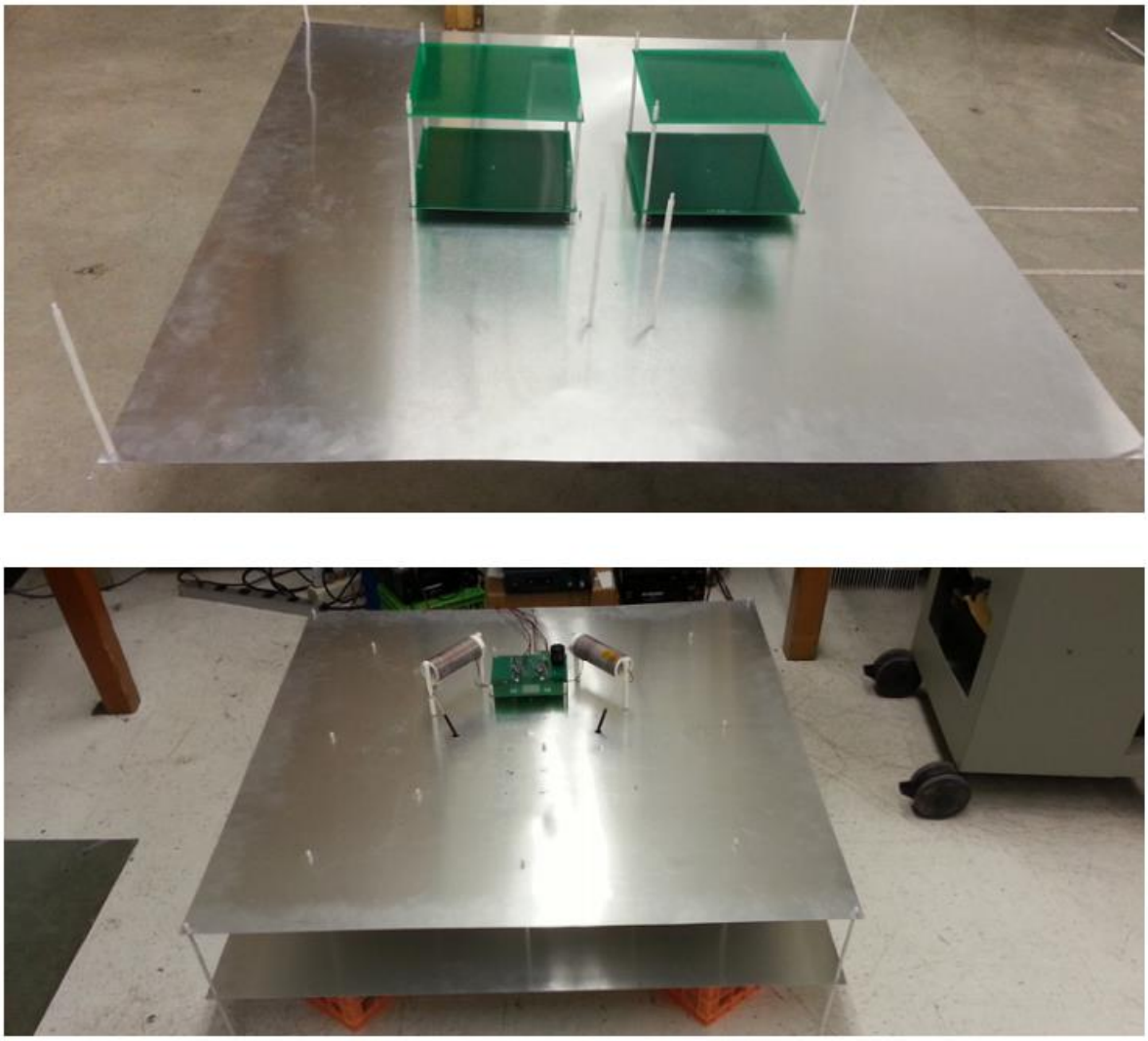

Figure 1-9: Simulated roadway to vehicle wireless charging scheme, using aluminum plates to simulate the ground plane formed by the roadway and the vehicle's chassis [41].

Large gap wireless power transfer has also included some hybrid inductive and capacitive power transfer topologies. Approximately 100 watts power has been transferred over an 18mm air gap with 73.6% efficiency using one such approach [56]. The coupler was comprised of a bent metal structure as seen in Figure 1-10. The relative orientation between segments of the coupling structure provided a hybrid electrostatic and electromagnetic coupling between the primary and secondary side. Because of the serpentine path of the electrode structures however, the overall volume of the coupler was quite large, in addition to the large volume occupied by the resonant inductors and passive matching components.

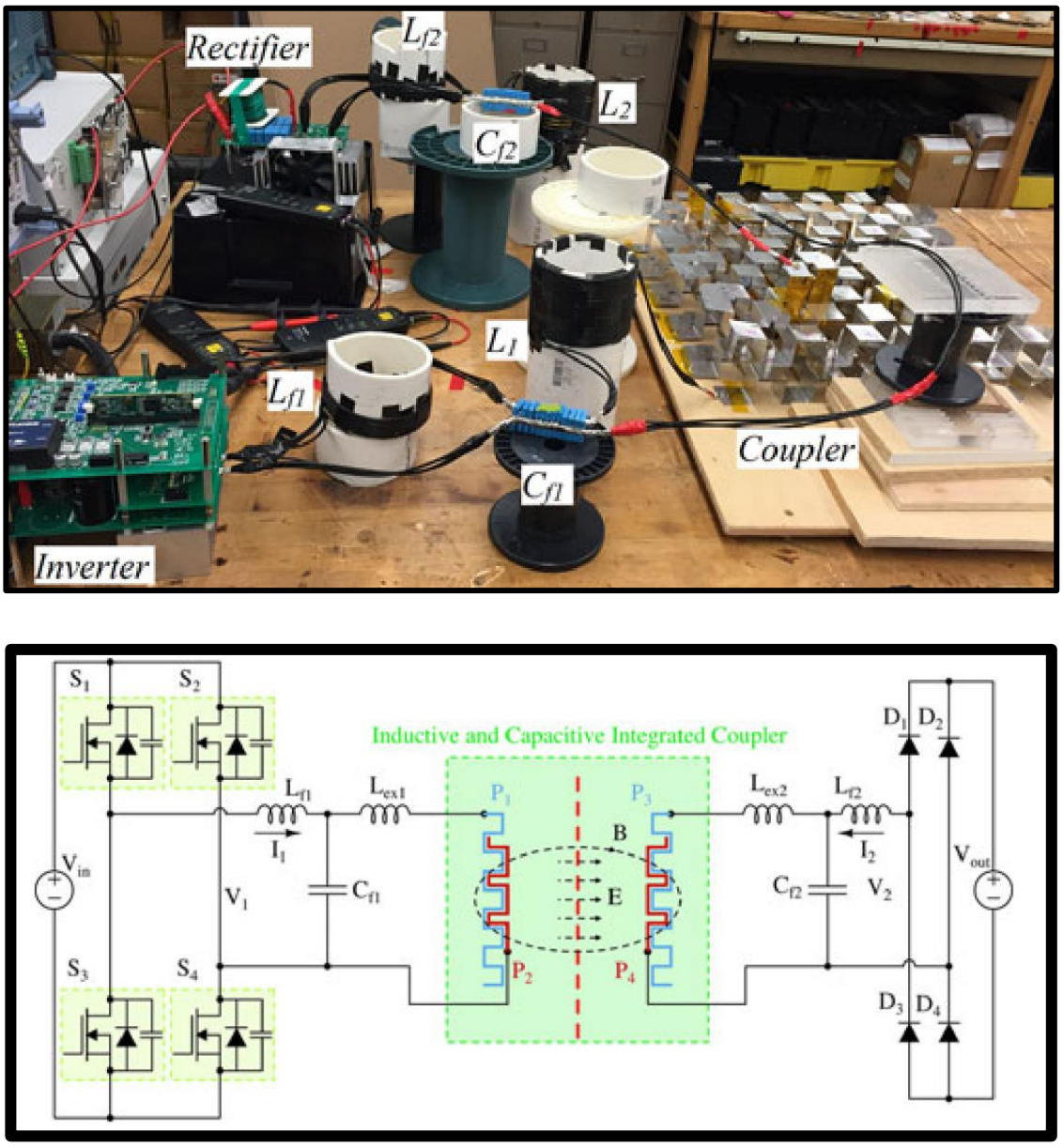

Figure 1-10: Integrated LC Coupler. Photo of layout (top) and circuit diagram (bottom) [56].

The same researchers also demonstrated a much higher power large gap system, targeted at electric vehicle charging, which transferred 2.2 kW of power across a 150 mm air gap with 86% efficiency [42]. The system similarly requires multi-kV voltages on the coupling plates, due to the small capacitance resulting from the large spacing between them. The matching between low voltage inverter and high voltage at coupler, as well as matching between high voltage coupler and low voltage load, is accomplished by LCL matching networks placed on the primary and secondary sides of the coupler. As seen in Figure 1-11, these matching networks (air core inductors and large high voltage capacitors) in addition to the large volume of the coupler itself, lead to a bulky overall system requiring a great deal of space on the vehicle it is intended to charge. Safety concerns arise from the leakage fields surrounding the high voltage coupling plates.

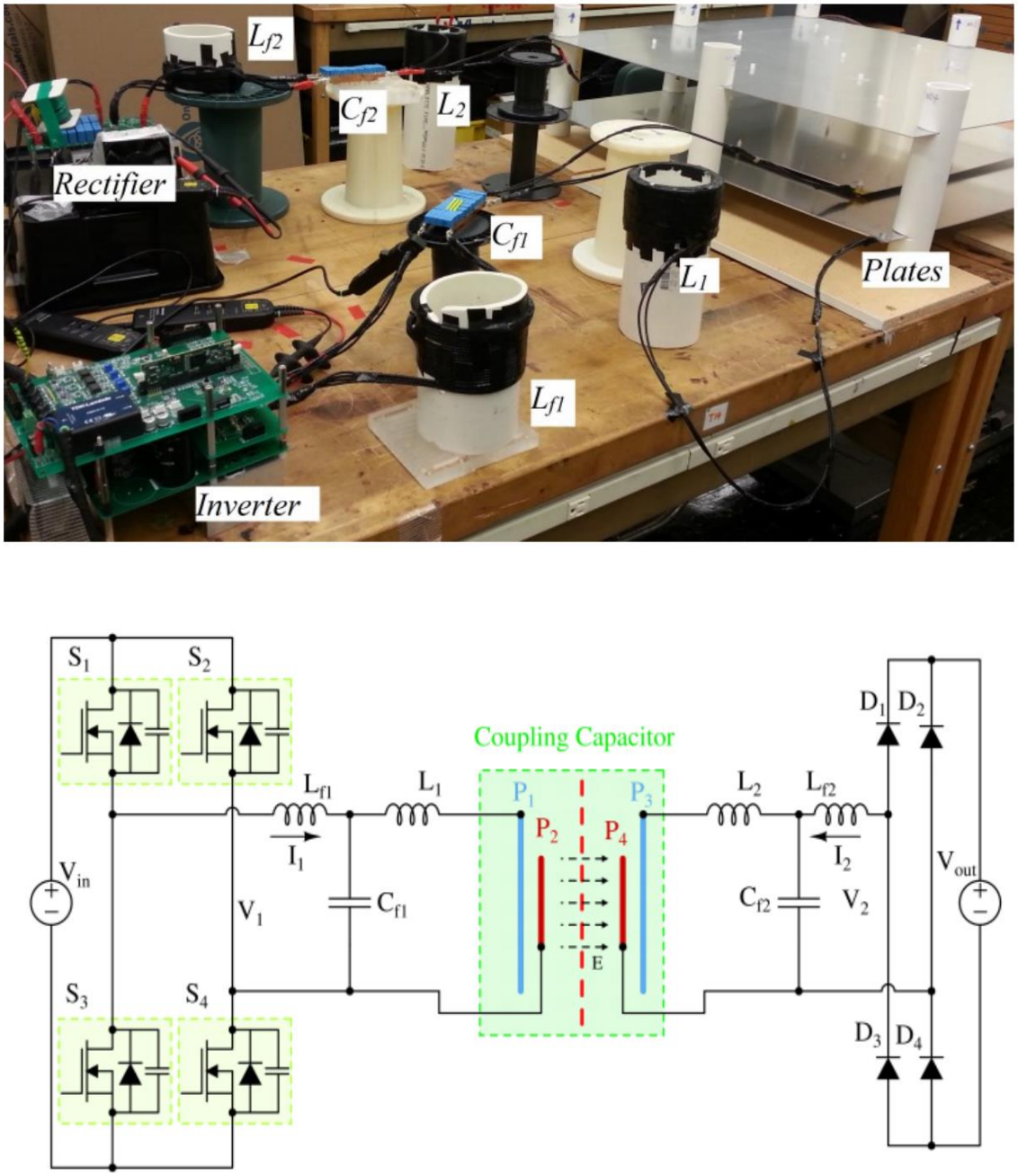

Figure 1-11: Four plate coupler structure, with matching components shown (top). Corresponding circuit diagram (bottom), for 2.2kW 150 mm gap coupling system [42].

Though not entirely a capacitive power coupling system, a large gap hybrid LC coupling system was demonstrated which was able to transmit just under 3kW with 95% efficiency over a 150mm gap [57] as seen in Figure 1-12. Unlike the previously described hybrid LC example, which shared the same structure for both the inductive and capacitive portion of the coupling effect, this example uses entirely separate coupling coils and capacitor plates, leading to a fairly large system. Peak coupling plate voltages are on the order of 7kV. Although this does not lead to an arc breakdown hazard, it does generate hazardous AC electric field intensities.

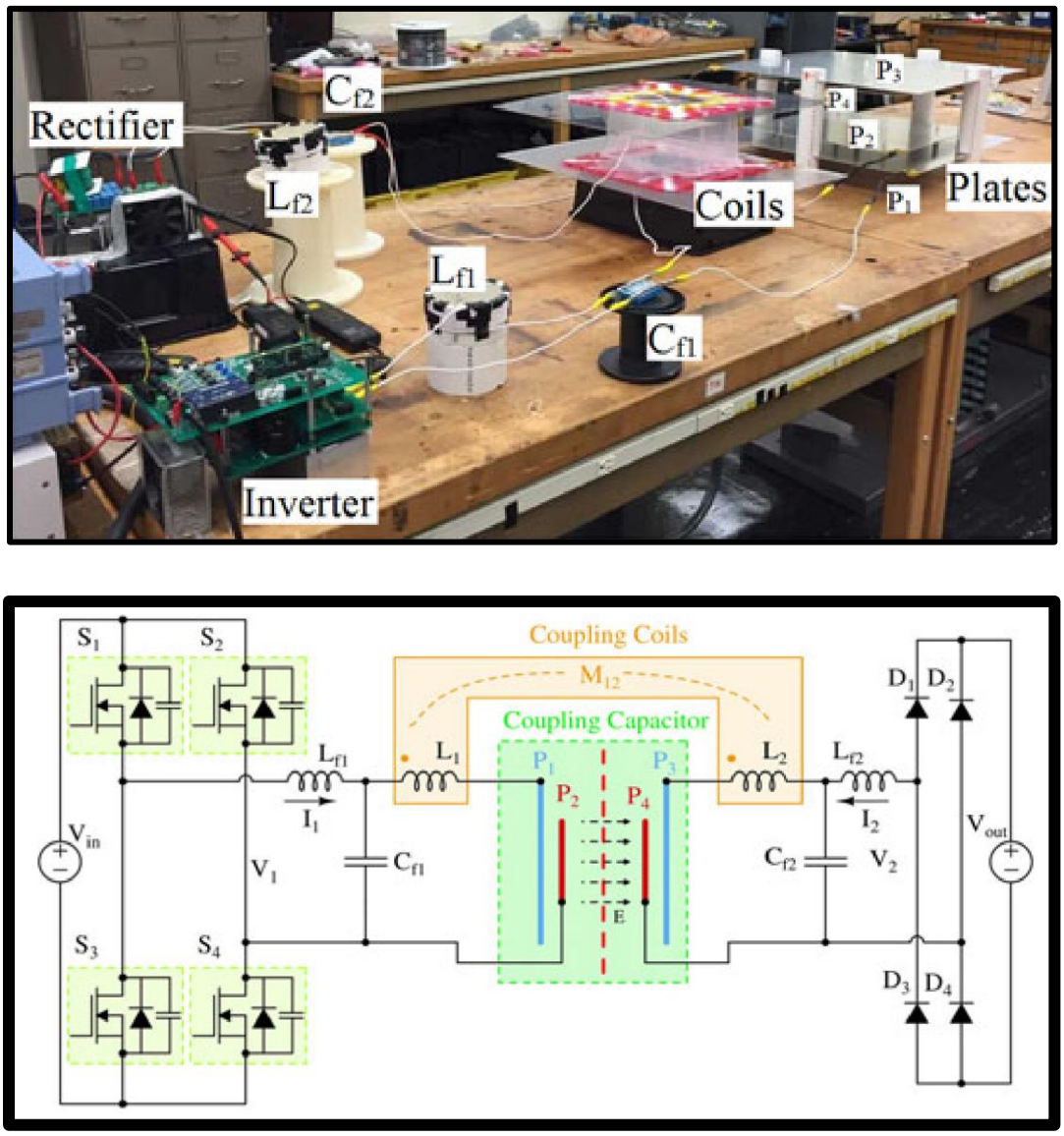

Figure 1-12: High power wireless vehicle charging system employing separate inductive and capacitive coupling elements. System photo (top) and circuit diagram (bottom) [57].

In summary, although very high power transfer levels have been demonstrated with large-gap capacitive power transfer, at high efficiency, its potential applications will be limited based on safety concerns associated with 10kV+ voltages on system components. This is not only a concern for safety of humans and animals in the vicinity, but also material degradation due to corona discharge in surrounding air.

1.2.5 Review of Small Gap Capacitive Power Transfer

By reducing the gap in a CPT system, the designer can take better advantage of the available coupling area, while maximizing power transfer capability for a given operating frequency and peak coupler voltage. Because the system is still non-contact, there is no friction or wear, so relative motion between the primary and secondary side are still possible, much like the large gap counterpart. However, the safety concerns which affect large gap CPT due to the high voltages and intense AC electric fields they require are eliminated, and a more volumetrically compact system can be achieved. Some example small gap CPT systems will be shown here.

In the area of electric vehicle charging, a conformal bumper was designed in [58] which transferred >1kW at 90% efficiency to charge the battery park of a small EV. Using a foam rubber substrate on the wall-mounted charging surface, the CPT coupler gap could be minimized between primary and secondary coupling surfaces. By minimizing the gap, capacitance was quite sizeable allowing kW power transfer with only approximately 500V on the coupling electrodes at about 530kHz. The vehicle charging bumper and conformal wall charger electrode structure can be seen in Figure 1-13.

Figure 1-13: Conformal bumper electric vehicle CPT structure showing receiving electrodes on bumper (top) and wall mounted conformal electrode structure (bottom) [58].

Although this system had high power and efficiency and relatively low voltage and frequency requirement, the close contact of the primary and secondary electrode structures eliminated the possibility for relative motion between the two surfaces. This was not an issue for a stationary charging application, but it would not allow this type of coupler to be used for WFSM excitation (rotary CPT coupling) due to the friction that would develop between electrodes.

Using a similarly designed coupling structure, but on a much smaller scale, a drone charging system was developed in [59] which transferred 12 watts at about 50% efficiency. This coupling system, based around the 6.78MHz Industrial Scientific and Medical (ISM) frequency, can be seen in Figure 1-14. Similar to the conformal bumper approach, the electrodes of the primary and secondary coupler structures had to be in near contact (separated only by insulating films), thus this type of structure would similarly not be suitable for a rotating application such as a WFSM field winding.

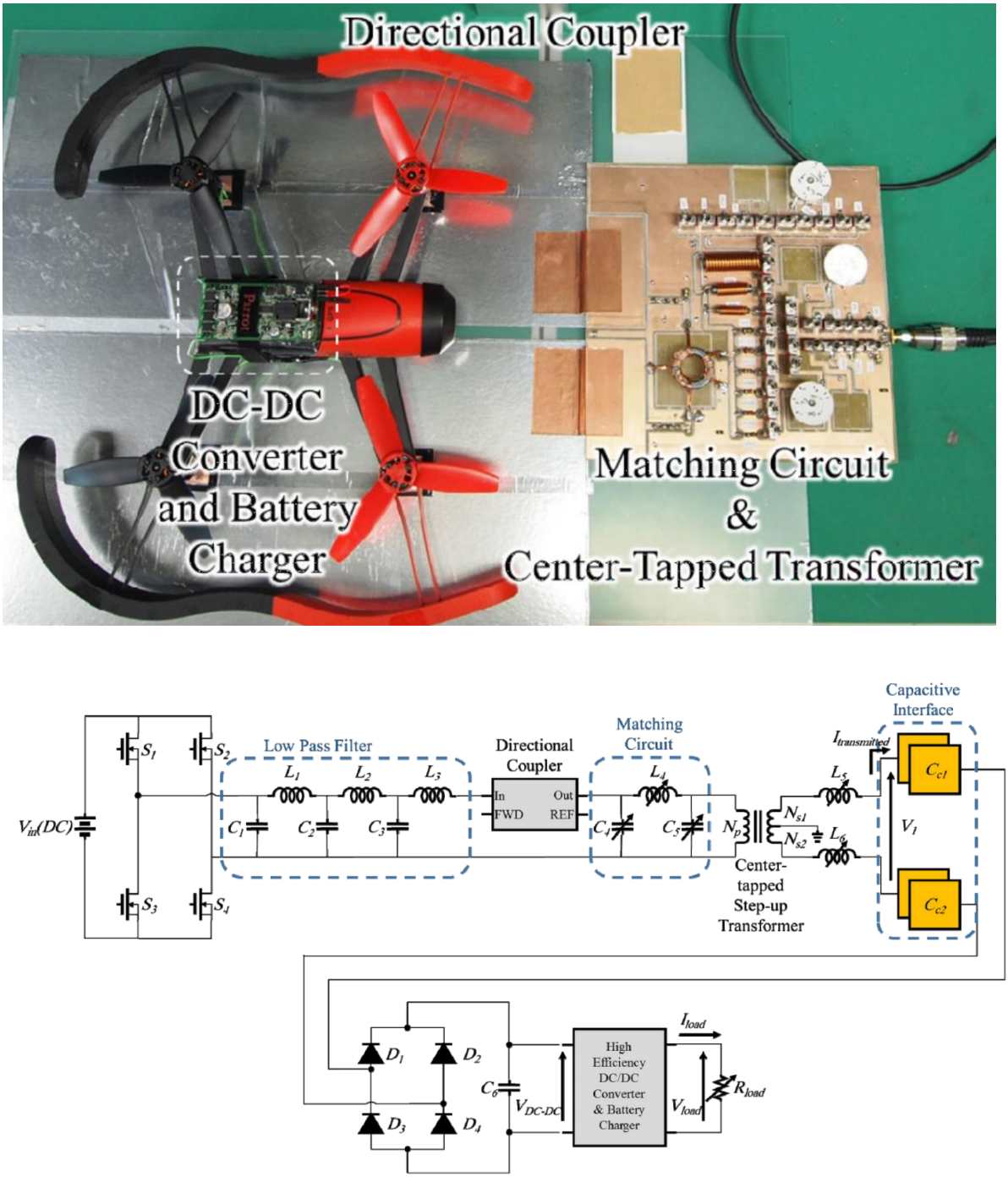

Figure 1-14: Capacitive drone charging system using the 6.78 MHz ISM frequency. Photograph of setup (top) and circuit diagram (bottom) [59].

Because the focus of this work is on rotational capacitive couplings, a number of examples of past work in this area will be introduced; including some capacitive couplers specifically designed for the excitation of wound field synchronous machine rotor windings.

As early as 2009, a research group proposed two different methods for capacitive power transfer across a rotating gap in [55]. The first method, being a pair of disks, with concentric planar electrodes, and the second being a pair of concentric cylindrical electrode sets, as shown in Figure 1-15.

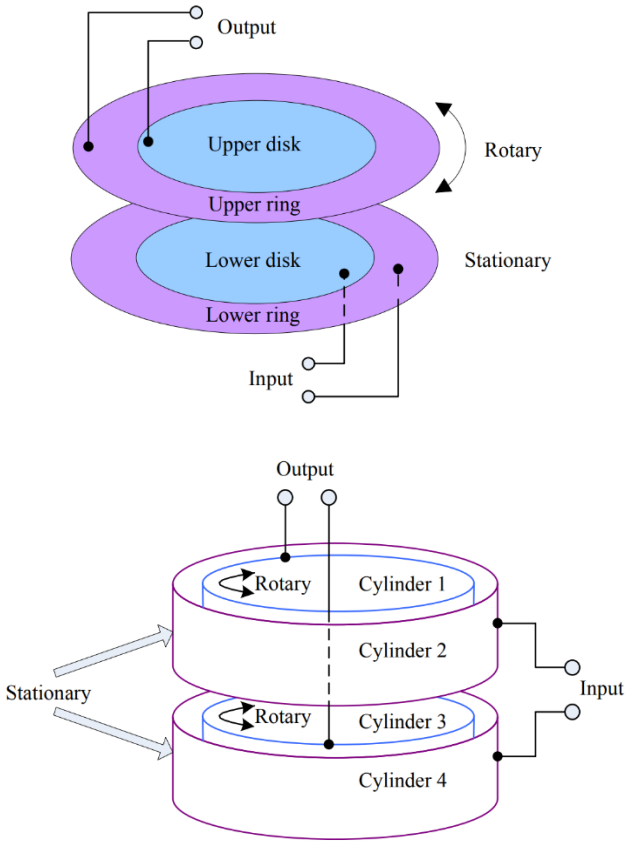

Figure 1-15: Disk (left) and cylinder (right) configurations for rotational capacitive power coupling shown in [55].

Simulations and experimental work were carried out in [55] for the cylindrical version of the coupler. The experimental system demonstrated 12.3W output power with an overall system efficiency of 42.7%. Although the power level and efficiency value seem low in this early contribution, the proposed mechanical coupling structures paved the way for several later CPT demonstrations. The disk type coupler described in [55] is the fundamental arrangement that is the topic of this paper.

Initial work in the area of capacitive wound field machine excitation as an alternative to slip rings or magnetic transformers included a discrete plate type air capacitor structure in [3]. Similar in construction to a radio tuning air variable capacitor, a structure of alternate rotating and stationary aluminum plates was constructed, which formed two separate capacitors, whose capacitance value remained constant throughout rotation. A cross section diagram and photo of the system can be seen in Figure 1-16.

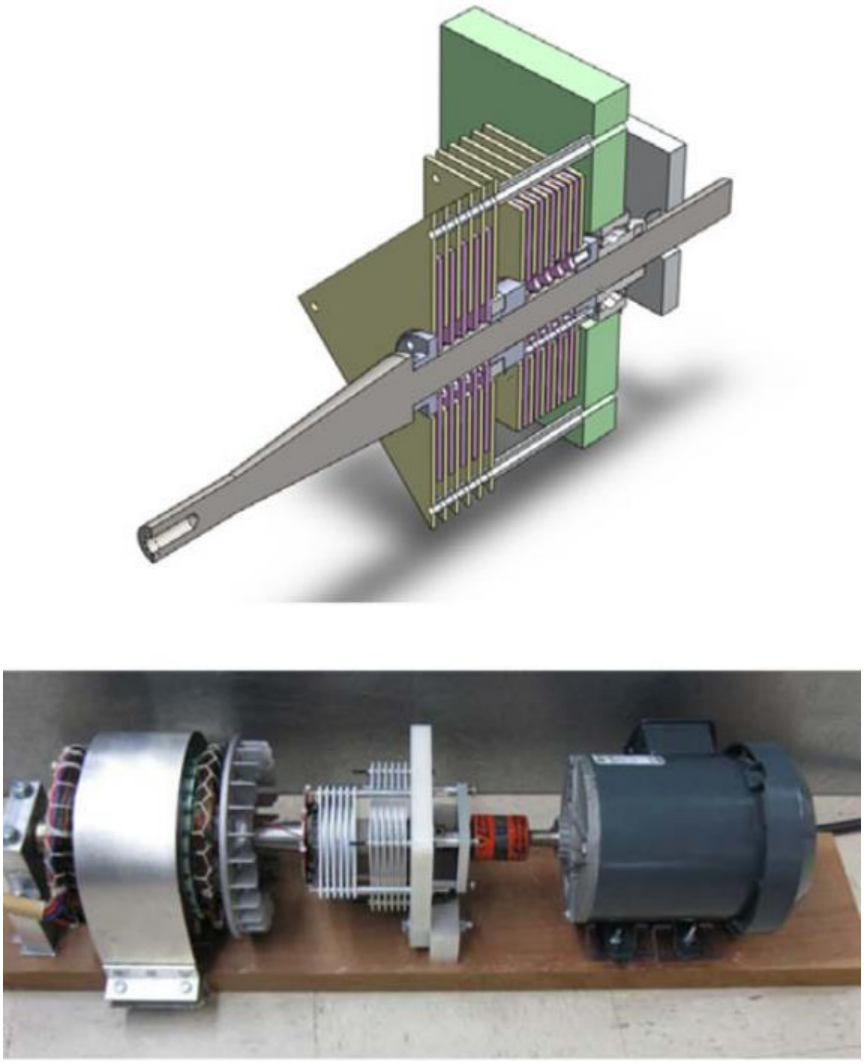

Figure 1-16: Discrete plate air gap capacitive coupler structure (top) and installation on the rotor of a wound field generator (bottom) [3].

The discrete plate coupler was able to transfer 6.5 watts to excite the wound field generator rotor, with 94% efficiency at 626 kHz. This initial attempt at capacitively powering a rotor field winding proved that CPT was a viable replacement for slip rings; though the large volume and complex mechanical structure left room for improvement. Also, this early work was completed before the advent of widely available wide bandgap semiconductors, thus limiting frequency of operation.

Because current throughput capability is limited by coupler capacitance, it is desirable to maximize capacitance by minimizing the gap between coupling electrodes. A coupler structure was produced in [2] which used hydrodynamically levitated journal bearings (much like the crank shaft bearings in an automotive engine) to transfer 340 watts at 85% efficiency. Photographs of the coupler structure can be seen in Figure 1-17.

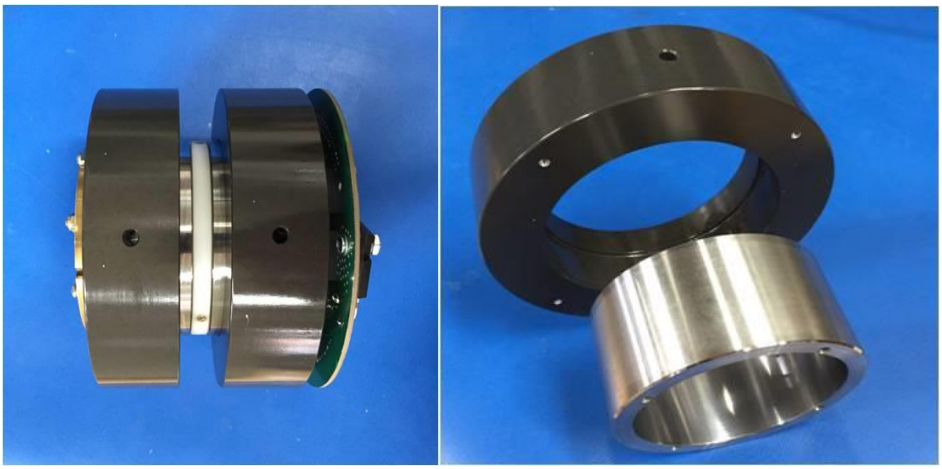

Figure 1-17: Hydrodynamically levitated journal bearing capacitive power coupler. Assembled with rotating rectifier board (left) and individual bearing and shafting components (right) [2].

Using oil as a dielectric, which has a higher permittivity than air, as well as maintaining electrode gaps on the order of a few thousands of an inch, integer nanofarad coupling capacitance was achieved. This high capacitance facilitated high power transfer, while keeping electrode voltages around 500 volts. Because the bearings were hydrodynamically levitated, the bearing could be rotated up to 1800 rpm without significant heating or wear. Unfortunately, due to viscous drag loss, this type of bearing is not suitable for higher speeds (i.e. several thousand rpm and up).

In an effort to eliminate friction contact for small gap capacitive power transfer high speed rotational or translational motion systems, while maintaining higher coupling capacitance per unit electrode area than can be achieved using a discrete plate coupler structure, research was done in [60] and [61] to use aerodynamic levitation of capacitor coupling electrodes in rotating systems. The research investigated aerodynamic levitation between coupling electrodes in both axial field and radial field arrangements. Photos of the coupler rotor disk, as well as an edge view of the assembled coupler disk stack are shown in Figure 1-18. This coupler successfully delivered 100w power to its resistive load during experimental testing.

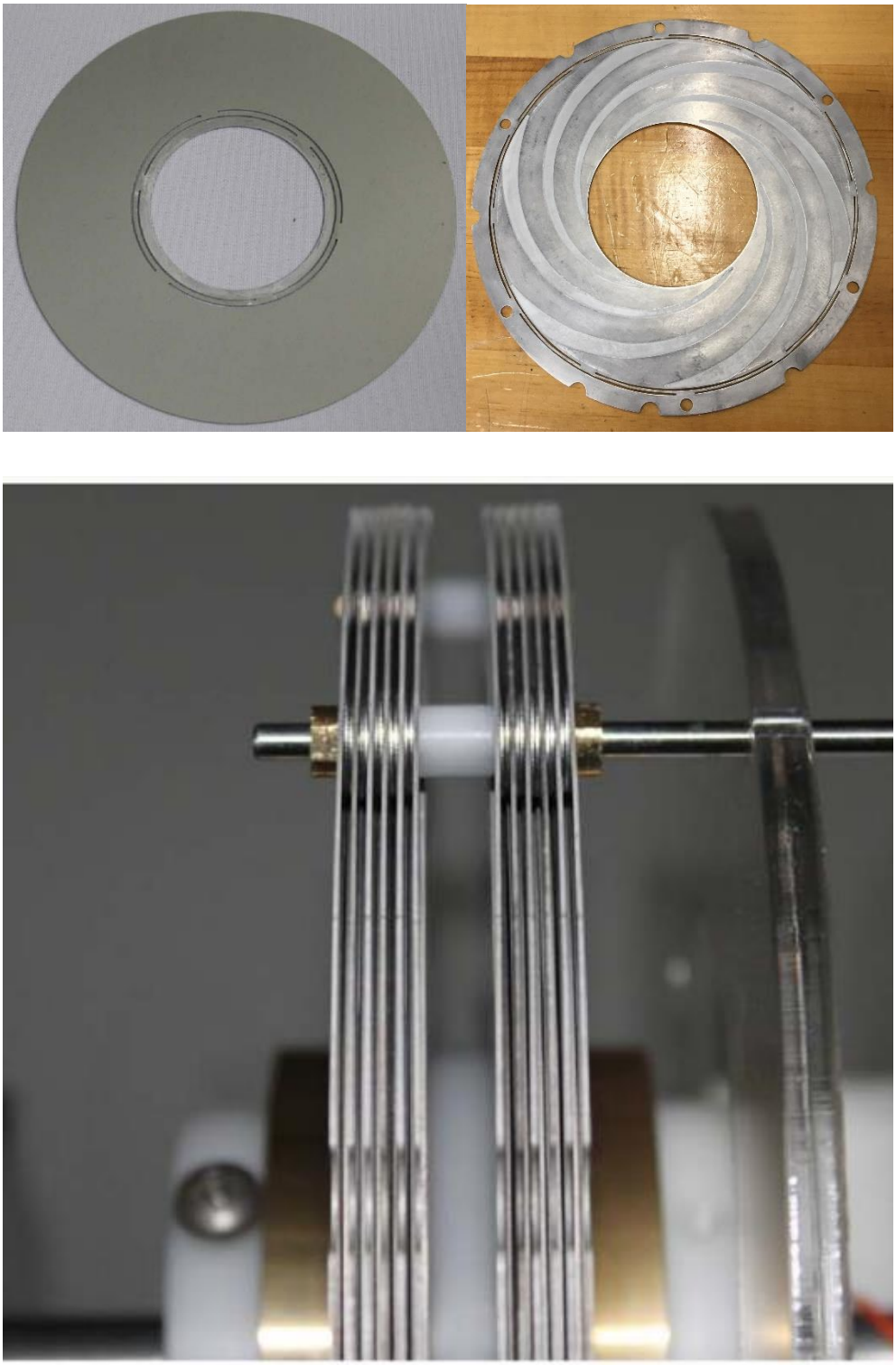

Figure 1-18: Rotor and stator disks and coupler stack for aerodynamic capacitive power coupler from [61].

Further advancement was made in the area of aerodynamically levitated “hydroflex” disk bearings in [62] and [63]. The overall size of this aerodynamic coupler was much smaller than the earlier example produced in [61]. This capacitive coupler was able to transfer approximately 1kW power to the rotor of a wound field synchronous generator with a base speed of 4,000 rpm. A photo of the coupler is shown in Figure 1-19.

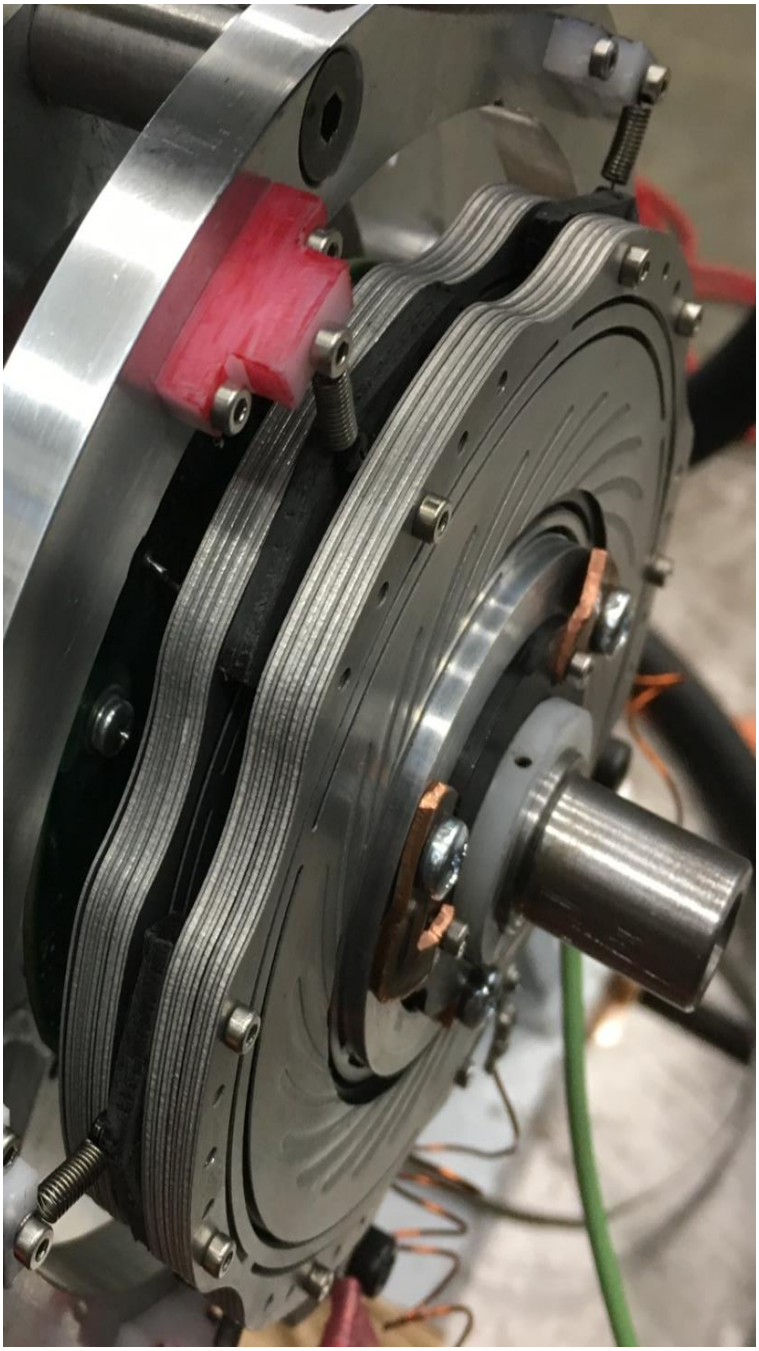

Figure 1-19: Aerodynamically levitated “hydroflex” axial thrust air bearing used as capacitor electrode structure in a 1kW CPT system for WFSM field excitation [62], [63].

An exploded view diagram of the assembly of the capacitor coupler plate structure is shown in Figure 1-20. This illustrates the cascading of multiple closely spaced plates, separated by an air cushion during rotation, that was used in order to fit a larger coupling capacitance into a small axial length on the machine shaft.

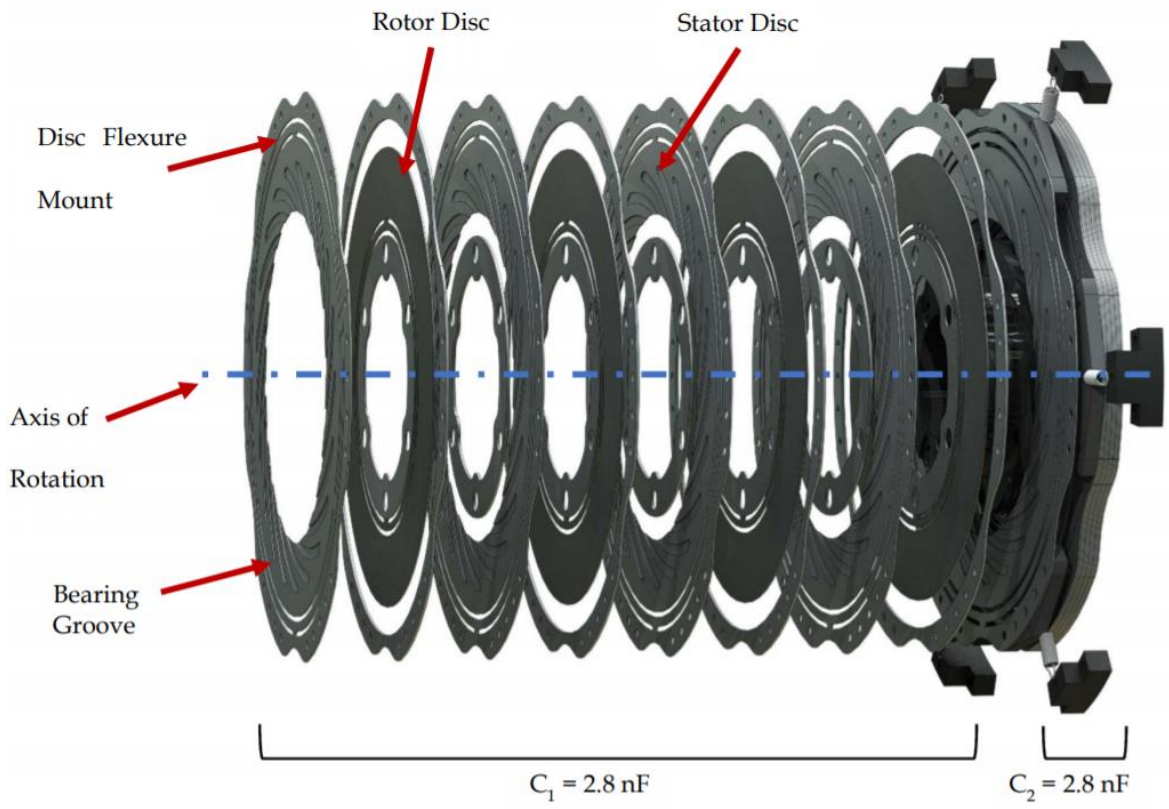

Figure 1-20: Exploded view of aerodynamically levitated cascaded disk CPC from [63].

Though this aerodynamic bearing CPC performed well mechanically and electrically, its electrode plate structure is intricate and difficult to manufacture and align. Thus the cost of installing such a coupler in high volume applications would be prohibitive.

In aforementioned examples of small gap capacitive couplers, heavier electrodes were required in order to provide mechanical strength, in order to ensure the dielectric gap is maintained. Electrically, at the high frequencies involved, the electrode only needs to be as thick as the skin depth at which current will flow through the particular electrode material at the operating frequency used. If high enough frequencies are used, this skin depth in materials like copper and aluminum is on the order of thousandths of an inch. Materials like the thin flexible aluminum disks (of the previous example) and the copper plating of a printed circuit board are thick enough to use as coupler electrodes.

The idea of reducing capacitive power coupler transmitter-to-receiver alignment sensitivity by pixelating the receiver structure was discussed in [64]. In [65], a position independent capacitive cell phone charger prototype was constructed and successfully transferred approximately 1w 5V USB power to a cell phone. The coupler secondary side structure was nothing more than a printed circuit board containing capacitive electrodes, rectifier diodes, and a voltage regulator for USB power output. A photo of the experimental setup can be seen in Figure 1-21, as well as a schematic diagram of the pixelated receiver with hexagonal pixel electrodes and rectifying diodes.

The results of this research showed that the copper plating of a printed circuit board is sufficient in thickness to conduct the required high frequency electrode current in a capacitive power transfer system, because the skin depth in copper at the MHz frequencies used is similar to the copper plating thickness. The use of printed circuit boards as the sole coupling electrode structure in a much higher-power system will be the topic of this paper.

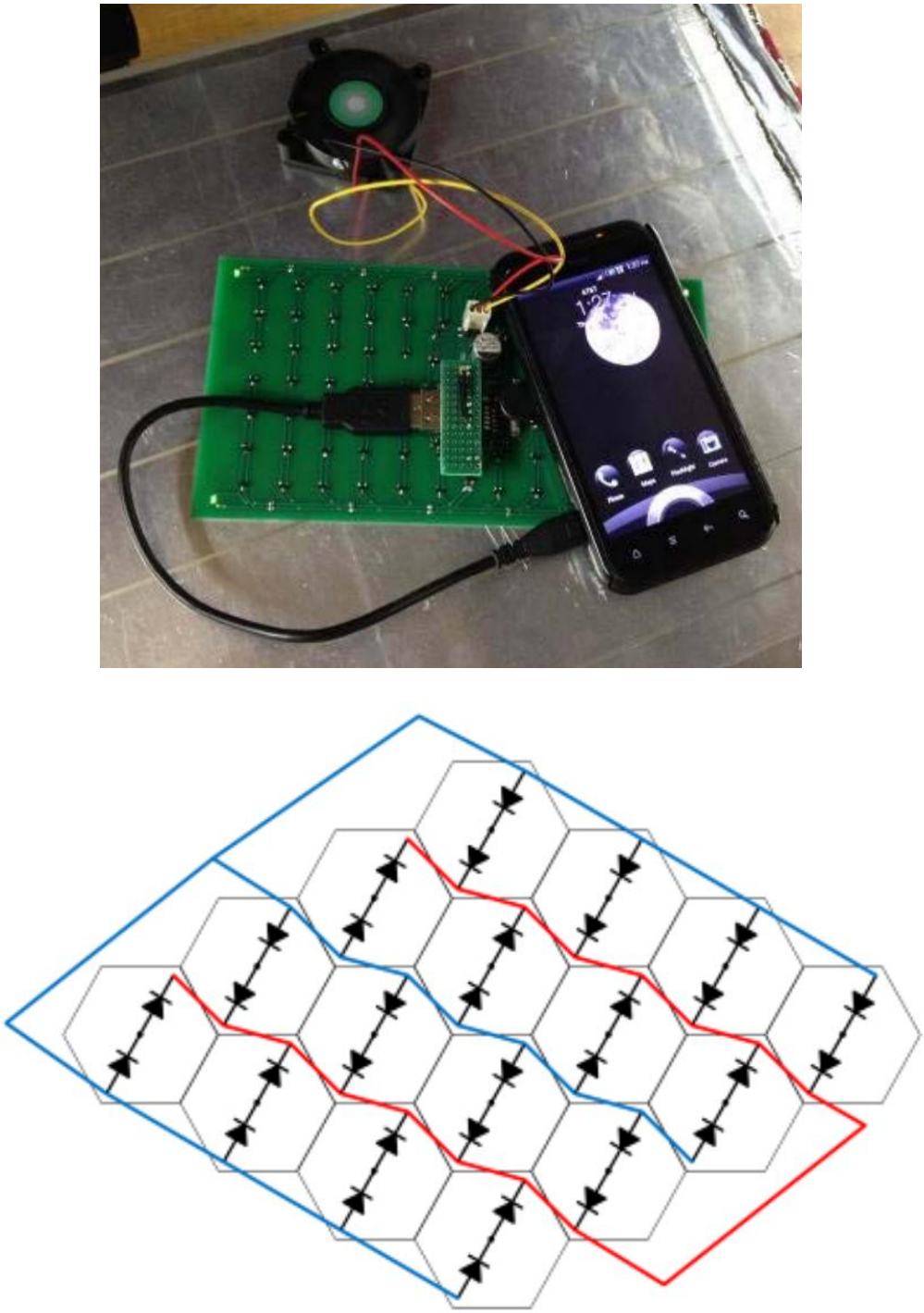

Figure 1-21: Capacitive cell phone charging system, using a printed circuit board as the coupler receiver structure. Photo of prototype (top) and schematic representation of receiver (bottom) [65].

1.2.6 Conclusion – State of the Art Review

This work deals with rotational capacitive power transfer for the purpose of exciting wound field synchronous machine rotor windings. Using lessons learned from the past CPT work described here, a new type of rotating capacitive power coupler will be described in the chapters to follow which allows rotational coupling with zero contact or viscous drag effects, while also being of a low cost easy to manufacture construction.

It is seen that in all forms of brushless excitation for wound field machines, a rectifier board must be included on the rotor in order to convert alternating current from the exciter to direct current for the WFSM field winding. Because a circuit board must already be included on the rotor in order for successful brushless excitation, **the primary interest of this work was to show that the same PCB can also be used as the power coupling structure**, with no additional structures or extra components required on the rotor. Motivation for the use of such a dual-purposed PCB coupler is shown in the following section.

1.2.6.1 Motivation for use of PCB's for Rotational CPT

It has already been shown that capacitive coupling can fully replace slip rings and rotating magnetic field couplers for wound field synchronous machine excitation in [1], [2], [62], etc. The downfalls of the previous work in CPC excited WFSMs lay in their complexity, longevity, and a

number of other factors. The characteristics that are desired for rotational capacitive couplers can be summarized into the following seven categories:

- Large coupling capacitance
- Low leakage
- Manufacturability
- Low physical volume
- High speed capable
- Mechanical robustness
- Fully non-contact

A careful assessment of the previous work in the area of rotational capacitive coupling methods was performed, and a comparison of the different coupler topologies on the basis of these categories is shown in Table 1.

TABLE 1. ROTATIONAL CAPACITIVE POWER COUPLING BENEFIT COMPARISON

	Journal Bearing	Hydroflex Disk	Discrete Plate	Printed Circuit Board
Large Coupling Capacitance	✓	✓	✗	✗
Low Leakage	✓	✓	✓	✗
Manufacturability	✓	✗	✗	✓
Low Volume	✗	✓	✗	✓
High Speed Capability	✗	✓	✓	✓
Mechanical Robustness	✓	✗	✓	✓
Fully Non-Contact	✗	✗	✓	✓

As seen in the table, the printed circuit board coupler stands out as having the greatest number of benefits, with the discrete plate [3] and hydroflex/aerodynamic disk [61]–[63] coupler types as close seconds. The discrete plate and hydroflex disk couplers offer little opportunity for improvement without sacrificing electrical performance. For instance, the manufacturing simplicity and volume of a discrete plate coupler cannot be improved without reducing capacitance, and therefore electrical capability. Similarly, the hydroflex disk coupler cannot be made fully non-contact without similarly reducing capacitance (essentially making it into a discrete plate coupler), thus in order to maximize electrical performance it will always have the opportunity for friction, wear, and deterioration at low-speeds where full aerodynamic levitation is not possible and rotor and stator disks are in physical contact with one another.

On the contrary, the coupling capacitance and leakage characteristics of a printed circuit board capacitive coupler *can* be improved through substrate material changes, and improvements in the board layout and design. Thus, even though the PCB coupler already has more advantages, it has further room for design improvement, while staying low cost, compact, and efficient. It is for these reasons that the printed circuit board coupler was selected to be the topic of this research.

1.2.6.2 Summary

Although printed circuit board couplers have lower coupling capacitance than aerodynamic or hydrodynamic counterparts, modern wide band gap power electronics allow high enough operating frequencies to facilitate adequate power transfer levels with reduced coupling capacitance. Printed circuit board manufacturing is a well-established process in almost all industries which produce electrical products, thus the cost of adopting PCB capacitive coupling components should be minimal. Because printed circuit boards can be made quite thin while still being mechanically rigid due to their glass fiber reinforced structure as shown in [66], the overall coupler volume can be much smaller than the volume of an equally rated magnetic coupling device. Because the PCB coupler is non-contact (i.e. the rotating component never comes in contact with the stationary component, even during stand-still and low speed), there is no wear, and theoretically no limitations on lifetime. For the same reasons, PCB couplers would be suitable for very high rotational speeds, lacking friction and being constructed of high strength composites such as FR4. Although capacitive power coupling systems are fundamentally limited by current, it will be seen that with the proper power electronics on the rotating rectifier board, they can easily and efficiently be matched to lower impedance loads such as the field winding of a typical WFSM.

Chapter 2 Printed Circuit Board Capacitive Coupler and Resonant Inductor Design

2.1 Capacitive Coupler Printed Circuit Board Design

In the first section of this chapter, the design of the printed circuit boards for capacitive power coupling will be discussed. General capacitive power coupler design steps will be laid out first, followed by a discussion of additional design considerations which are more specific to wound field machine excitation, and other rotational CPC applications. Design of the resonant tank inductor will be discussed in section 2.2.

2.1.1 General CPC Design Steps

2.1.1.1 Define Constraints

As seen in Figure 1-6 in the previous chapter, the capacitor coupler, made up of a pair of capacitors, is placed between the primary and secondary side electronics in a similar fashion to the way a transformer would be placed in an inductive power transfer system. This comparison is illustrated in Figure 2-1. Unlike a magnetic transformer, the capacitive coupler has no provisions for a "turns ratio." The AC voltage leaving the capacitive coupler will be equal in magnitude to the AC voltage entering provided series inductors within in the primary or secondary electronics cancel the capacitive reactance. Also, without any turns ratio, and because the capacitive coupler is simply in series with the load, the AC current entering the secondary electronics is equal to the AC current leaving the primary electronics. Inductive systems are inherently a "T" circuit, thereby having a magnetizing branch, and in certain circumstances the magnetizing current is non-negligible.

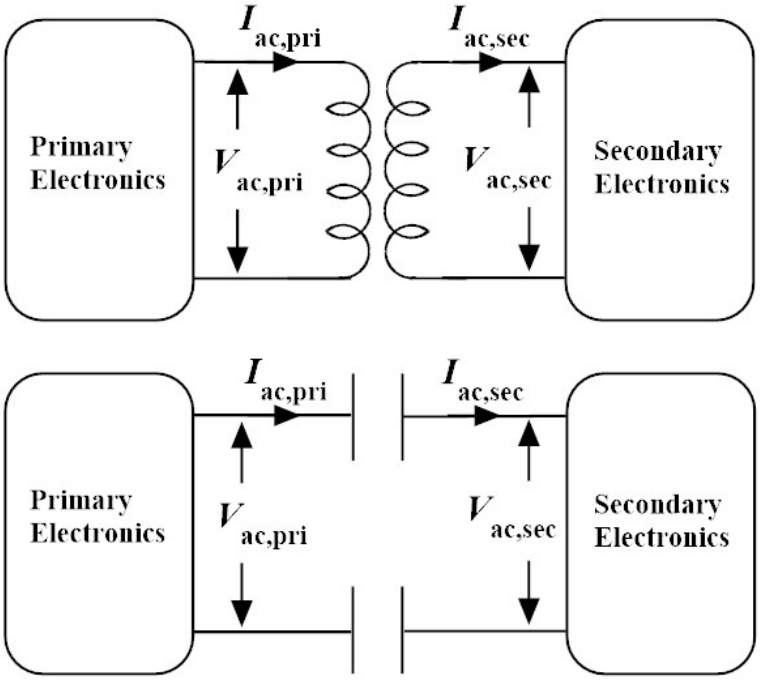

Figure 2-1: Comparison of capacitive power coupler (bottom) to inductive coupling transformer (top).

The AC current which is required to pass through the capacitive coupler is governed by the properties of the load, as well as whatever power conversion electronics are located on the secondary side of the capacitive coupler. In summary, the relationships between primary and secondary voltages and currents in the capacitive (bottom, with series inductors in primary or secondary electronics) coupling circuit of Figure 2-1 are:

$$|V_{ac,primary}| = |V_{ac,secondary}| \tag{2.1}$$

$$I_{ac,primary} = I_{ac,secondary}. \tag{2.2}$$

2.1.1.2 Electric Field Limitation

As discussed in the previous chapter, the primary limitation for power throughput in any capacitive power transfer system is the electric field that can be allowed in the capacitor gap, without risking corona discharge or arc breakdown. In the case of a printed circuit board capacitor electrode structure, as is the topic of this research, the standard solder mask coating may provide some additional breakdown protection. However, its only true purpose in printed circuit board manufacture is to block solder from adhering where it is not desired during the component assembly process. Because of this, it is not intended to be, nor can it be expected to function as a true dielectric conformal coating (the likes of Parylene [67], [68]) which is intended to be used for electrical insulation. Also, the presence of a thin dielectric film in a capacitor whose gap is primarily filled with air, as is the case here, will not prevent damaging corona discharge in the air if the breakdown electric field limitations of air are approached.

The dielectric breakdown field of air, alone, is used to calculate the safe limits for electric field in the capacitor gap. The breakdown field limit for dry air, around 3kV/mm, is used along with a safety factor to come up with a safe maximum field intensity. For example,

$$E_{maximum} < 50\%\ E_{breakdown} = 50\%\ 3\text{kV/mm} = 1.5\text{kV/mm}. \tag{2.3}$$

2.1.1.3 Achievable Air Gap

It is desirable to minimize air gap in order to maximize capacitance in the coupler structure. With typical low cost printed circuit board construction techniques, some amount of flatness distortion exists in the finished PCB, especially after various heating and cooling cycles during the process

of soldering components to the board. Based on observations on manufactured prototypes during the experimental work for this paper, it was decided that a safe gap distance to prevent the possibility of collision between the rotating and stationary coupler PCBs was

$$0.5 \leq g \leq 1.0 \text{ mm}. \tag{2.4}$$

In the final prototype described in this paper, the air gap on either side of the rotor coupler disk was approximately 0.8mm, within these acceptable limits. With additional effort, the boards could likely be made flat enough to support an even smaller gap through careful annealing as discussed in [63], but this would add some cost and complexity to the manufacturing process.

With the knowledge of a safe maximum electric field and capacitor gap, capacitor peak voltage can then be calculated.

$$V_{\text{c,maximum}} = E_{\text{maximum}} \cdot g = \frac{1.5\text{kV}}{\text{mm}}\ 0.8\text{mm} = 1.2\text{kV}. \tag{2.5}$$

Note that the example safety factor of 50% is quite conservative and was slightly exceeded in the experimental work of this paper, without any noticeable detriment.

2.1.1.4 Coupling Capacitor Area and Frequency

As shown in Chapter 1, electric field in the coupler gap is proportional to current, and inversely proportional to frequency and coupler area according to

$$E = \frac{I_{ac} g}{\omega A \epsilon g} = \frac{I_{ac}}{\omega A \epsilon} = \frac{I_{ac}}{2\pi f A \epsilon}. \tag{2.6}$$

In the interest of safe operating limits, this can be rewritten in terms of maximum values as

$$E_{maximum} = \frac{I_{ac,maximum}}{2\pi f A \epsilon}. \tag{2.7}$$

Operation in a dielectric different than air, such as oil [54], [69], can boost the permittivity ε and allow higher current for a given electric field. However, in the case that permittivity is fixed, the main variables here for a given load current requirement are area *A* and frequency *f*. At this point, the design flow must follow a constraint hierarchy which is determined by the specific CPT application. I.e. the frequency may be constrained by the available power electronics or EMI concerns, requiring that the coupler area be scaled as necessary. Conversely, the frequency may be variable according to the designer's choice, while the overall coupler area is limited by mechanical space constraints in the system.

In early rotational CPT experimentation, prior to the widespread availability of GaN and SiC wide bandgap semiconductors, the primary bottleneck of CPT capability was frequency. Per equation (2.7), this limitation on frequency necessitated a push for higher surface area, leading to large cascaded disk structures such as [61].

At the present time, especially with the availability of reliable GaN transistors, frequency is less of a limitation as evidenced by the ability to transfer 884W power at 13.56MHz in [34]. By

utilizing higher and higher frequencies, coupling capacitor area can be reduced, even with the larger gaps required in a printed circuit board capacitor structure. This reduction in coupler electrode size, in addition to the reduction in size of other passive components by using higher frequencies (i.e. the resonant inductors) leads to much more compact CPT systems.

2.1.1.5 Capacitance Prediction Based on Area

The analytical prediction of the capacitance of a given capacitive coupling structure generally starts by approximating it as a basic parallel plate capacitor [37]. The structure of the capacitor is made up of any two conducting electrodes separated by a dielectric material or vacuum, such that there is no direct contact between the conductors. The dielectric medium provides a location for an electric field to exist whenever an electrical potential exists between the two electrodes.

The conducting electrode "plates" have a given area A and are separated by a uniform gap g in the most basic scenario. The gap is filled with an insulating material with permittivity ε. Thus, the capacitance can be calculated as

$$C = \frac{A\epsilon}{g}. \tag{2.8}$$

This simple formula assumes that the separation distance g is much smaller than any dimension of the electrode area so that fringe field effects can be neglected. For small gap capacitive power transfer, this assumption is fairly accurate. It will be seen that slight deviation from this basic geometrical capacitance calculation will be needed to further improve the capacitance predictions.

It was decided to use just one single capacitive coupler disk for the rotor portion of the system, so the secondary side electrodes for both coupling capacitors would need to be co-located on each face of the rotor board. Because the printed circuit coupler will be used in a rotational application,

the electrode shape must be selected such that the rotor-to-stator electrode overlap area and resulting capacitance remains approximately constant throughout rotation. For this reason, concentric ring shaped electrodes similar to the disk concept proposed in [55] were selected. A diagram showing the geometry is shown in Figure 2-2.

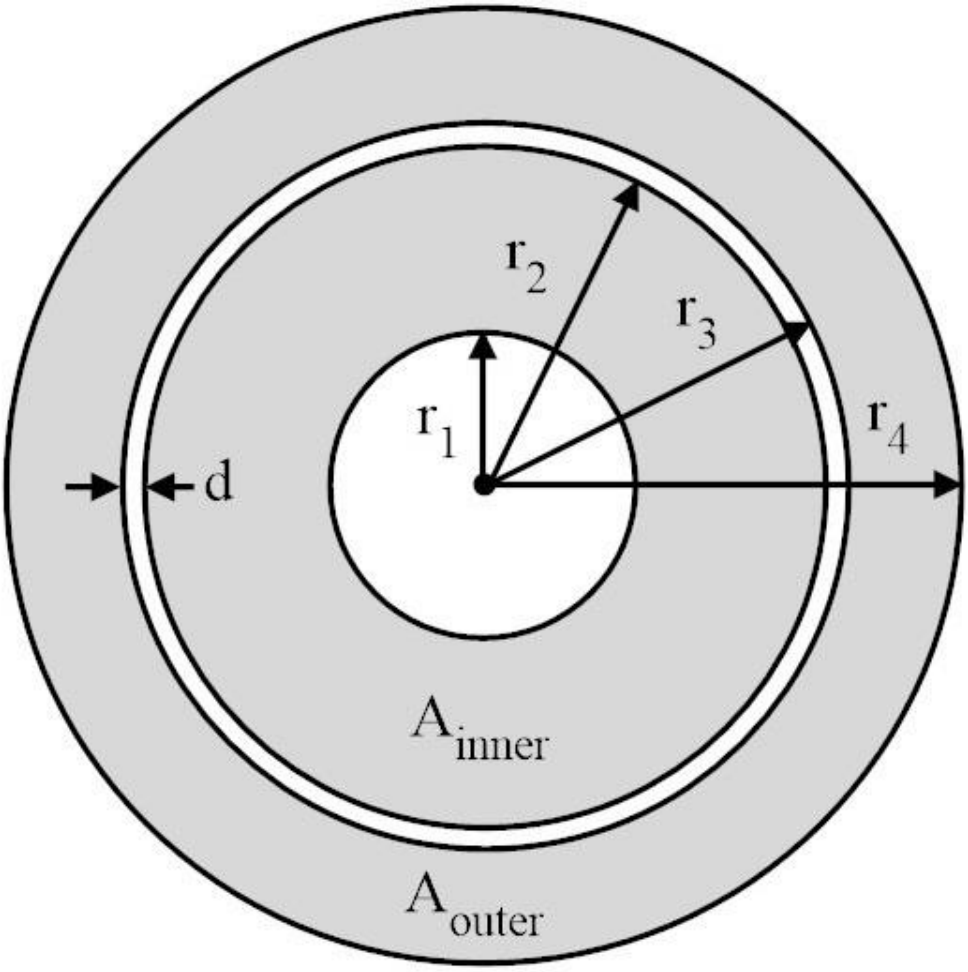

Figure 2-2: Coupling electrode geometry using concentric electrode rings.

These concentric ring-shaped electrodes each have a geometric area given by

$$A_{inner} = \pi r_2^2 - \pi r_1^2 \tag{2.9}$$

$$A_{outer} = \pi r_4^2 - \pi r_3^2 \tag{2.10}$$

where dimensions r_1, r_2, r_3, r_4, A_{inner}, and A_{outer} are those defined in Figure 2-2.

Electrode copper on standard printed circuit boards is coated with a very thin layer of insulating solder mask. In theory the solder mask increases the effective permittivity of the capacitor gap ever so slightly. Due to its small thickness when compared to the air gap, its effect on capacitance would be negligible as explained in [38].

Ultimately, since coupler overall geometry and resulting total coupling electrode area would be constrained by the dimensions of the WFSM, analytical capacitance predictions were only used to ensure that the two coupling capacitor sections are matched as closely as possible in capacitance value; not to size the absolute capacitance.

2.1.2 Application Specific Design Considerations

Once the capacitor gap, and safe peak voltages have been determined as laid out previously, the design comes down to the decision of overall area *A* and operating frequency *f* to satisfy the power output requirements. As discussed before, the design flow must follow a constraint hierarchy which is determined by the specific CPT application.

In the case of this work, the available power electronics were capable of sufficient frequency so that electrode area *A* could be made small enough to produce a CPC which, using only one double-sided rotor disk sandwiched between two stator disks, would fit inside the intended WFSM housing. The calculation of the electrode dimensions for these disks follows, based on the primary rule that the coupler assembly must be able to fit inside the housing of the WFSM.

2.1.2.1 Electrode Dimension Constraints

The overall physical dimensions of the coupler are constrained by the physical size of the wound field machine in which it will be installed. Though preliminary versions of the PCB CPC have been mounted on the exterior of the WFSM housing for serviceability and experimentation, the end goal is to produce a coupler structure that can be integrated inside the machine housing. Because of this, **the outer radius of the outer coupling electrode, r_4 in Figure 2-2, was sized so that the CPC could fit inside the end bell of the WFSM**.

The rotating power-receiving PC board of the capacitive power coupler (referred to as the CPC rotor) is electrically connected to the rotating field winding load via wires passing through a bore in the center of the shaft. Therefore it makes sense to mount the rotating rectifier components near the inside diameter of the rotor board near the shaft, as shown in Figure 2-3.

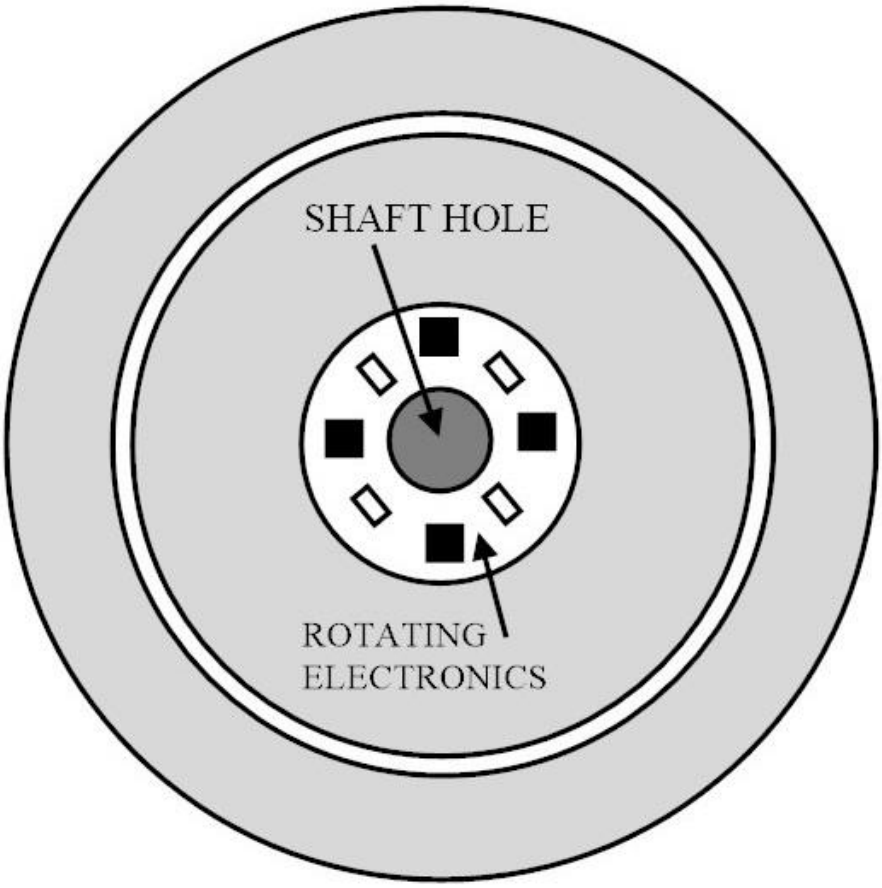

Figure 2-3: Location of rotating electronics and shaft through-hole on the CPC rotor PCB.

Centrifugal forces applied to electronic components are also greatly reduced by mounting them near the ID of the rotating coupler board. **The inner radius of the inner electrode, r_1 in Figure 2-2, was sized by the space required for rotating power electronics around middle portion of the rotor board**.

With inner and outer radius limits determined as described above, the total area of the circular printed circuit boards that can be devoted to the capacitor electrodes is then known. In the case of the boards presented in this work, the inner radius of the active coupling area was r_1 = 38.1 mm (1.5 inches), and the outer radius of the coupling area was r_4 = 101.6 mm (4 inches).

The shaft passes through a hole in the center of the board with a diameter of 22.2 mm (7/8”). The rotor board would be mounted to a hub on the shaft, and the pair of stator boards, with identical matching electrodes, would be mounted to the WFSM housing.

With r_1 and r_4 determined by mechanical constraints, the intermediate radii r_2 and r_3 would then be calculated in order to best balance the capacitances between the inner and outer capacitor sections. Before the exact electrode dimensions are finalized, the concept of fringe fields needs to be addressed:

2.1.2.2 Fringe Field Effects on Capacitance

Fringe field effects on capacitance are proportional to the capacitor gap; insomuch as the fringing effects have a greater percentage impact on total capacitance for larger capacitor gaps, while being less significant for smaller gaps (which better resemble a simple parallel plate capacitor.) Since this fully non-contact coupler structure has a gap distance which is non-negligible compared to the overall electrode size, the gap must be taken into account in order to incorporate fringing effects into the capacitance predictions for a given electrode geometry. The basic geometric copper area of an annular ring electrode is given by:

$$A = \pi r_{\text{outer}}^2 - \pi r_{\text{inner}}^2. \tag{2.11}$$

Fringe fields were accounted for by adding the length of the capacitor gap to the inner and outer radii of the electrode rings, thus calculating an *effective area*, A_{eff} for capacitance predictions, as follows:

$$A_{\text{eff}} = \pi(r_{\text{outer}} + g)^2 - \pi(r_{\text{inner}} - g)^2. \tag{2.12}$$

A visual description of the approximation made can be seen in Figure 2-4. The actual electrodes have fringe fields at the edges, as shown on the left hand side (I.) These fringing fields contribute to the capacitance but are difficult to accurately incorporate into an analytical capacitance prediction. It was found that a fairly close approximation was to add the length of the gap, g, to inner and outer dimensions while calculating ring electrode area, A_{eff}, as shown on the right hand side (II.) of Figure 2-4 using the equation above. This approach is commonly applied to magnetic cores as well.

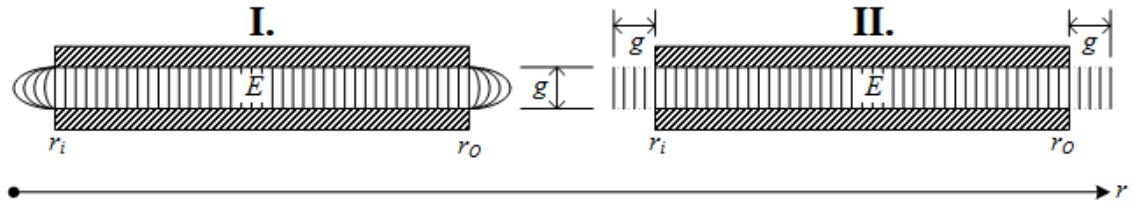

Figure 2-4: Visualization of fringe field approximation.

The radial distance between inner and outer capacitors, d as labelled in Figure 2-2, was somewhat arbitrarily set to be 3.8 mm (0.15 inch). This spacing allows some room between inner and outer electrodes to reduce stray capacitance, prevent corona and arcing, as well as provide room for machined slot features which will be discussed later. A set of equations of the form of (2.12) can then be set up to solve for r_2 and r_3, the only unknowns.

$$A_{\text{eff,inner}} = \pi(r_2 + g)^2 - \pi(r_1 - g)^2. \tag{2.13}$$

$$A_{\text{eff,outer}} = \pi(r_4 + g)^2 - \pi(r_3 - g)^2. \tag{2.14}$$

$$A_{eff,outer} = A_{eff,inner}. \tag{2.15}$$

$$d = r_3 - r_2 = 3.8\ \text{mm}, \qquad r_1 = 38.1\ \text{mm}, \qquad r_4 = 101.6\ \text{mm} \tag{2.16}$$

Using (2.15), equations (2.13) and (2.14) can be combined into one equation. Using the definition of d in (2.16), along with the definitions of r_1 and r_4 in (2.16), this can be simplified to a single variable equation which defines r_2 (and therefore also defines $r_3 = r_2 + 3.8$ mm.)

In this way, the full set of radii was found, which would be used to design the coupler printed circuit board that will be described in the experimental results chapter.

2.1.2.3 Power Handling Capability

The wound field synchronous machine used for this research requires 4 Amps field current for full field excitation, which represents approximately 675 watts into the warmed field winding resistance of 42 Ω.

Once the coupler capacitance has been set by the coupler's physical design constraints and geometry, it can be assigned a certain Amps/MHz rating by adapting equation (1.5) as follows.

$$\frac{I_{peak}}{f} = 2\pi C V_C \quad \left[\frac{\text{A}}{\text{MHz}}\right]. \tag{2.17}$$

The ac current required to pass through the coupling capacitors is governed by the characteristics of the load. In the case of this WFSM, I_{DC} = 4 A. If power factor in the tank circuit were unity, and the load was connected directly to the output of the high frequency rectifier, the peak AC current (before rectification), based on the average value of the tank current sine wave, would be expected to be $I_{peak} = \frac{\pi}{2}(4\text{ A}) = 6.3\text{ A}$. In reality, power factor in at the output of the inverter and at the input of the rectifier are not exactly unity, because of the parasitic capacitances of the semiconductor devices, causing some deviation from this.

Also, as will be described in the power electronics section of this paper, the addition of a dc-dc converter on the rotor will affect the actual peak AC current that is required in the CPC tank circuit in order to achieve the desired load current. Because of this, the simple relationship between load current and resonant tank current will not accurately reflect what is seen during experimental testing. The actual relationship between load current and ac tank current will involve additional factors such as tank power factor and dc-dc converter duty ratio as will be described in Chapter 3.

2.1.3 Reduction of Dielectric Loss and Selection of Single Phase Capacitive Coupling Circuit Topology

The focus of this paper is on the design and experimental testing of a single phase capacitive power coupler constructed solely of printed circuit boards. Prior to the construction of this final prototype, a three phase topology was also conceptualized, prototyped, and tested. It is useful to briefly discuss the reasons for this design venture, as well as the loss mitigation techniques that were discovered during its development which can be directly applied to the present single phase version.

Because of the recent successes with the 3-phase linear bearing experimental work described in [32], [39], [54], the first prototype printed circuit board capacitive power couplers also used a three phase circuit topology. The rotor and stator boards had three matching concentric pairs of capacitor electrodes, calculated using a set of equations very similar to (23)-(26) expanded for a set of three electrodes rather than two. Photos of the initial three phase prototype are shown in Figure 2-5.

Figure 2-5: Initial three-phase capacitive power coupler prototype rotor (left) and one of two stator disks (right).

In theory, the polyphase topology makes better use of the available coupling capacitors, much in the same way that polyphase utility power is known to better utilize transmission line conductors than single phase transmission.

This theory holds true in tightly coupled CPT systems, such as the linear bearing/rails of [32], [39], [54], where parasitic capacitances are much smaller than the actual coupling capacitances. When the three phase printed circuit board CPC in Figure 2-5 was prototyped, it was quickly seen that the ratio of undesired parasitic capacitance to desired coupling capacitance was much worse than what was seen with the linear rails. During power testing, efficiency using the first three phase prototype was poor (~70%) due to the excessive current circulating in the stray capacitances between electrodes of adjacent capacitor sections.

In an attempt to reduce dielectric losses, two key mitigation techniques were investigated:

- Finite element analysis (FEA) was used to investigate the effects of removing excess dielectric material between ac electrodes, as well as improving trace routing in the areas where losses were seen to be most severe
- A precision dielectric test fixture and impedance analyzer was used to experimentally measure the potential loss reduction of upgrading to a lower-loss high frequency printed circuit board dielectric material than conventional FR4.

2.1.3.1 Finite Element Dielectric Loss Analysis

It was seen experimentally in early prototypes that dielectric heating of the glass-filled composite printed circuit board substrate material (FR4) was a prime contributor to overall CPC system inefficiencies. The volume located between any two opposite polarity ac electrodes on the printed circuit board coupler is filled with dielectric material. The dielectric material may either be FR4 (in the case of a standard circuit board) or air (if the FR4 has been machined or "slotted" out). FR4 occupying these high ac field regions leads to losses due to repeated re-polarization of electric dipoles at high frequency. If the dielectric material is air, these losses are negligible, because the dielectric constant and dissipation factor of air is very similar to vacuum, which is a lossless dielectric.

The common circuit board substrate FR4, which has a non-negligible dielectric constant and dissipation factor, experiences dielectric heating when placed in an intense ac electric field. With this in mind, two design changes were considered, with the end goal of reducing dielectric heating and losses in the CPC boards. One design change would be **slotting away of dielectric material**

between adjacent electrodes of opposite polarity. The other change would be the **elimination of overlapping traces** by switching from a 4-layer board design to a 2-layer design.

Finite element analysis (FEA) in Ansys Maxwell software was performed to help visually explain the improvement that would be seen experimentally from each of these changes.

2.1.3.1.1 Board Slotting between Adjacent Phase Conductors

First, the effects of slotting out FR4 material between adjacent phase traces were investigated. These machined slots would be located in the gap, of width *d*, which is shown between the inner and outer electrode areas in Figure 2-2. The desired effect of this design change was to reduce electric displacement field intensity in the radial direction between one phase's electrode ring edge and the edge of the adjacent one. A simulation was set up in Ansys Maxwell. The geometry simulated is similar in layout and scale to the actual PCB's with slight changes made for better visibility. The electric displacement field (D-field, units of Coulombs/m^2) was plotted across the 2-dimentional structure and is shown in Figure 2-6.

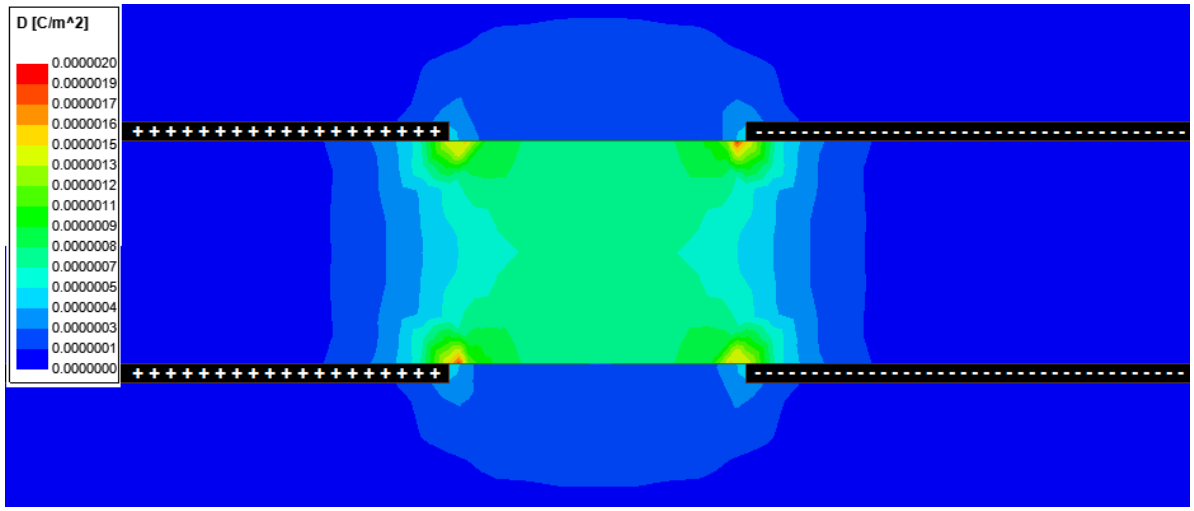

(a)

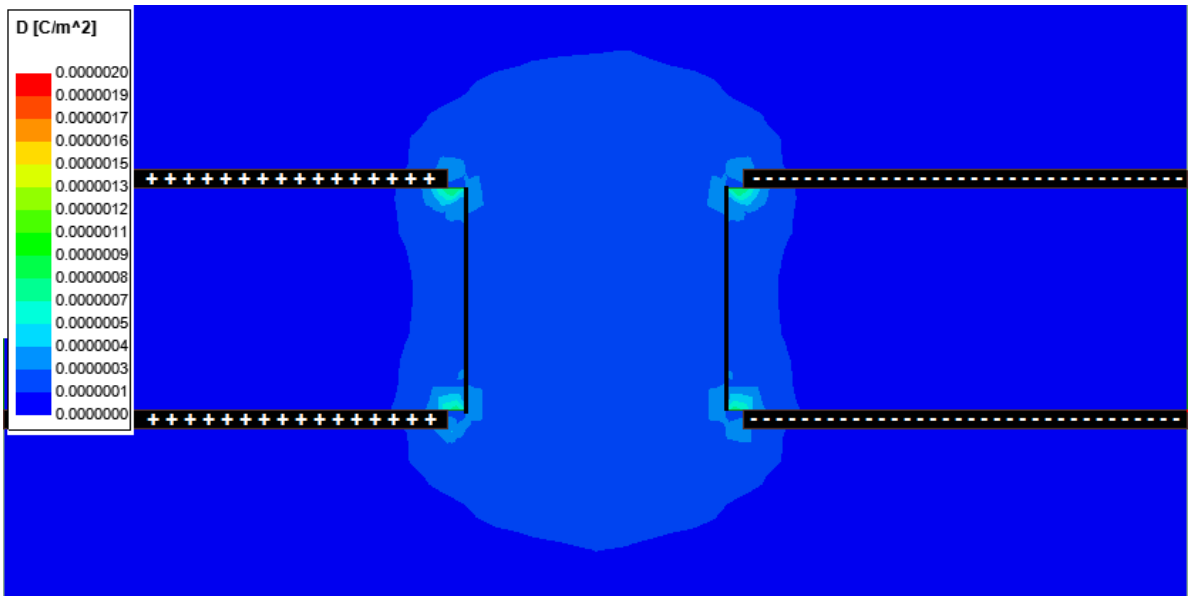

(b)

Figure 2-6: FEA plots of displacement field intensity showing field between adjacent phase rings on unslotted CPC (a) and between the same phase rings on a slotted CPC (b).

Both simulations used the same excitation voltage, the same electrode arrangement/spacing, and both maps are displayed with the same color scale range. It is clear from the simulated field maps that D-field intensity in the majority of the volume between electrodes would be reduced by a factor of approximately 4x (correlating with the FR4 permittivity) between the un-slotted version and the slotted version, which would greatly reduce dielectric losses in these regions of the board. Considering these simulation results, it was decided to slot out the dielectric material between adjacent electrodes for future prototypes.

The physical implementation of the changes made as a result of the observations of Figure 2-6 can be seen in Figure 2-7, where the FR4 between the rings was slotted away, except for a few mechanical spokes.

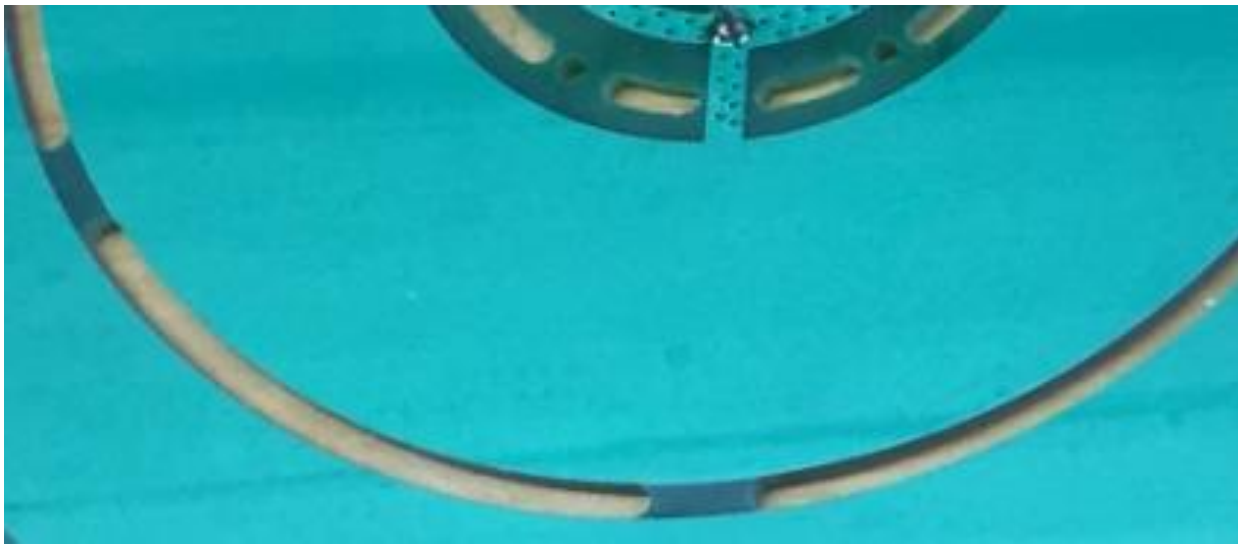

Figure 2-7: Close-up photograph of "slotting" between capacitor electrodes. Also seen is the slotting between the inner electrode and the rotor electronics section.

The majority of the space between the outer electrode ring and the inner electrode ring, where the highest magnitude electric field exists at high frequency, was slotted out, leaving only air as a dielectric material and eliminating losses. As seen at the top of the photo, some FR4 material was even removed between the inner electrode and the inner rotating power electronics section of the board. In this way, capacitive coupling between the high frequency coupling electrode and the more sensitive low voltage rotor electronics (described in the next chapter) was minimized.

FR4 “spokes” were left physically attaching the portion of the board with the outer electrode to the portion containing the inner electrode. These spokes provide mechanical support for the outer portion of the rotor board. Additionally, one of the spokes was used for the passage of a copper trace electrically connecting the outer electrode ring to the inner rotor electronics area. FEA was also used to determine the routing of this trace, as will be described in the next section.

2.1.3.1.2 Elimination of Overlapping Traces between Phases

The second PCB CPC design alteration considered for reduction of dielectric losses was the elimination of any axially overlapping traces of differing phase/polarity. The original rotor board design shown in Figure 2-5 used radially extending traces located in the 2nd and 3rd layer of a 4-layer board to make electrical connection between outer electrode rings and inner rectifier components. In order to eliminate overlap, gaps can instead be left in the inner electrode rings to allow traces to pass radially through, connecting outer rings to inner rectifier components.

Electrostatic simulations were again carried out using Ansys Maxwell software; this time, to show the reduction in D-field intensity resulting from the elimination of trace overlap. The color coded D-field maps can be seen in Figure 2-8.

The simulation results make it clear that elimination of overlapping traces has a similarly drastic effect on the intensity of electric displacement field (~3-4x reduction) in the FR4 insulating material. Based on this reduction of displacement field (and therefore ac losses), future coupler designs would incorporate both changes: slotting and careful routing to avoid overlap.

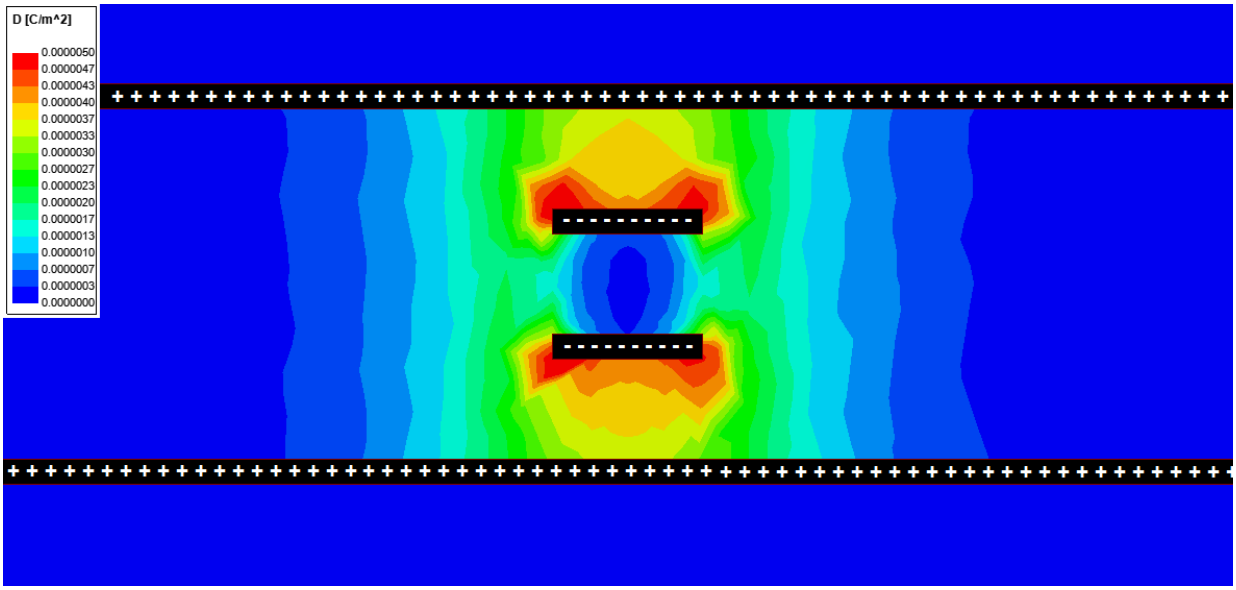

(a)

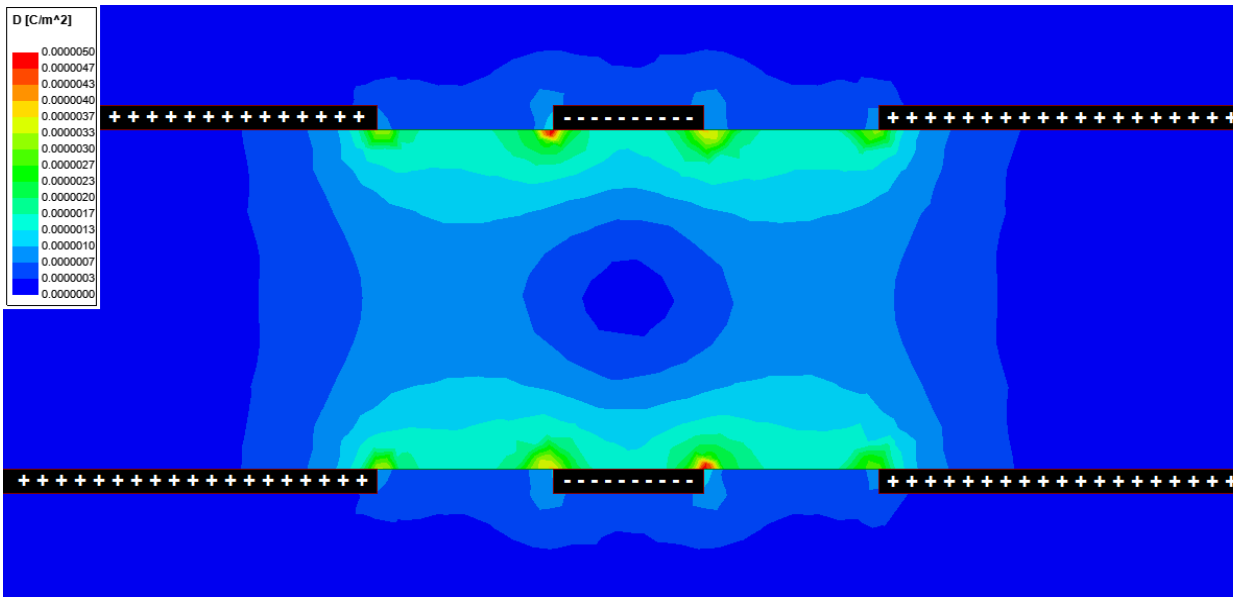

(b)

Figure 2-8: D-field comparison between original PCB CPC with overlapping phase traces in 4-layer board and later prototype with non-overlapping traces on 2-layer board. Excitation 100vdc, same color scale used for both cases.

A photo showing the physical implementation of these changes can be seen in Figure 2-9. Here, a two-layer board was manufactured instead of the four-layer board previously used. In order to make connection between the outer electrode are and the inner electronics section, a gap was left in the inner electrode area, through which a trace could pass, on the same layer as the inner electrode. The same was used to connect the outer ring on the other side of the two-sided rotor board to the inner electronics, as proposed in the FEA simulation of Figure 2-8.

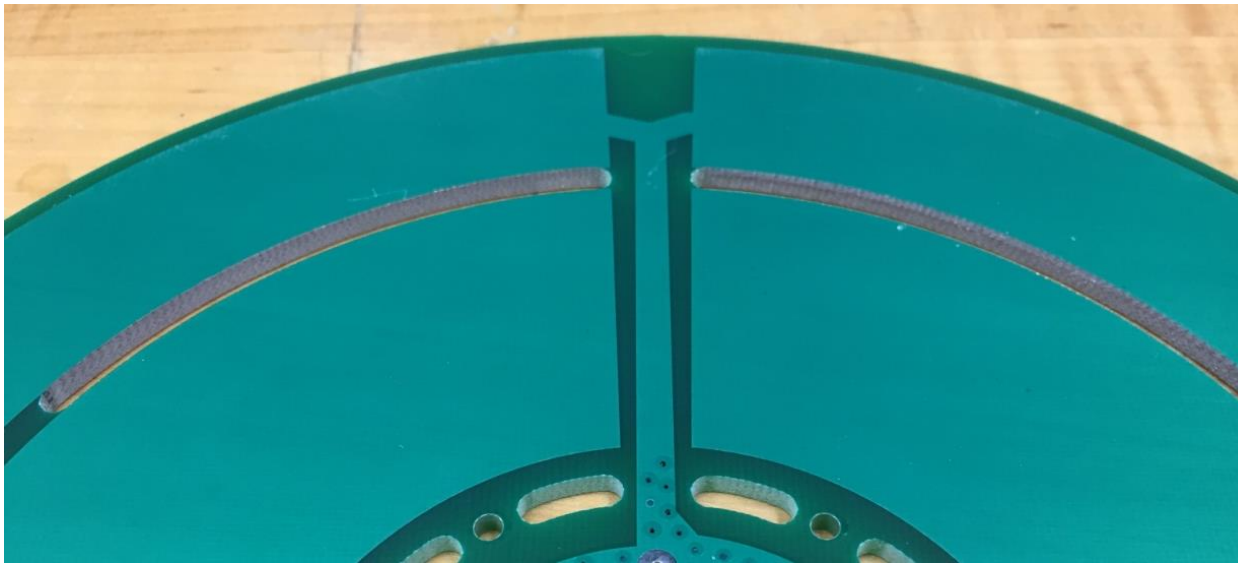

Figure 2-9: Photo showing connection of the outer electrode to the inner rectifier and electronics area. Also shown is the slotting highlighted in the previous section.

2.1.3.2 Explanation of Efficiency Gains from these Changes

A particular dielectric material, such as the FR4 fiberglass epoxy material used for printed circuit boards, has a given complex relative permittivity given by:

$$\epsilon_r = \epsilon_r' - j\epsilon_r''. \tag{2.18}$$

The dielectric also has a dissipation factor or loss tangent given by

$$D.F. = \tan(\delta) = \frac{\epsilon_r''}{\epsilon_r'} \tag{2.19}$$

which gives the proportionality of the real and imaginary parts of the relative permittivity ε_r. When an electric field *E* of a particular magnitude and direction is applied to a dielectric material, the electric dipoles within the material align, as shown in Figure 2-10.

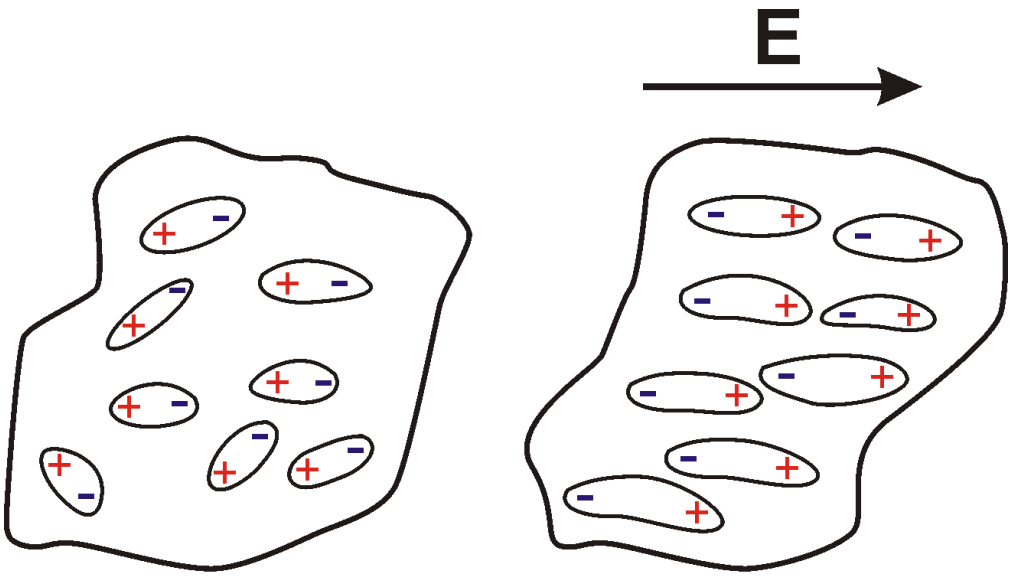

Figure 2-10: Random orientation of electric dipoles without exposure to an *E* field (left) and after exposure to *E* field (right) resulting in alignment of dipoles.

The magnitude and direction of the alignment of these dipoles can be described by the electric displacement field, *D*.

The volumetric power density dissipated in the process of displacing electric charges within a dielectric exposed to an alternating electric field *E* at a particular frequency ω, is given by

$$W_{vol} = \frac{P_{loss}}{Volume} = \omega E^2 \epsilon_0 \epsilon_r'' = \omega E^2 \epsilon_0 \epsilon_r' \tan(\delta). \quad (2.20)$$

As such, power lost (and inefficiency incurred) by dielectric losses is proportional to the square of the electric field, and also proportional to the AC frequency applied. Since frequencies used in the CPC system are relatively high (for switched power electronics), and so are the applied voltages

(and therefore electric field E given the physical dimensions of the system), it is of key importance to make effort to reduce ε and tan(δ) in the volume between electrodes of different phases or polarity; thus minimizing displacement field $D = \epsilon_0 \epsilon_r E$, as shown in Figure 2-6 and Figure 2-8. Both simulations displayed D-field reductions between electrodes of approximately 3-4x, which is most likely directly connected to the change from FR4 (ε_r = ~4) to air (ε_r = ~1), according to the $D = \epsilon_0 \epsilon_r E$ relationship.

2.1.3.3 FEA Conclusion and Selection of Single Phase Topology

Based on what was seen in the FEA simulations, a second three-phase prototype was constructed which implemented the design changes discussed. Slots were cut in the gaps between AC electrodes, and a 2-layer board was used rather than overlapping traces in a 4-layer board. Photos of this improved 3-phase prototype are shown in Figure 2-11.

Figure 2-11: Improved 3-phase prototype with slotting and elimination of trace overlap.

This improved three phase prototype showed notable improvements in ESR over the original 3-phase prototype, due to the reduction in dielectric losses as a result of the changes made based on FEA observations. A comparison of ESR of the resonant tank circuit using both 3-phase prototypes can be seen in Figure 2-12.

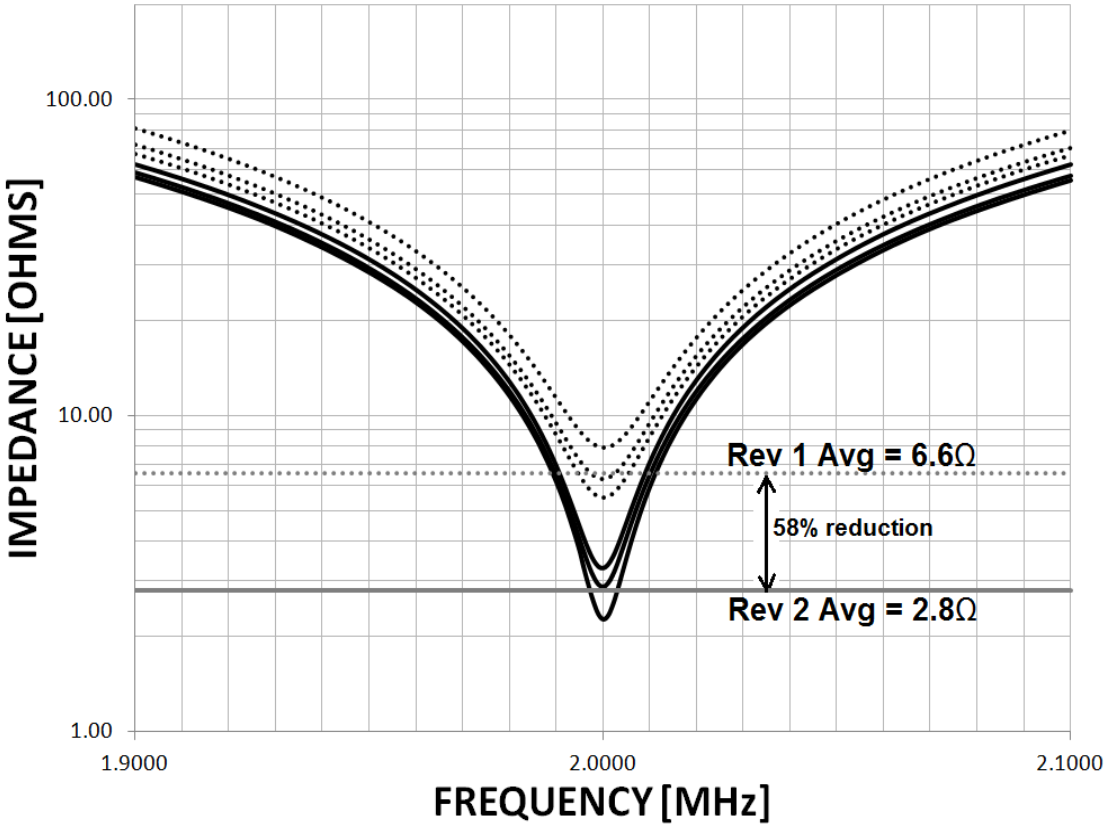

Figure 2-12: ESR comparison between 3-phase coupler prototypes, via Bode plot. Horizontal bars represent the average impedance of the three phase legs, at the resonant frequency of 2MHz.

A 58% reduction in ESR was seen between the older version and the improved version. Everything else in the tank circuit (inductors, etc) was identical between the two tests.

Though improvement was seen in the 3-phase coupler system after implementing the changes suggested by FEA simulations, the 3-phase system still has a major disadvantage compared to a single phase coupler. On a three phase coupler board like the ones shown in Figure 2-5 and Figure 2-11, there is essentially twice the inter-electrode gap region that exists in a single phase layout like Figure 2-2. Because of this, a single phase design was chosen for the work described in this paper, and as will be seen in the experimental results to follow, this choice resulted in a highly efficient system, that unlike earlier prototypes, was able to achieve the 4.0Amp WFSM field current target. The single phase circuit topology also greatly simplifies tuning of the resonant circuits, which would be key for the use of closed loop frequency control to ensure soft switching, as will be described in the next chapter. A summary of the pros and cons which support the decision to go with a single phase CPC are shown in TABLE 2 below.

TABLE 2. MOTIVATION FOR SELECTION OF A SINGLE PHASE CPC TOPOLOGY

	Capacitance Utilization	Drive Electronics & Passive Components	Leakage Capacitance and Dielectric Loss	Tuning Difficulty and Circulating Current Issues
Single Phase	**Worse**	**Simpler**	**Better**	**Simpler**
Three Phase	**Better**	**More complex**	**Worse**	**More complex**

2.1.3.4 Investigation of Alternative PCB Materials

Efficiency gains predicted (using FEA) by mechanical board design changes, which were intentionally made to reduce electric displacement field wherever possible, prove that the dielectric constant and loss tangent of the printed circuit board substrate play a significant role in CPC system losses. For this reason, an investigation was done regarding the possible use of alternative PCB substrate materials to further reduce losses via a change in dielectric constant and loss tangent.

One well known low-loss high-frequency printed circuit material is called Rogers 4000, and is commonly used for high frequency communications electronics and antennas. The properties of Rogers 4000 are fairly well known at 100MHz+ frequencies, as used in RF communications, but there is little data available in the integer megahertz operating space. Thus, careful measurements were taken in the lab to quantify the potential benefits of using such a material for the purpose of capacitive power transfer at integer MHz frequencies. This could be a benefit at the ~2MHz frequencies used in the research of this paper, but would be even more beneficial if higher frequencies are used in future work, such as the 6.78MHz ISM band.

A parallel plate solid dielectric test fixture was used in conjunction with an impedance analyzer to compare dielectric properties between similar-thickness samples of FR4 and Rogers materials. The test fixture is shown in Figure 2-13, holding samples of FR4 (left) and Rogers 4000 (right).

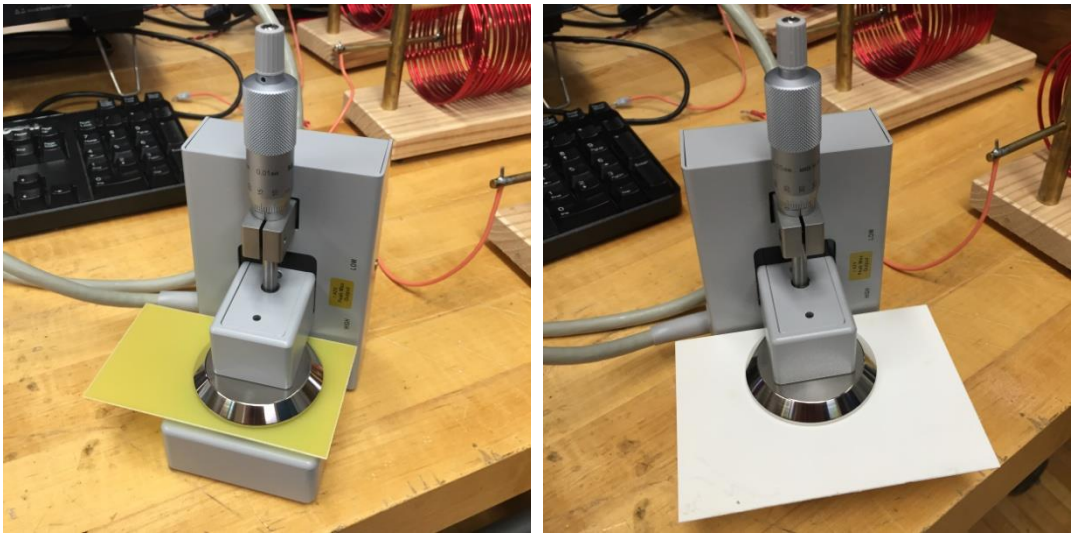

Figure 2-13: Dielectric test fixture holding non-plated samples of FR4 (left) and Rogers 4000 (right) printed circuit board materials.

Based on the range of frequencies that lie within the capabilities of the power electronics used for this work, the frequency range for these measurements was capped at 5 MHz. The thickness of the FR4 sample was 0.044", and the Rogers sample was 0.032". Using measured Bode plots of capacitance C and dissipation factor D, along with guidelines from the test fixture's operating instructions [70], ε_r and D_f were calculated from capacitance and dissipation measurements using the following equations.

$$\epsilon_r = \frac{t_a \times C_p}{A \times \epsilon_0} = \frac{t_a \times C_p}{\pi \times \left(\frac{d}{2}\right)^2 \times \epsilon_0} \tag{2.21}$$

$$D_f = D \tag{2.22}$$

where A is area in m^2, C_p is capacitance measured in Farads, d is diameter of the guarded electrode in the test fixture (38×10^{-3} meters), and t_a is average thickness of the test material (listed above for the two materials tested).

At the target operating frequency of 2 MHz, the FR4 material had $\varepsilon_r = 4.4$ and $D_f = 0.021$ while the Rogers material had $\varepsilon_r = 3.4$ and $D_f = 0.003$. Plots of relative permittivity and dissipation factor, vs. frequency are shown in Figure 2-14 and Figure 2-15, respectively.

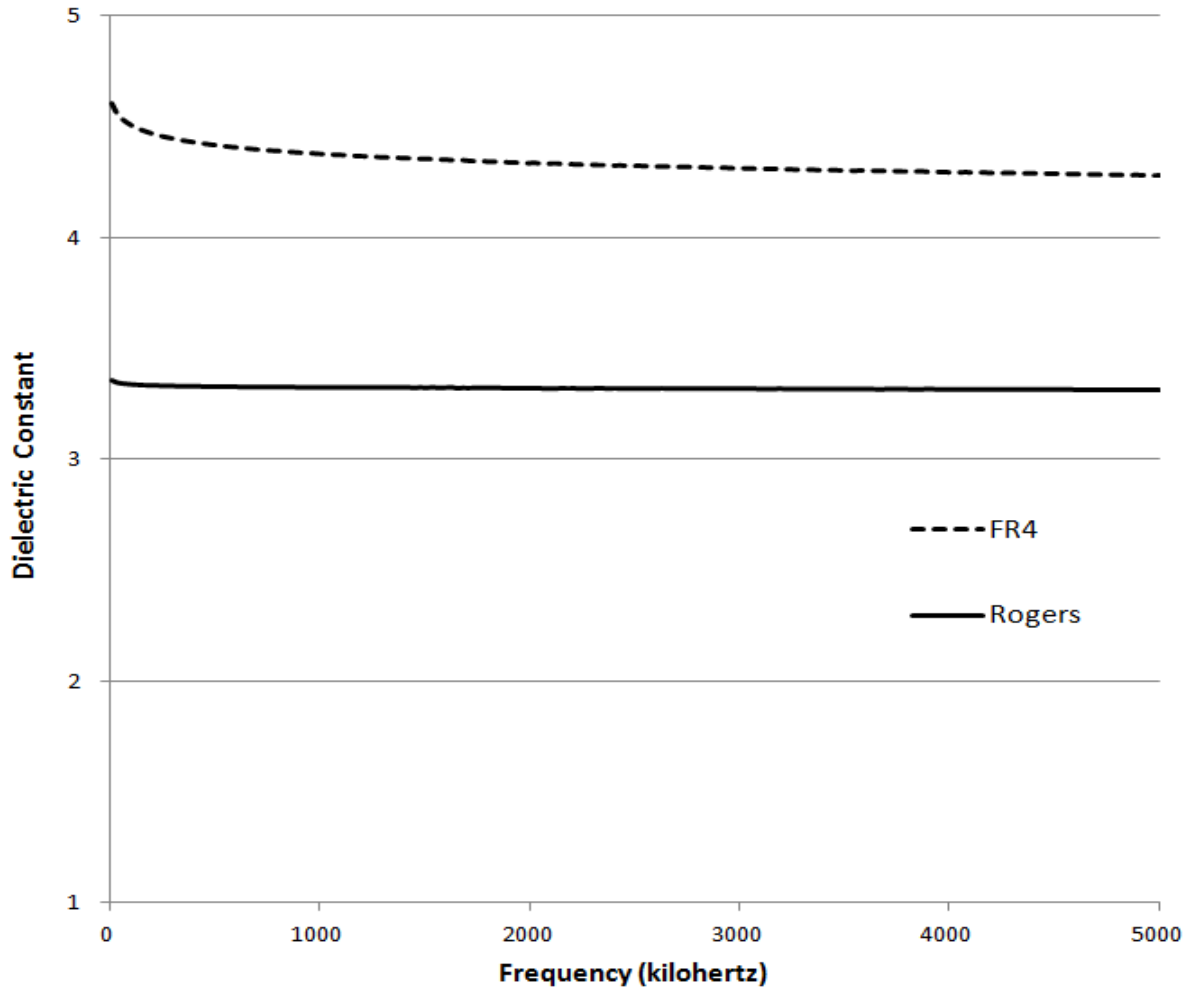

Figure 2-14: Dielectric constant comparison between FR4 and Rogers PCB materials.

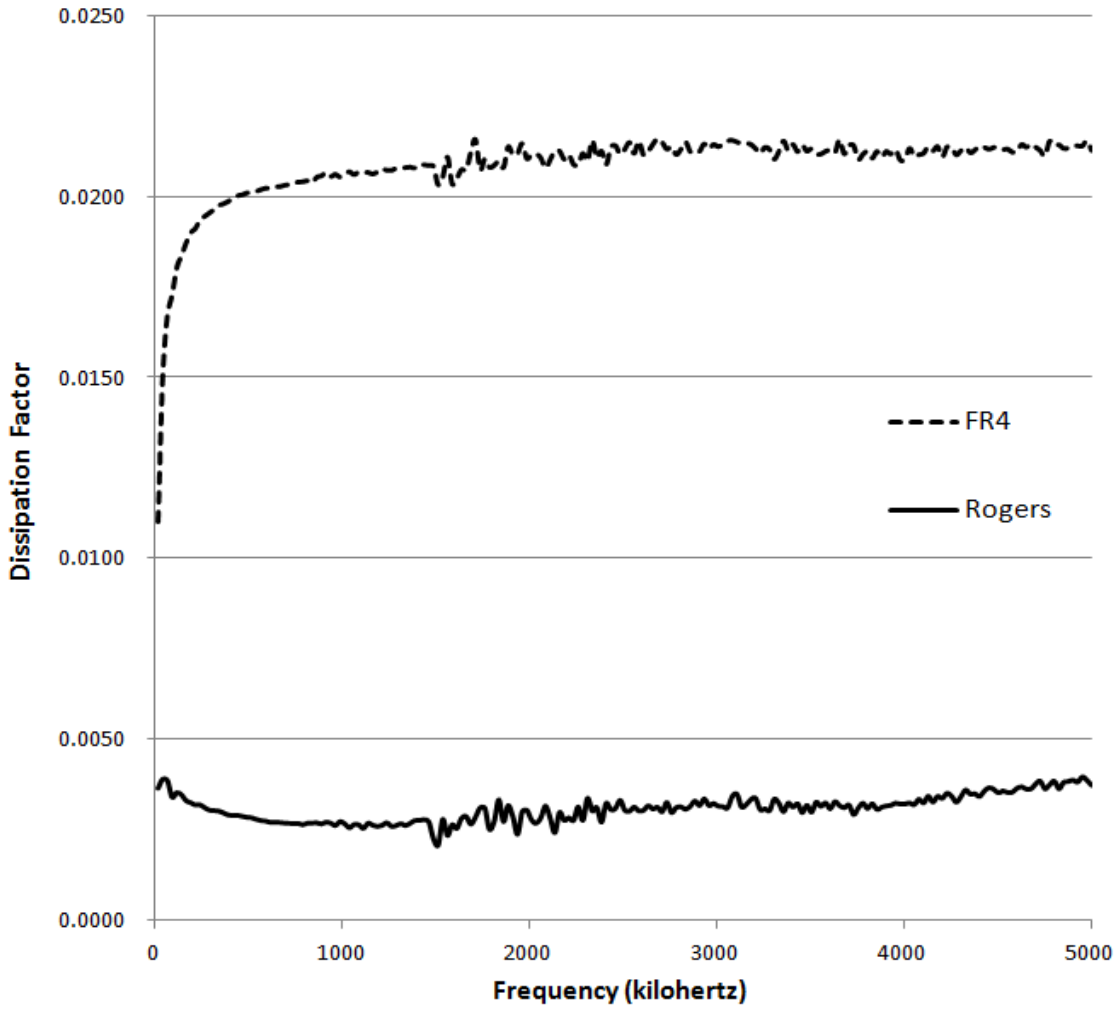

Figure 2-15: Loss tangent / dissipation factor comparison between FR4 and Rogers PCB materials.

It is clear that the use of Rogers material would most likely benefit the efficiency of the CPC system to some degree; however, the cost of obtaining large CPC boards of the Rogers material makes it prohibitively expensive, at least in the small quantities needed for experimental work. It is quite possible that the price for large volume manufacturing would be affordable enough to warrant the added efficiency gains. The use of these more costly materials could also be justified

in some high-end automotive or aerospace applications where performance outweighs price point. No sample CPC PCB's were ordered using the Rogers materials, since one of the primary goals of this capacitive power coupler design was low-cost and ease of manufacture. However, the mechanical changes (slotting between electrodes and elimination of overlapping traces of opposite polarity) were implemented in the prototype whose experimental results are described in this paper. Future work in this area, especially in the 6.78MHz ISM band, may justify the added expense of the lower loss Rogers substrate, as dielectric losses scale with frequency per (2.20).

Power Handling Capability

The wound field synchronous machine used for this research requires in excess of 4 Amps field current for full field excitation, which represents approximately 675 watts into a warmed field winding.

Once the coupler capacitance has been set by the coupler's physical design constraints and geometry, it can be assigned a certain Amps/MHz rating by adapting equation (1.5) as follows.

$$\frac{I_{peak}}{f} = 2\pi C V_C \ \left[\frac{\text{A}}{\text{MHz}}\right]. \tag{2.23}$$

The ac current required to pass through the coupling capacitors is governed by the characteristics of the load. In the case of this WFSM, I_{DC} = 4 A. Assuming unity power factor in the tank circuit, as would be expected when operating it exactly at its resonant frequency, the peak AC current (before rectification), based on the average value of the tank current sine wave, would be expected to be $I_{peak} = \frac{\pi}{2}(4\text{ A}) = 6.3\text{ A}$. In reality, power factor in at the output of the inverter and at the input of the rectifier are not exactly unity, because of the parasitic capacitances of the semiconductor devices, causing some deviation from this.

Also, as will be described in the power electronics section of this paper, the addition of a dc-dc converter on the rotor will affect the actual peak AC current that is required in the CPC tank circuit in order to achieve the desired load current. Because of this, the simple relationship between load current and resonant tank current will not accurately reflect what is seen during experimental testing.

2.1.4 Coupler Inter-Electrode Partial Capacitances

In order to establish an accurate equivalent circuit of the coupler system, careful measurements of capacitance between electrodes on the printed circuit boards must be taken. These measurements include both the desired coupling capacitances and the undesired parasitics or leakage capacitances. Capacitances exist between all combinations of electrodes, as well as between each electrode and ground, as shown in Figure 2-16.

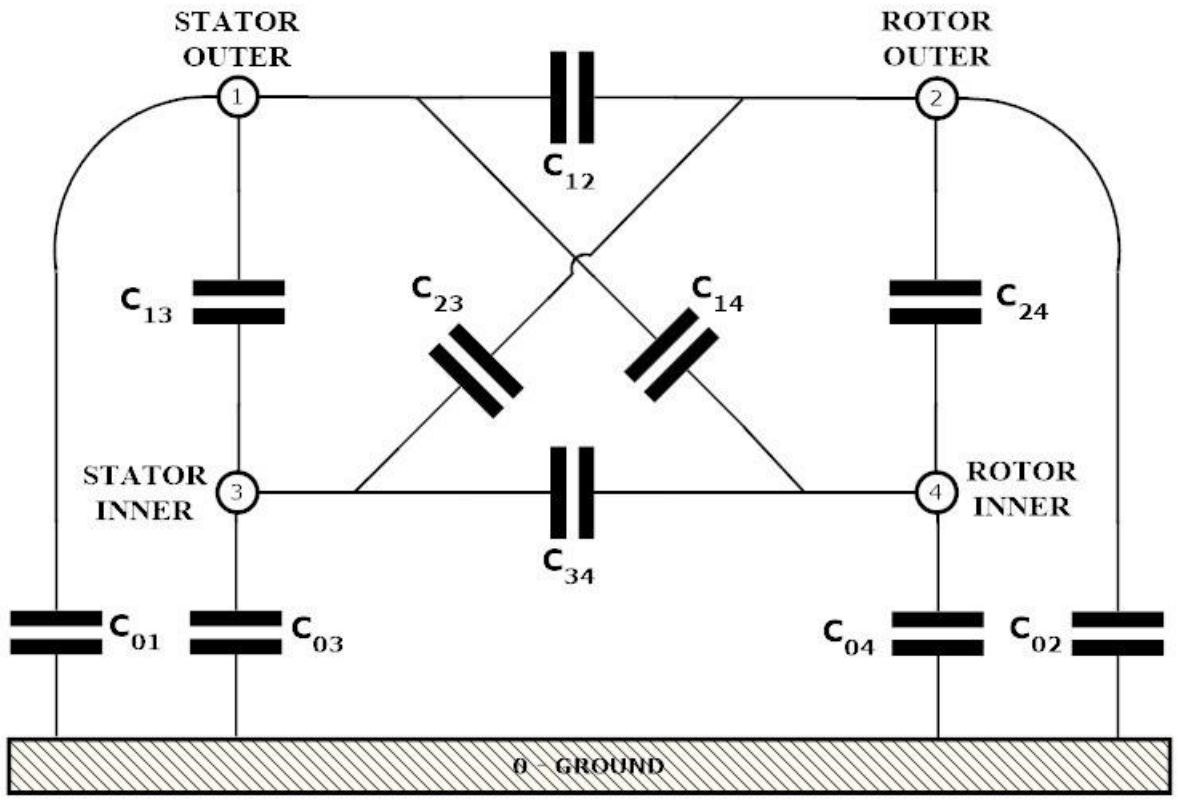

Figure 2-16: Diagram of partial capacitances between all combinations of electrodes and ground.

A method is laid out in [71] which determines each "partial capacitance" labeled in Figure 2-16 using a set of "total capacitance" measurements. These partial capacitances cannot be directly measured accurately, unless there are only 2 electrodes in the entire system. This is because with 3+ electrodes there are always parallel capacitances which alter the measured value between two electrodes. The partial capacitances reflect the actual energy storage capability due to the electric field lines between the two electrodes in question, without influence from other electrodes, as if the other electrodes in the system didn't exist. Therefore, the knowledge of the partial capacitances is useful in determining how current will flow through the coupler circuit, and aid in developing an accurate equivalent circuit.

For an $(N + 1)$ – electrode system, there exist $N\,(N + 1) / 2$ partial capacitances. In this case, for a $N + 1 = 5$ electrode system where $N = 4$ there are 10 partial capacitances, as shown in Figure 2-16. Thus, there are 10 "total capacitances" which must be experimentally measured to determine them.

For the purposes of clear notation, the 5 electrodes, starting with ground, are denoted 0, 1, 2, 3, and 4, as shown in Figure 2-16.

The first set of total capacitances are measured by shorting together all but one electrode and measuring the single capacitance between the isolated electrode and the set of shorted electrodes. This first connection scheme makes up 5 of the 10 total required capacitance measurements, as there are 5 individual electrodes in the system which can be isolated one at a time. These measurements were denoted C_{0_1234}, C_{1_0234}, C_{2_0134}, C_{3_0124}, and C_{4_0123}. For all measurements, the underscore in the subscript separates the two groups of numbered electrodes between which the capacitance has been measured. For all measurements, the grounded outer shield, or "low-side"

clip on the impedance analyzer probe is connected to whichever group of electrodes contains “0”, or ground in the system under test.

The second and final set of total capacitances are measured by shorting various combinations of two electrodes and measuring from there to the remaining three electrodes, which are also shorted together. These measurements make up the remaining 5 of the 10 required measurements. The measurements are denoted C_{01_234}, C_{12_034}, C_{23_014}, C_{34_012}, and C_{04_123}. Again, the low side of the impedance analyzer is connected to whichever shorted group of electrodes contains “0” or ground.

The physical meaning of these total capacitance measurements, which hints at the way the individual partial capacitances can be mathematically solved for, can be shown by example. In the case of C_{0_1234}, electrodes 1, 2, 3, and 4 are shorted together and connected to the “high” side of the impedance analyzer. The “low” side of the impedance analyzer is connected to electrode 0 which is the earth-grounded shell of the WFSM. By shorting together electrodes 1, 2, 3, and 4, partial capacitances C_{12}, C_{13}, C_{14}, C_{23}, C_{24}, and C_{34} which exist between electrodes 1, 2, 3, and 4, are eliminated from the measurement. Therefore, $C_{0\_1234} = C_{01} + C_{02} + C_{03} + C_{04}$.

For the example of C_{01_234}, the shorting of electrodes 0 and 1 eliminates partial capacitance C_{01}, while the shorting of electrodes 2, 3, and 4 eliminates partial capacitances C_{23}, C_{24}, and C_{34}. Based on the remaining partial capacitances, the equation for this total capacitance is found to be $C_{01\_234} = C_{02} + C_{03} + C_{04} + C_{12} + C_{13} + C_{14}$.

Similar equations can be set up for all the measured total capacitances. The resulting system of 10 equations can be solved to find the 10 desired partial capacitances. In matrix form, the system is given as:

$$\begin{bmatrix} 1 & 1 & 1 & 1 & 0 & 0 & 0 & 0 & 0 & 0 \\ 1 & 0 & 0 & 0 & 1 & 1 & 1 & 0 & 0 & 0 \\ 0 & 1 & 0 & 0 & 1 & 0 & 0 & 1 & 1 & 0 \\ 0 & 0 & 1 & 0 & 0 & 1 & 0 & 1 & 0 & 1 \\ 0 & 0 & 0 & 1 & 0 & 0 & 1 & 0 & 1 & 1 \\ 0 & 1 & 1 & 1 & 1 & 1 & 1 & 0 & 0 & 0 \\ 1 & 1 & 0 & 0 & 0 & 1 & 1 & 1 & 1 & 0 \\ 0 & 1 & 1 & 0 & 1 & 1 & 0 & 0 & 1 & 1 \\ 0 & 0 & 1 & 1 & 0 & 1 & 1 & 1 & 1 & 0 \\ 1 & 1 & 1 & 0 & 0 & 0 & 1 & 0 & 1 & 1 \end{bmatrix} \begin{bmatrix} C_{01} \\ C_{02} \\ C_{03} \\ C_{04} \\ C_{12} \\ C_{13} \\ C_{14} \\ C_{23} \\ C_{24} \\ C_{34} \end{bmatrix} = \begin{bmatrix} C_{0\_1234} \\ C_{1\_0234} \\ C_{2\_0134} \\ C_{3\_0124} \\ C_{4\_0123} \\ C_{01\_234} \\ C_{12\_034} \\ C_{23\_014} \\ C_{34\_012} \\ C_{04\_123} \end{bmatrix}. \quad (2.24)$$

Using the Keysight 4990 impedance analyzer, the total capacitances for the printed circuit board coupler mounted on the test WFSM were found to be:

$$\begin{bmatrix} C_{0\_1234} \\ C_{1\_0234} \\ C_{2\_0134} \\ C_{3\_0124} \\ C_{4\_0123} \\ C_{01\_234} \\ C_{12\_034} \\ C_{23\_014} \\ C_{34\_012} \\ C_{04\_123} \end{bmatrix} = \begin{bmatrix} 30 \\ 323 \\ 310 \\ 305 \\ 281 \\ 326 \\ 57 \\ 601 \\ 51 \\ 307 \end{bmatrix} \text{ pF.} \quad (2.25)$$

Using these measured total capacitances, the partial capacitances were calculated using (2.24) and the "`linsolve`" command in MATLAB to be:

$$\begin{bmatrix} C_{01} \\ C_{02} \\ C_{03} \\ C_{04} \\ C_{12} \\ C_{13} \\ C_{14} \\ C_{23} \\ C_{24} \\ C_{34} \end{bmatrix} = \begin{bmatrix} 14 \\ 5 \\ 10 \\ 2 \\ 288 \\ 21 \\ 1 \\ 7 \\ 11 \\ 268 \end{bmatrix} \text{ pF.} \tag{2.26}$$

A capacitance diagram with these calculated partial capacitance values labeled for easier interpretation is given in Figure 2-17. The desired coupling capacitances C_{12} and C_{34} are shown to be well matched, which will result in acceptable voltage balance in the final implementation, since the two coupling capacitances are in series with the load and therefore share the same current. As a reality check to confirm that the measurements are reasonable, the interelectrode capacitance of the CPC stator C_{13} = 21pF is approximately double the interelectrode capacitance of the rotor C_{24} = 11pF, due to the fact that there are two stator disks, and only one rotor disk.

As a second check, it can be seen that the capacitances from the rotor electrodes to ground are much lower than those from the stator electrodes to ground, due to the fact that the stator shields the rotor from ground, as it surrounds both sides of the rotor disk. Finally, the stray capacitances from the outer electrodes to ground, on both rotor and stator, are larger in value than those from the inner electrodes to ground. This is likely due to the larger perimeter of the outer electrodes on both boards.

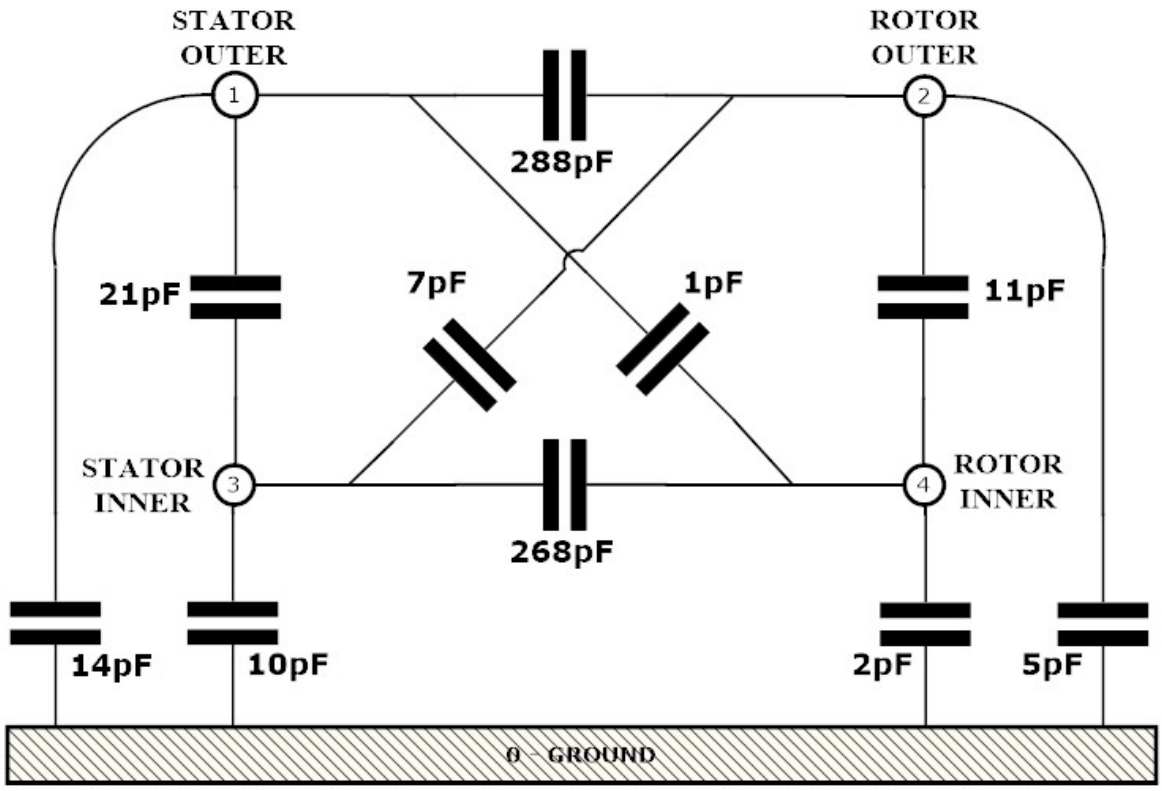

Figure 2-17: Capacitance diagram of printed circuit board CPC with partial capacitance values labeled, as calculated from total capacitance measurements using matrix algebra.

2.2 Ferrite-Cored Resonant Tank Inductor Design

As shown in photos in Figure 1-9 through Figure 1-12, among others, all previous work in capacitive power transfer discussed in the State-of-the-Art review utilized air inductors in their resonant tank circuit. Air inductors tend to have reasonable quality factor due to the lack of a permeable core, and therefore lack of core loss. Despite functioning well in isolated laboratory experimentation, air inductors' physical size and the potential for radiated EMI makes them unusable in a real-life commercial application of CPT technology. For these reasons, the design of a cored resonant tank inductor capable of handling the kVA levels required in kilowatt scale CPT was pursued.

Previous work in [72] had developed a cored inductor for power converters which was able to efficiently operate in the MHz regime at multiple amps RF current. The key development made by [72] was the distributed air gap, used to distribute air gap fringe flux along the length of the inductor, reducing eddy current losses in the coil winding conductors.

Though this inductor design proved capable of operating at the frequencies used in CPT work, its use at high-kVA levels in a resonant tank circuit required that the design of [72] be modified for high inductor voltage and multiple kVA power levels. The distributed air gap concept of was maintained, however the size of the core design was scaled up using parametric ratios to increase the winding window cross-section for high voltage wire insulation. Kapton shims were used in the distributed air gap in order to fully insulate each stacked ferrite core piece from the next in order to prevent leakage current when high AC voltages are applied from one end of the inductor core to the other. A rendering of the solid model of the core design used for this research is shown in Figure 2-18.

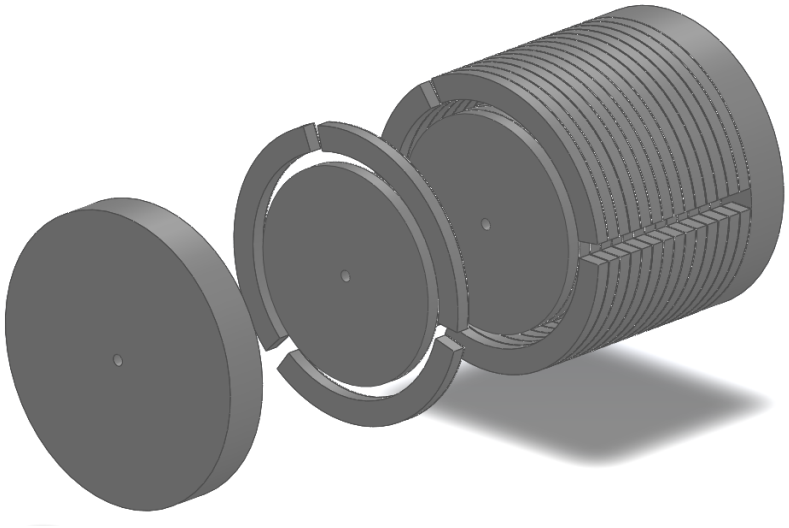

Figure 2-18: Solid model rendering of resonant inductor core.

The segmented core pieces shown were manufactured by Fair Rite Corp from their #67 material, which is optimized for MHz frequencies. As in [72], a center hole is included through the axis of all the core pieces to allow a small metal rod to be used as an alignment jig during assembly. Slots were left in the outer shell pieces to allow wire leads from inductor coils to pass through for connection into the tank circuit. Using a CNC vinyl cutter, spacers were cut out of 0.002" thick Kapton adhesive backed sheet in the shape of all core pieces to act as spacers. The inductor core was assembled as shown in the photos of Figure 2-19.

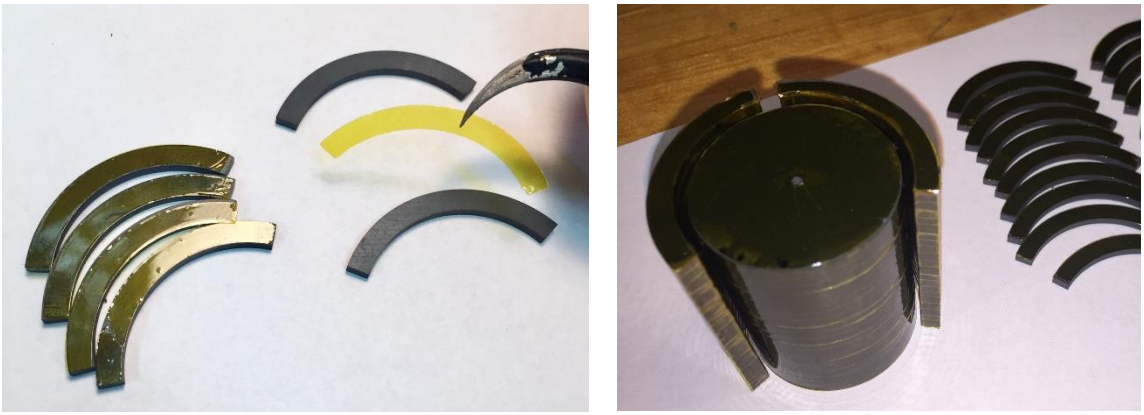

Figure 2-19: Assembly process of ferrite core inductor showing application of adhesive Kapton spacers (left) and completed center post and outer shell segments (right). In the righthand image, the third outer shell segment and end cap pieces are not shown.

A split winding strategy was used in order to avoid the risk of common mode current due to imbalance of the resonant tank element voltage drops on each side of the CPC and field winding as described in [33]. Two separate coils are wound onto the same ferrite core, in such a way that their inductances add in series with the coupler structure to achieve the desired resonant frequency. The coils were wound separately as shown in Figure 2-20 (a) as opposed to bifilar as shown in Figure 2-20(b), to reduce turn-to-turn voltage and proximity losses. In this way, the coil turns with the highest voltage potential between them are placed at far opposite ends of the core stack. The coils were wound using #18AWG silver plated copper wire, in order to improve high frequency AC conductivity. The wire was insulated with PTFE insulation, for high breakdown voltage, in order to withstand the high voltages encountered in a high kVA resonant tank application.

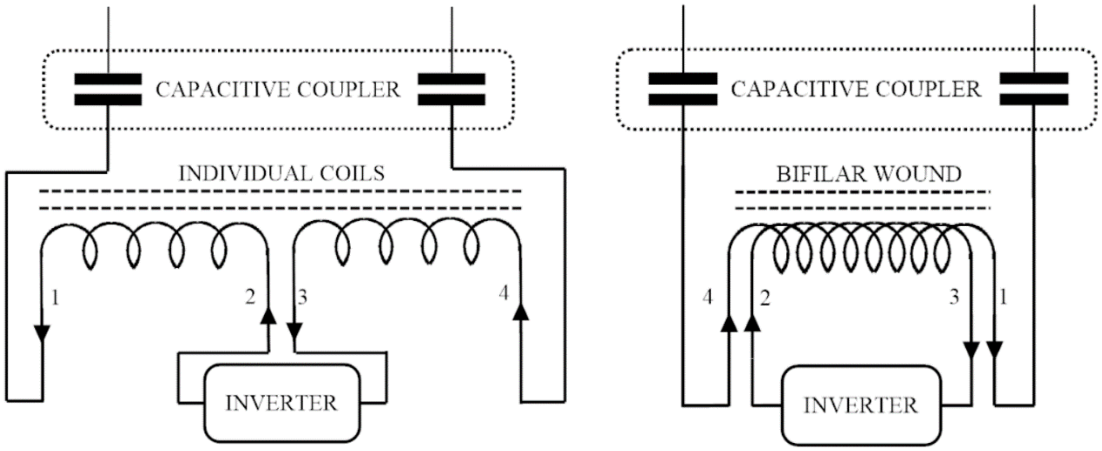

(a) (b)

Figure 2-20: Two different winding schemes for split resonant inductor on a single ferrite core.

A plastic inductor holder, including locations for banana plug connection terminals was 3D printed on a PLA printer and is shown in Figure 2-21(a). Connections between winding coils and banana plugs were made inside the base of the fixture, which were then covered by a phenolic bottom plate. Figure 2-21(b) shows a comparison between the original air inductors, and the equivalent valued ferrite core inductor. As shown, the cored inductor is many times smaller than the equivalent air inductors while also having far less stray field, which would allow it to be installed inside a small enclosure without introducing eddy current loss and electromagnetic interactions with surrounding electronics.

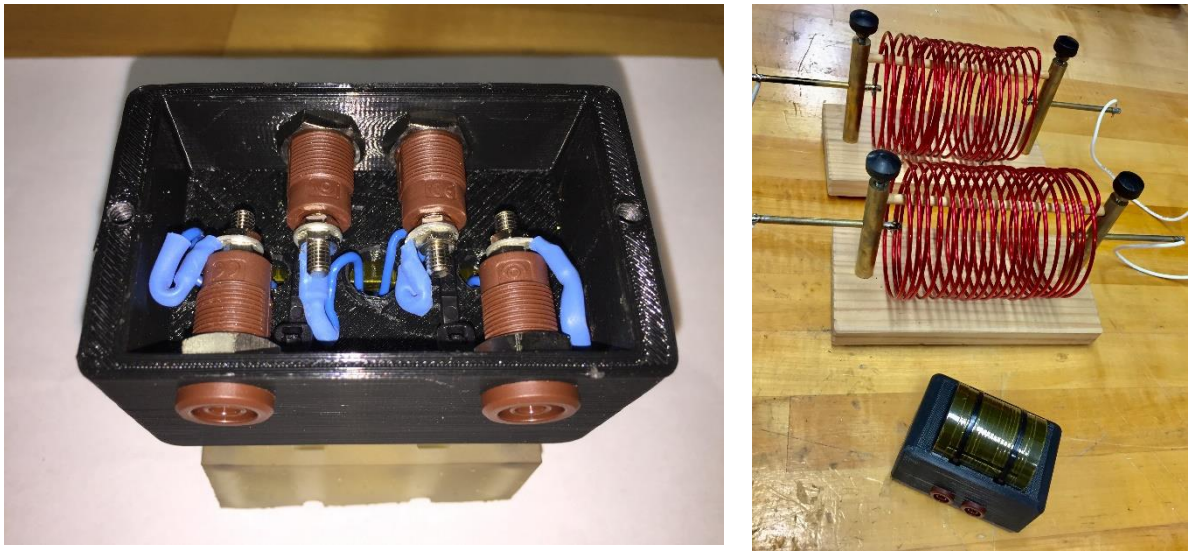

(a) (b)

Figure 2-21: Cored resonant inductor mounted in 3-d printed fixture. Connection of coil windings to terminals (a) and size comparison with equal value air inductors (b).

Impedance testing of the complete resonant tank circuit with both air inductors, and ferrite core inductors tuned to resonant at the same frequency with the same coupler PC boards are shown in Figure 2-22. As shown, the ESR of the tank circuit with the core inductors is actually significantly lower than with the air inductors. Although the air inductors do not have core losses, they do require a great deal more length of wire in order to achieve the same inductance value. Thus, the ac conduction and proximity losses cause the air inductors to suffer from higher ESR than the cored part. The resulting split-inductor had an inductance value and ESR of 27μH and 400mΩ per section (54μH and 800mΩ for the series combination) at the operating frequency of the CPT system.

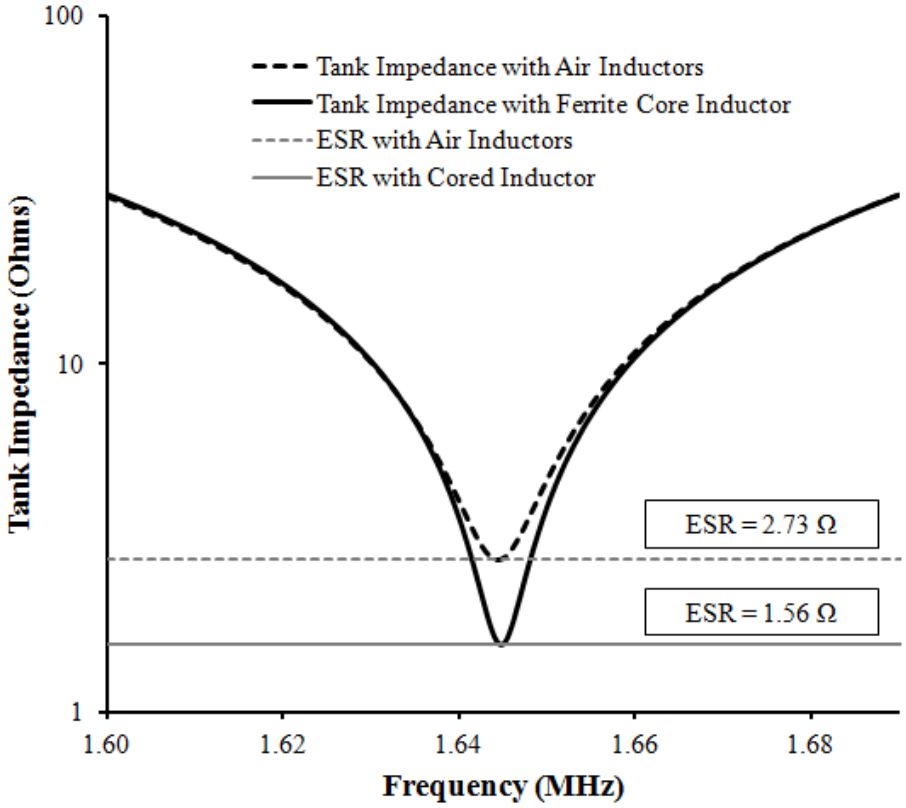

Figure 2-22: Impedance comparison between tank circuit using air inductors vs cored inductor showing reduction of ESR with cored inductor.

By comparing Figure 2-12 and Figure 2-22, it is seen that by implementing the PCB design changes suggested by FEA earlier in the chapter, as well as a carefully designed and constructed high quality factor ferrite core inductor described here, the overall ESR of the resonant tank has been reduced by about 75% from the original 3-phase air core tank circuit (ESR = 6.6 Ω) to the final single phase ferrite core tank circuit (ESR = 1.56 Ω). This drastic reduction in ESR of the tuned circuit, including both the capacitor coupler structure, and the resonant tank inductors, is responsible for the high efficiency and high power transfer capability which this system demonstrates.

Chapter 3 CPC System Power Electronics and Controls

Now that the design process for the electrode portion of the capacitive power coupler, and the resonant tank inductor, the design for the associated power electronics and controls will be discussed. In the first section of this chapter, the high-frequency inverter and it's associated controls will be described. The second section will describe the power electronics located on the rotating coupler board.

A Gallium Nitride (GaN) inverter originally designed in [62] was used for conversion of DC from a regulated benchtop power supply to the high frequency AC required for capacitive power coupling experimentation. At the MHz frequencies used for capacitive power transfer work, soft switching of inverter switches and rectifier diodes is necessary in order to ensure high efficiency. For this reason, a resonant inverter topology was chosen. By connecting the cored inductors, whose design was discussed in the previous chapter, in series with the capacitance formed by the printed circuit board electrodes, a resonant tank circuit is formed which if operated near resonance boosts the voltages applied across the coupling capacitors, taking better advantage of their rather small ~300 pF capacitances, as well as ensuring soft switching of the power electronics, so long as the system is operated near the resonant frequency of the tank circuit that is formed.

The schematic of the entire system is shown in Figure 3-1. Each major portion of the circuit will be discussed in more detail in the following sections.

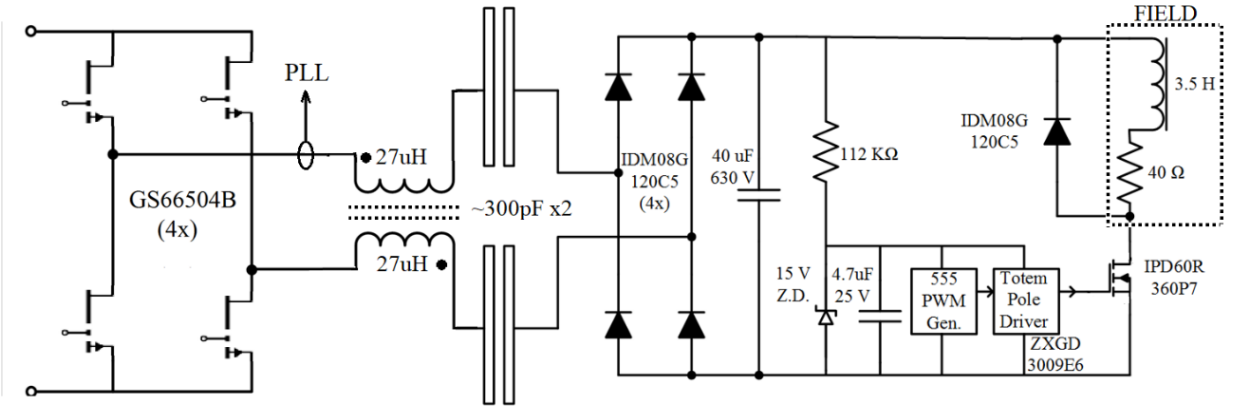

Figure 3-1: Overall CPT system schematic from DC input (left) to field winding load (right, dashed box).

The design of the GaN inverter, shown at left in Figure 3-1 is discussed in [62]. The design of the coupling capacitor assembly and resonant inductors, shown left of center in the schematic, was described in detail in the previous chapter. The following sections will describe the controls and electronics used to regulate frequency and gating of the GaN inverter, as well as the rotor electronics shown on the righthand side of the schematic.

3.1 PLL-based High Frequency Inverter Gate Control

It is desirable to operate the GaN inverter close to the resonant frequency of the combination of the resonant inductors and coupling capacitors. By doing so, power factor is brought close to unity, resulting in near zero current switching of the inverter transistors and rotor rectifier diodes. At this frequency, the capacitive reactance of the ~300pF coupling capacitors is canceled by the inductive reactance of the tank inductors, causing the capacitive coupling tank circuit to have a much lower impedance.

If tank inductance and capacitance were constant under all operating conditions, the GaN inverter could be connected to a simple fixed frequency gate drive, set at the measured resonant frequency of the CPC tank circuit which is approximately:

$$f_{resonant} = \frac{1}{2\pi\sqrt{LC}}. \tag{3.1}$$

In practice, environmental conditions and imperfections in flatness of the coupling boards cause slight saliency of coupling capacitance as the machine is operated and the shaft is rotated. This saliency of capacitance causes a mild modulation of the tank resonant frequency during rotation, requiring that the inverter frequency be actively adjusted to keep the circuit as close to resonance as possible. A simple solution to maintaining the proper phase relationship between inverter output voltage and current is to use a phase locked loop (PLL) circuit implement with analog ICs. AN analog solution is ideal for MHz frequency power electronics as commercial PICs or DSPs do not possess the necessary bandwidth.

The phase of inverter output voltage is directly tied to the switching of the GaN transistors, and thus to the output of the voltage controlled oscillator (VCO) which is feeding gating signals to the GaN inverter. The VCO provides the GaN inverter gate drivers with a complementary (180° out of phase) pair of 50% duty ratio square waves. The phase of the inverter output current can be measured using a simple current sensing transformer.

The current sensing transformer was constructed based on information from [73] by winding turns of magnet wire onto a powdered iron toroid, just large enough for the current carrying conductor to pass through. It is best to use a small toroidal core, with an inner diameter, once wound, that is

just large enough for the conductor under measurement to pass through. This minimizes leakage inductance of the current transformer which would cause phase and magnitude error in the output current. A 1:*N* turns ratio transformer is formed, where *N* is the number of turns wound on the toroid. For this work, 25 turns were wound onto the secondary. The transformer core and secondary are electrostatically "Faraday-shielded" from the current carrying conductor by a copper tube to prevent capacitive coupling of voltage from the conductor under test to the secondary winding. The whole assembly is then mounted to a circular copper frame which includes a BNC output connector, as shown in Figure 3-2. The frame and faraday shield are grounded via the BNC connector, which forms the ground reference for the output signal.

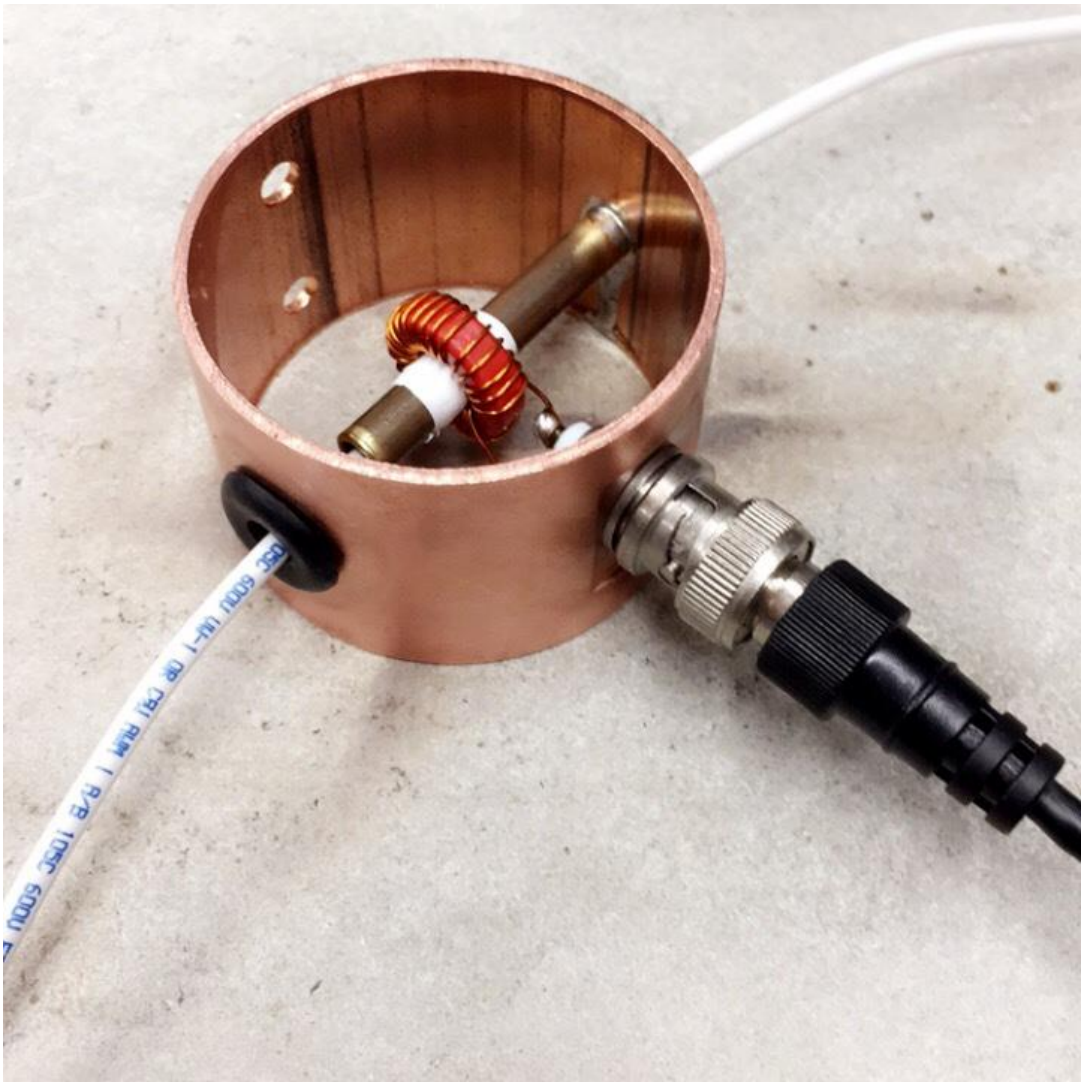

Figure 3-2: Current sensing transformer of simple construction used for closed loop frequency control for soft switching.

When connected to the 50 ohm load resistor in the PLL circuit, in parallel with the 50 ohm input on an oscilloscope used to monitor current, this 25 turn sensing transformer conveniently develops almost exactly 1 volt/amp across the 25 ohm parallel combination, as displayed on the oscilloscope.

At the input of the PLL circuit, this voltage signal developed across the input resistor is fed to a comparator integrated circuit, type AD8561. By comparing the alternating input signal to a zero volt reference (signal ground), a 50% duty ratio square wave is developed at the output of the AD8561 comparator, whose rising and falling edges correspond approximately to the zero crossing points of the sinusoidal inverter output current.

The square pulses from the current zero crossing detector are then fed through an RC-RC-RC passive integrator circuit, shown in Figure 3-3, forming a triangle wave. Component values for the passive filter were selected to give a good quality linear triangle wave with sufficiently large amplitude swing at the target frequency of operation, around 1.7MHz.

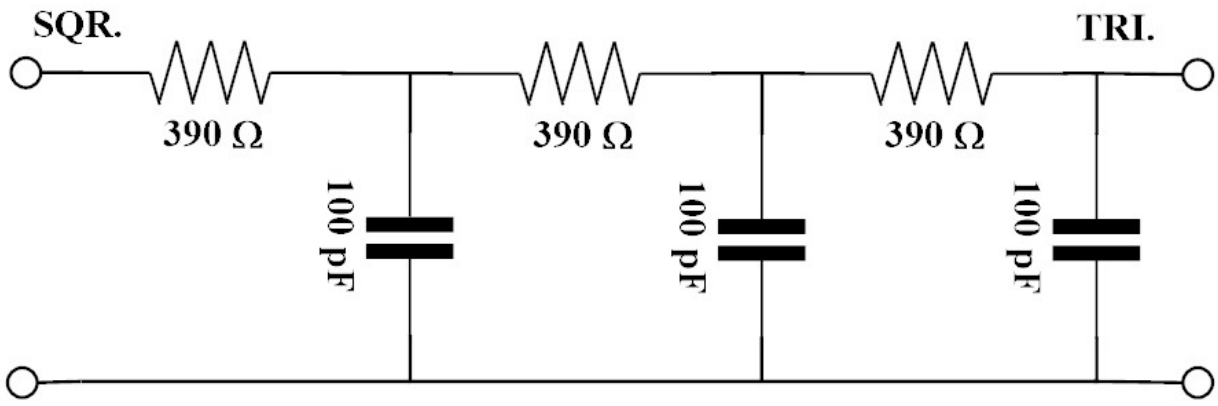

Figure 3-3: Passive RC-RC-RC integrator which converts square pulses from first integrator to ramps/triangles for phase adjustment using second integrator.

This triangle wave output from the passive integrator is fed into one input of a second AD8561 comparator. The second (reference) input of this comparator is connected to a variable DC voltage source. The phase relationship between the outputs of the first and second comparators can then be continuously adjusted by varying the DC reference voltage input to the second comparator. The setting of the DC reference voltage determines how “far up” the triangle wave ramp the signal will proceed before the comparator is triggered; thus resulting in an adjustable phase delay between the incoming and outgoing signal.

The control circuit is shown diagrammatically in Figure 3-4. The phase comparator and VCO shown at the lower left corner of are contained within a single integrated circuit, a CMOS version of the ubiquitous 4046 PLL.

The active loop filter utilizes a simple first order RC low pass filter buffered by an OPA2227 operational amplifier wired as a voltage follower or buffer. The selection of loop filter characteristics for this application is not very critical, due to the large disparity between the operating frequency of the inverter (~2MHz) and the maximum expected modulation frequency, which is tied to the maximum rotational speed of the CPC (~100Hz). The resistance and capacitance selected for use in the loop filter were 12kΩ and 330pF. The cutoff frequency of this filter is given by

$$f_{cutoff} = \frac{1}{2\pi RC} = \frac{1}{2\pi(12\text{k}\Omega)(330\text{pF})} = 40.2\text{kHz}. \quad (3.2)$$

The cutoff frequency of ~40kHz, being orders of magnitude greater than the expected modulation frequency, while also orders of magnitude below the VCO output frequency, ensures stable operation of the phase locked loop.

The output of the active low pass filter is diode clamped to a pair of adjustable DC voltage sources which limit the upper and lower frequency limits at which the VCO can operate, in order to ensure the system always self-starts, and to protect the GaN inverter from operating at excessive frequencies in the case of a fault in the current phase measurement circuit.

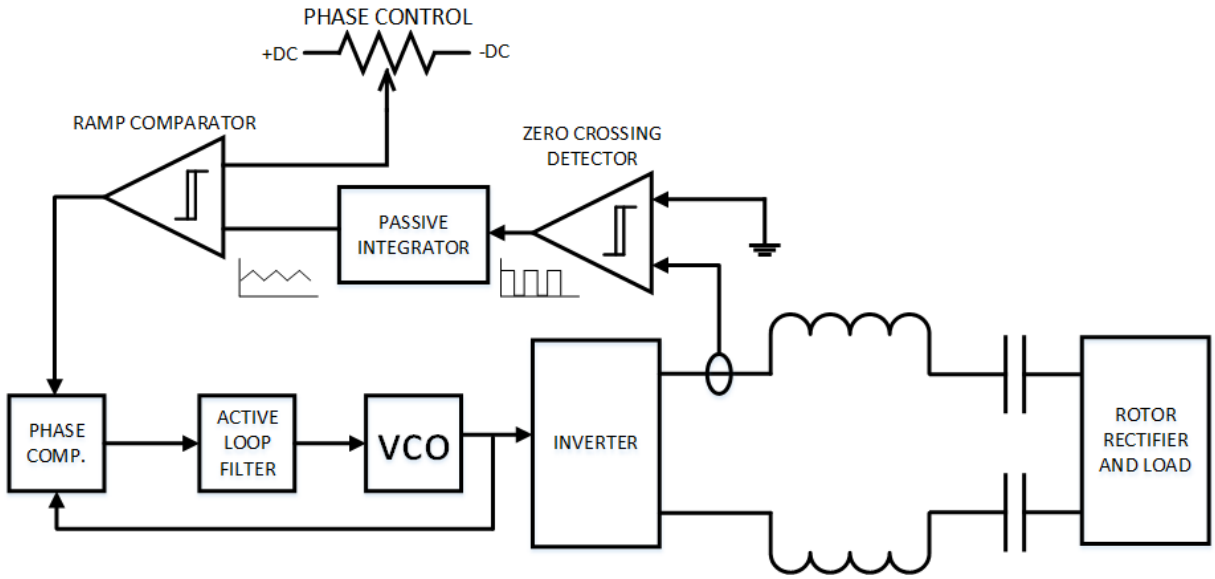

Figure 3-4: PLL-based automatic frequency control diagram.

Using this setup, the phase relationship between inverter output voltage and current, as adjusted using the variable DC reference voltage, can be regulated, thus ensuring soft switching over a range of tank resonant frequencies. The complete schematic for the PLL controller is shown in Appendix A.

3.2 Rotor-Mounted Power Electronics

As discussed in previous chapters, current is the primary bottleneck of a capacitive power transfer system, due to the limitations on electric field in the coupler gap. For this reason, it is favorable to operate CPT with a high impedance load. WFSM field windings inherently have a lower impedance (based on wire gauge sizes) than what is desired for CPT.

Evidence for the benefit of higher load impedance can be seen directly by comparing efficiencies from experimental data taken using an earlier PCB CPC prototype which did not include a rotor

mounted buck converter. The two data points are taken at the same input power with the only variation being two different load impedances, 38.5 ohms and 92 ohms. Even at power levels as low as ~100 watts, efficiency differences as large as 10% can be seen, as shown in Table 3.

TABLE 3. EFFICIENCY COMPARISON AT SAME INPUT POWER FOR TWO DIFFERENT LOAD RESISTANCES

Load Resistance	**Input Power**	**Output Power**	**Efficiency**
38.5 Ω	112 w	91 w	81 %
92 Ω	111 w	101 w	91 %

Impedance of WFSM rotor field windings can only be made so high before mechanical integrity of the rotor windings is compromised by the use of an excessively small wire gauge size. In order to make a CPC system useful across a wide range of WFSM applications, it must be able to function with a range of load impedances, some of which are much lower than the characteristic impedance of the capacitive coupler. This suggests the need for some sort of impedance matching, or transformation, between the CPC and the WFSM field winding.

By including one additional active switching transistor, a basic fixed-duty-ratio gate controller located on the CPC rotor board, and one additional diode, a fixed duty ratio buck converter can be implemented which would take care of this impedance matching requirement.

Without greatly increasing the semiconductor count, and without requiring any control signal path between the rotor and the stator, this simple open-loop dc-dc converter would allow CPC systems

which have high characteristic impedance to power a lower impedance field winding. The duty ratio D_{buck} would be selected to achieve the desired impedance transformation as follows.

$$Z_{out} = (D_{\text{buck}})^2 \, Z_{in} \tag{3.3}$$

In order to transform the ~40 Ω rotor winding resistance to the ~90 Ω that allowed >90% efficiency to be achieved in prior prototype couplers, as shown in TABLE 3, a duty ratio of ~ $^2/_3$ was selected for this work.

The schematic of the rotor power electronics including high frequency silicon carbide rectifier diodes and buck converter are shown in Figure 3-5.

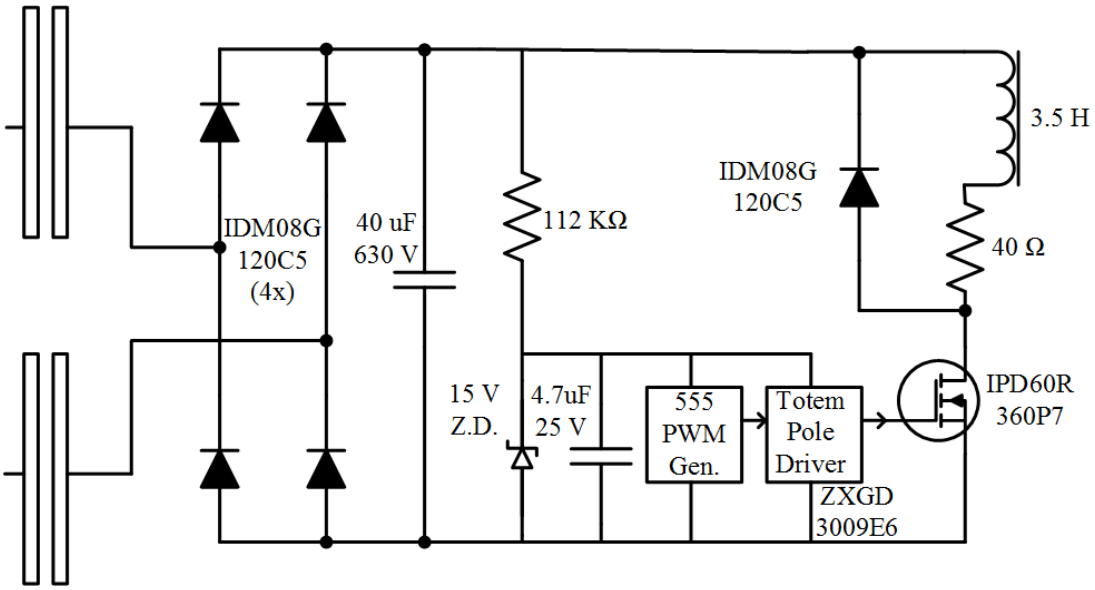

Figure 3-5: Schematic of rotor-mounted power electronics, including high frequency rectifier and buck converter.

A simple analog gate control is used to switch the buck converter MOSFET. The control consists of a 555 timer IC which, alongside associated passive components, is used to set the frequency and duty ratio. The output of the 555 drives the MOSFET through a totem pole style gate drive IC. Power for the gate drive and control is derived from the high voltage output of the rectifier using a dropping resistor and Zener diode. Very little power (on the order of microwatts) is required for the gate drive circuitry, due to the use of MOS components, thus the power dissipated in the dropping resistor and Zener diode is negligible. Because a fixed impedance ratio is desired, the buck converter duty ratio and frequency can remain constant, allowing for fully open-loop operation of the buck converter.

Without the presence of a buck converter, earlier CPC prototypes required very little filter capacitance at the output of the rotor rectifier bridge, due to the high frequency at which the CPC tank circuit operates. With the buck converter in mind, the filter capacitance present on the rotor board will need to be sized to keep voltage ripple at the input to the buck converter within reasonable limits. The value of capacitance will depend on the choice of buck converter switching frequency.

It is desirable to use the field winding inductance as the output filter for the buck converter, thus avoiding the need for a discrete inductor to be added to the rotor circuit board. Impedance of the WFSM field winding is shown in Figure 3-6. As seen, the field winding measures as an inductor out to approximately 2000 Hz, at which point its self-capacitance begins to dominate. In order to use the field winding as the buck output inductor, a buck converter operating frequency of approximately 1700 Hz was selected.

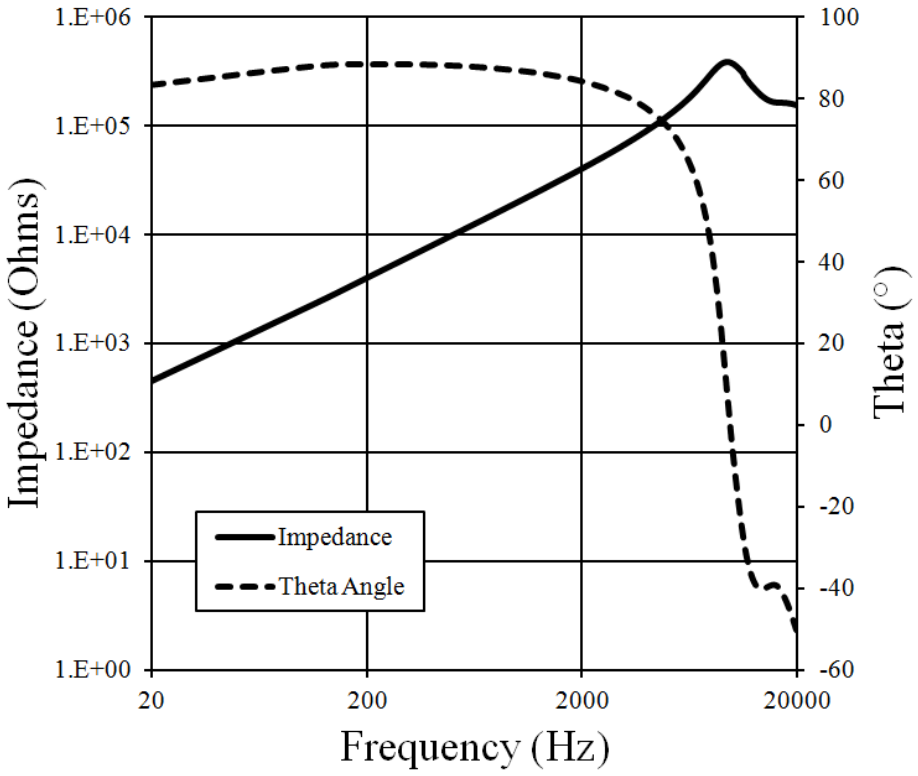

Figure 3-6: Impedance Z-theta plot of WFSM field winding.

Based on the buck converter switching frequency of 1700Hz and $D_{\text{buck}} = 2/3$, along with the 4.0 Amp target load current, the calculation of rotor filter capacitor value is as follows. For simplicity of calculation, ideal switches are assumed. Average buck converter input current at rated load is

$$I_{\text{in,average}} = D_{\text{buck}}\, I_{\text{out}} = \frac{2}{3}(4.0\text{A}) = 2.7\text{A}. \tag{3.4}$$

Voltage ripple on the filter capacitance would be reflected as load ripple to the CPC system, which would slightly modulate the resonant frequency of the CPC tank circuit. Thus, the PLL controlling the CPC inverter must be able to track this variation in order to maintain soft switching. Because the PLL bandwidth of ~40kHz greatly exceeds the selected buck converter switching frequency of 1700Hz, some amount of voltage ripple on the filter capacitance is acceptable. It was decided to allow approximately 10% ripple for this design.

During the "On" state of the buck converter MOSFET, the 4.0 Amp load current is being sourced by the combination of the CPC rectifier and the filter capacitance. The average current input to the rectifier is 2.7A as calculated above. The capacitor has to source the remaining 1.3A. Although the nominal rotor resistance value is 40 Ω, as shown in the schematic of Figure 3-5, the value measured with the rotor winding warm, during power testing, was 42.2 Ω. This value will be used in these calculations for better accuracy. Average capacitor (buck converter input) voltage can be calculated using Ohm's law and D_{buck}.

$$V_{\text{load}} = I_{\text{load}} R_{\text{load}} = (4.0\text{A})(42.2\Omega) = 169\text{V} \;\rightarrow\; V_{\text{in}} = \frac{169\text{V}}{2/3} = 250\text{V}_{\text{ave}} \qquad (3.5)$$

The capacitor value needed to maintain 10% ripple can then be calculated as follows.

$$C = i\frac{\Delta t}{\Delta V} = (1.3\text{A})\frac{2/3\left(\frac{1}{1700\text{ Hz}}\right)}{10\%(250\text{V})} = 20.4\mu\text{F} \qquad (3.6)$$

The capacitors which would be used on the rotor board were 630V rated X7R type ceramic chip capacitors. According to [74], X7R capacitors voltage coefficient of capacitance would likely result in a derating of at least 40% capacitance value when operated at 250VDC. For this reason, it was decided to use 40uF total filter capacitance in the final design, as shown in the schematic of Figure 3-5.

The entirety of the high frequency rectifier and buck converter were located on the same printed circuit board as the capacitive coupling electrodes, requiring only surface mount electronic components, resulting in a compact and efficient capacitive power coupler installation. Photos of the assembled rotor board will be shown with the experimental results in the next chapter. The overall schematic of the rotor electronics is shown in Appendix B.

Chapter 4 Experimental Results from Demonstrator System

4.1 Assembly of PCB CPC Prototype

A prototype of the printed circuit board capacitive power coupler was designed and manufactured by a printed circuit board house. The prototype contained the coupling electrodes, high frequency rectifier, and buck converter as outlined previously. Design rules determined using finite element analysis were followed, including slotting between electrodes, and the use of a 2-layer board construction to avoid overlapping traces. Photos of both sides of the printed circuit boards, as received from the board manufacturer are shown in Figure 4-1.

Figure 4-1: Printed circuit board coupler rotor, as received from the printed circuit board manufacturer. High frequency rectifier side (left) and close-up of rotor buck converter section (right).

Necessary components were obtained, and the rotor board was populated forming the completed unit. Close up photos of the populated electronics section of the rotor board, located around the inner shaft hole, are shown in Figure 4-2, prior to the application of any sort of board potting material.

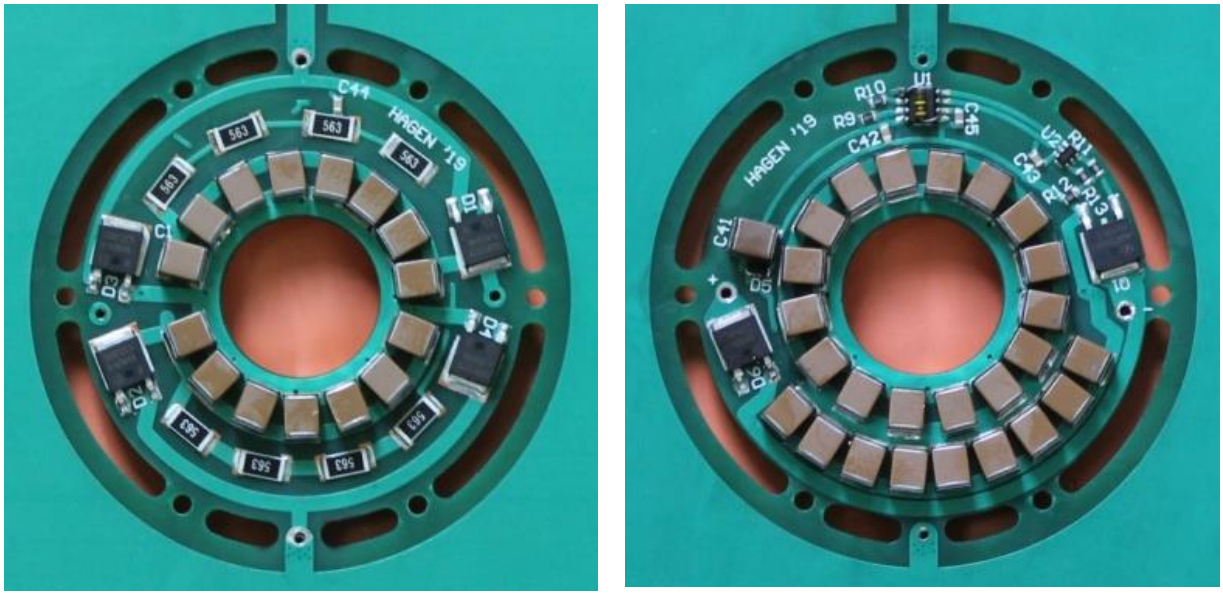

Figure 4-2: Printed circuit board coupler rotor, with electronic components populated.

Because the rotor board would be expected to spin at several thousand RPM's, there was a hazard of solder joint failure due to centrifugal forces acting on the surface mount components used. The decision was made to "pot" or encapsulate the entire electronic circuit on each side of the rotor board in a hard epoxy resin material, in order to mechanically hold the components in place at high rates of speed. A clear epoxy was selected in order that the components would remain visible after encapsulation. The electronics section of the printed circuit board coupler rotor, after encapsulation can be seen in Figure 4-3.

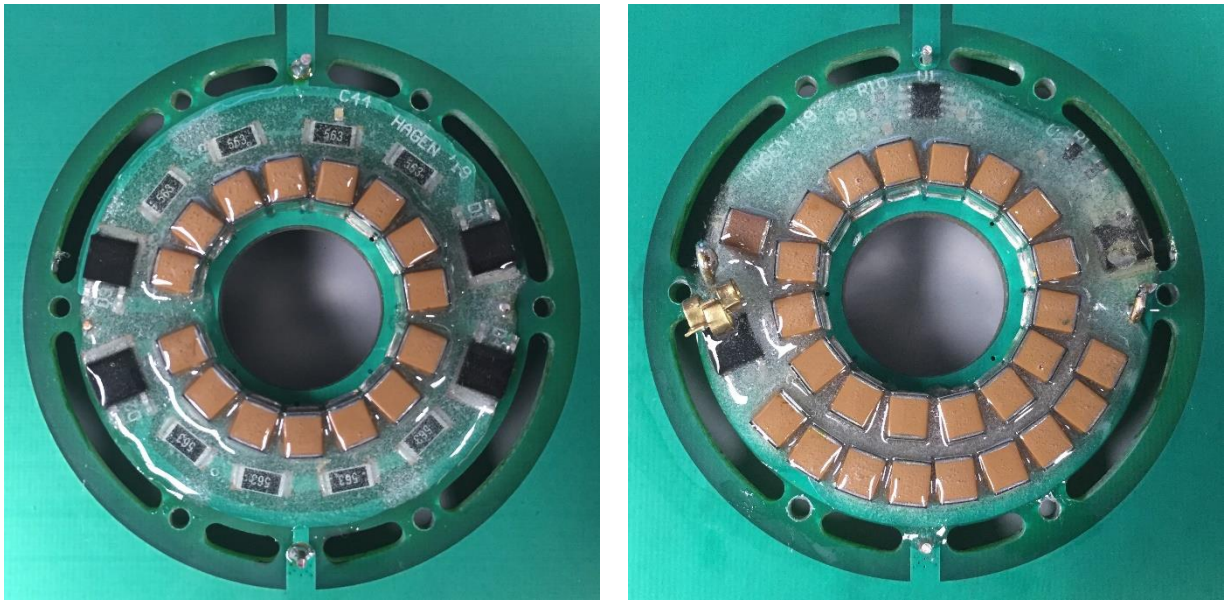

Figure 4-3: Epoxy encapsulated rotor power electronics.

4.2 Installation on Wound Field Synchronous Machine

During all experimental testing of the PCB capacitive coupler, it was mounted on a wound field synchronous machine that is representative of the coupler's intended application. The machine is designed for 30kW continuous, 55kW peak, with a base speed of 4000rpm [62]. The rotor board is mounted to the WFSM shaft using an aluminum hub which is press fit onto the shaft stub extending from the non-drive end of the machine. Though the coupler is sized to fit inside the machine, it was left on the exterior for this experimental work, for ease of connecting probes and monitoring component temperature in the lab.

The stator disks are mounted to the end plate of the WFSM housing using standoffs which allow adjustment of the axial position of the disks, thus allowing the rotor disk to be centered axially between the two stator disks. Connections are made between the rotor disk and the field winding

using wires which pass through a bore in the machine shaft; while connections between stator disks and resonant inductors are made using solder pads on the outer faces of the stator disks. A photo of the complete CPC assembly mounted on the end of the WFSM is shown in Figure 4-4.

Figure 4-4: CPC assembly mounted on WFSM end bell.

The phase locked loop control circuit discussed in the previous chapter was constructed and installed in an enclosure with the GaN inverter. The enclosure provided necessary power supplies, cooling fans, and electrical shielding for the system. The current transducer and resonant inductors were connected in series between the GaN inverter and CPC. The entire benchtop experimental setup is shown in Figure 4-5.

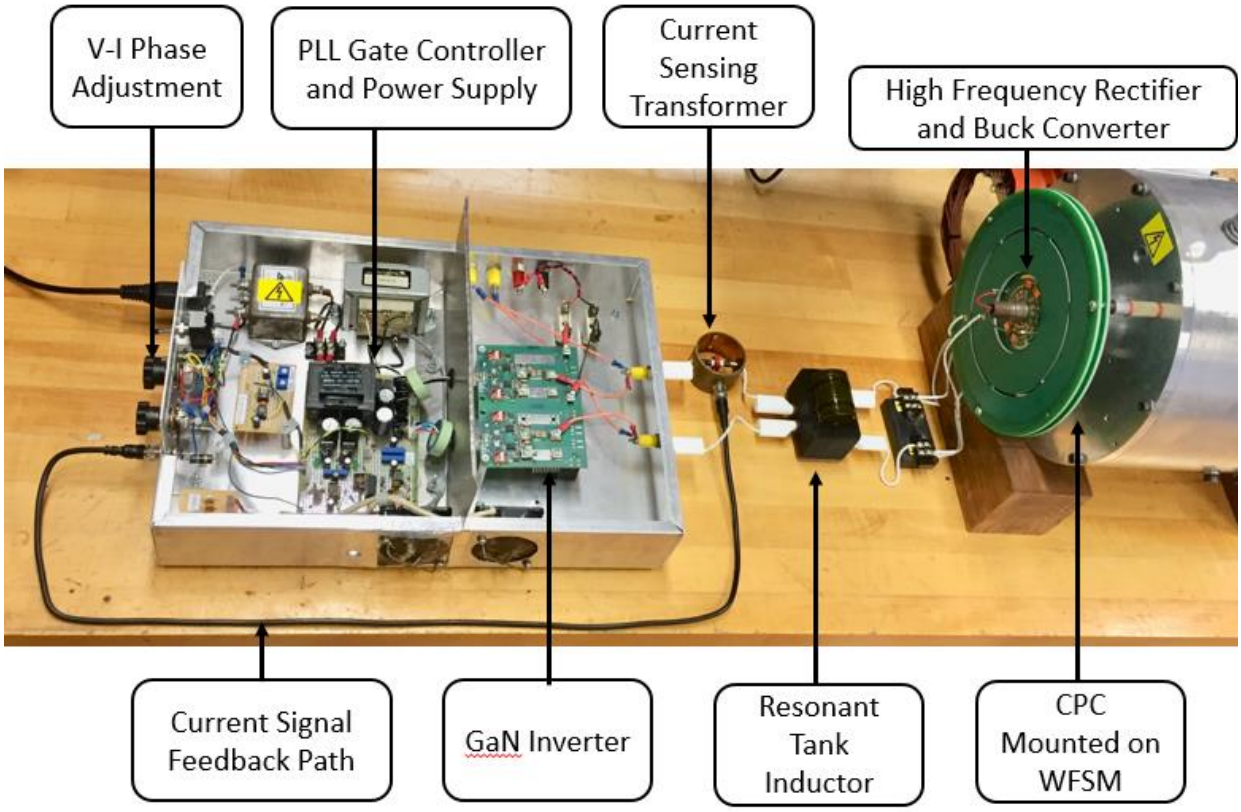

Figure 4-5: Bench top CPC test setup. Enclosure is shown with top cover removed.

Not shown is the DC bus supply for the GaN inverter which consists of a regulated DC benchtop power supply. One oscilloscope with a fast time-base was used to monitor inverter output voltage and current, as well as rectifier input voltage. A second oscilloscope with a slower time-base was used to monitor DC voltage and current input to the GaN inverter, as well as DC output voltage and current from the rotor buck converter to the load. Because the machine was not rotated during these initial benchtop tests, direct probe connections could be made to the rotor buck converter output. By measuring voltage and current at the input and output of the overall system, an accurate DC-DC efficiency calculation could be made.

4.3 Benchtop Testing

Using the setup shown, a set of bench top tests were performed up to a maximum of 676 watts output power (corresponding to 4.0 amps output current to the field winding, the target operating point based on the WFSM design.)

Results for these power tests are shown in Table 4.

TABLE 4. BENCH POWER TESTING OF PCB CPC MOUNTED ON WFSM

$V_{in,dc}$	$I_{in,dc}$	$V_{out,dc}$	$I_{out,dc}$	P_{in}	P_{out}	Eff	$I_{ac,rms}$	$V_{L,rms}$
(volts)	*(amps)*	*(volts)*	*(amps)*	*(watts)*	*(watts)*	*(%)*	*(amps)*	*(volts)*
108.27	1.03	65.27	1.53	111.52	99.86	89.55	1.614	465
152.06	1.47	88.84	2.26	223.53	200.78	89.82	2.346	676
189.59	1.76	110.01	2.74	333.68	301.43	90.33	3.090	890
219.41	2.02	126.98	3.15	443.21	399.99	90.25	2.869	826
247.80	2.24	142.55	3.51	555.07	500.35	90.14	3.436	989
269.54	2.48	159.57	3.77	668.46	601.58	89.99	3.680	1060
282.42	2.65	168.89	4.00	748.41	675.56	90.27	3.974	1144

As seen in the bottom row of the table, the target I_f = 4.0 A was met, showing that this capacitive coupler system is capable of fully exciting the wound field synchronous machine for which it was designed, without the need for additional laminations or windings within the machine. Regulation of this current, if desired, can be achieved via burst mode current control from the stationary side

as shown in [32], [39], [75]. Efficiency greater than 90%, measured dc input to dc output, was achieved. Inductor voltage in the final column was calculated based on AC current and measured inductance, as a direct measurement using oscilloscope probes would disrupt the tuned tank circuit. Because capacitive reactance is equal and opposite to inductive reactance in a tank circuit operating at resonance, RMS capacitor voltage across the CPC electrodes would be equal to the calculated inductor voltages in the right hand column. At the maximum power operating point, the capacitor voltage would then be approximately 1144 V_{rms}, or approximately 1617 V_{peak}. As discussed earlier, the breakdown voltage of the CPC is expected to be:

$$V_{c,breakdown} = E_{breakdown} \cdot g = \frac{3000\ \text{V}}{\text{mm}}\ 0.8\text{mm} = 2400\ \text{V}. \qquad (4.1)$$

By taking the ratio of (1617 V / 2400 V) we see that at maximum rated power, delivering 4A into the WFSM field winding, the coupler capacitors were operating at 67% of their theoretical breakdown voltage. Though this is greater than the 50% safety factor given in an earlier example to illustrate a typical design process, this is still within safe limits and electrical breakdown was not an issue during experimental testing.

Plots of voltage waveforms at the output of the GaN inverter and input to the SiC high frequency rectifier, as well as resonant tank current, can be seen in Figure 4-6 for the 676 watt test.

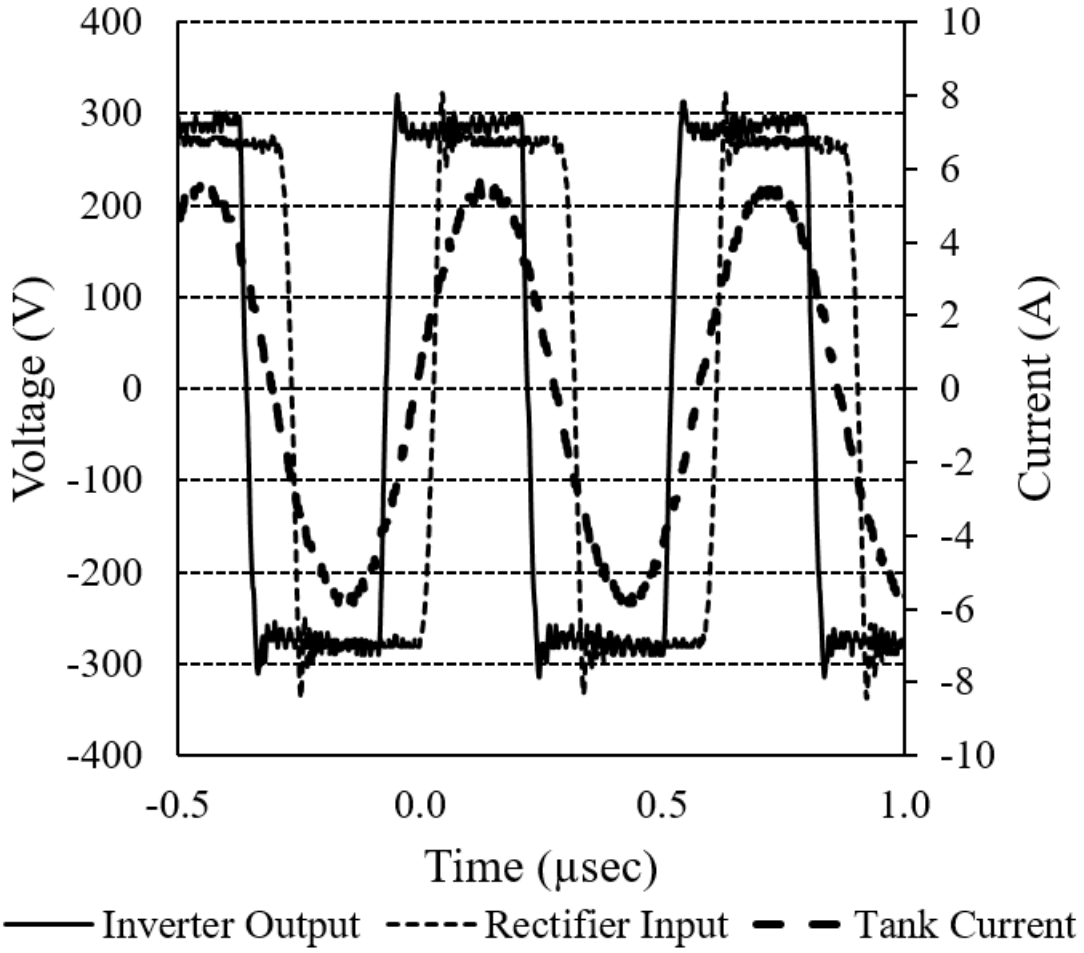

Figure 4-6: Plots of inverter output voltage, tank current, and rectifier input voltage for the CPC system operating at 676w output.

As seen in these plots, the zero crossings of both voltage waveforms occur close in phase to the zero crossings of the tank current, resulting in the best possible switching condition for both the GaN inverter and the high frequency rotor rectifier in the constructed configuration.

The current waveform slightly leads the voltage input to the rectifier, due to the parasitic capacitive nature of the rectifier diodes. The diode bridge rectifier capacitance prevents the system resonance

from being the same as the coupling tank. In order to compensate for this and provide the best compromise towards soft switching of both the rectifier diodes *and* the GaN inverter, the PLL phase regulator is set such that the GaN inverter sees a slightly inductive load. In this operating condition, as seen in Figure 4-6, neither the inverter output or the rectifier input have perfect unity power factor, however they are both to place the current and voltage zero crossings as close as possible for all semiconductors.

4.3.1 DC Input and Output Waveforms

Plots of Input and output DC voltage and current waveforms can be seen in Figure 4-7 and Figure 4-8, respectively. Input DC measurements are taken at the output of the regulated DC power supply used to feed the DC bus of the CPC system. Output measurements are taken at the connection point between the CPC rotor board and the WFSM field winding itself.

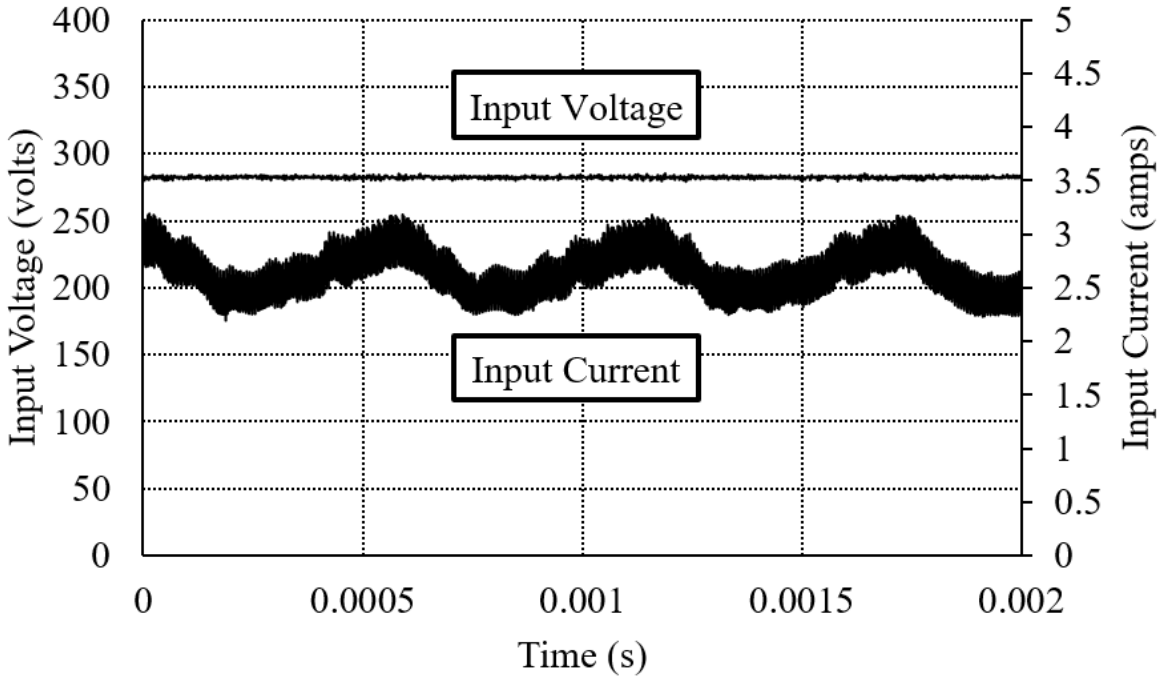

Figure 4-7: Input measurements to high frequency inverter from regulated DC power supply. Upper trace shows voltage (approximately 282 volts), and lower trace shows current (approximately 2.6 amps)

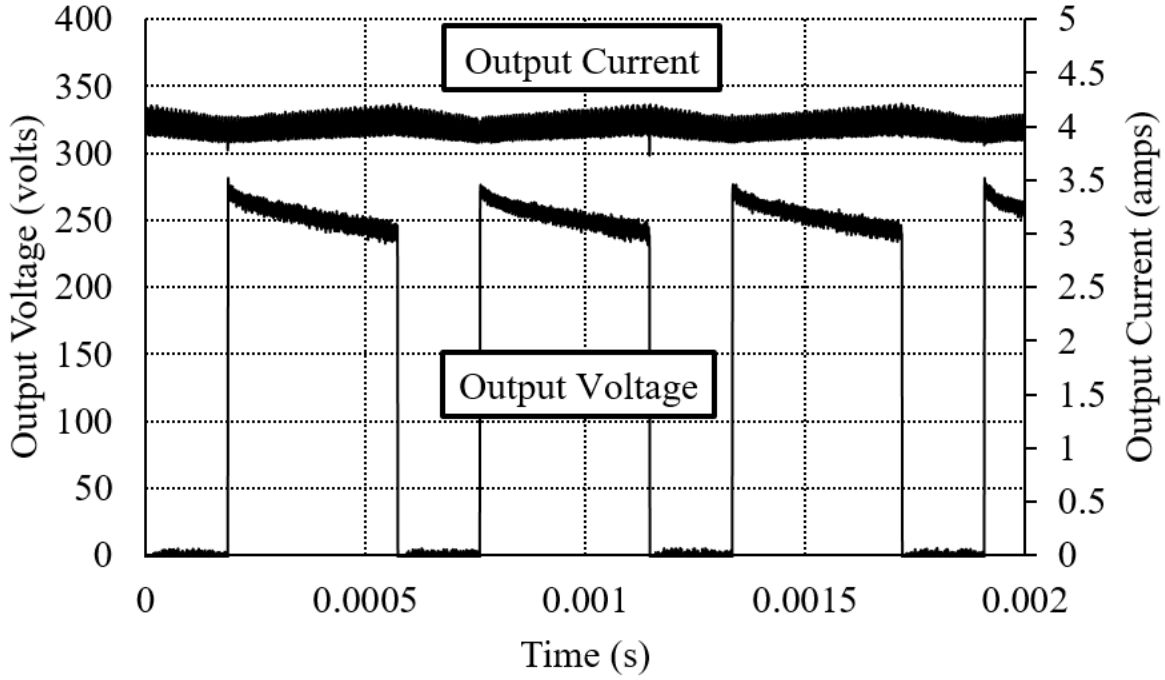

Figure 4-8: Output measurements from buck converter to field winding. Upper trace shows current (4 amps), and lower trace shows voltage (averaging 169 volts dc).

The average values of these direct current waveforms were used for system efficiency measurements, and are the values given in Table 4. However, as seen in plots, AC components of these waveforms at the buck converter switching frequency are also present. We will show that these components of the rotor field winding current create a pathway for use of the CPC system in rotor position tracking in future iterations of a CPC system.

4.3.2 Rotor-Injected Position Tracking Signals Measured at WFSM Stator Terminals

During testing of the capacitive power coupler, mounted on the WFSM, the WFSM stator was instrumented with voltage probes, so that the three phase BEMF could be seen. During benchtop

testing, when the machine was not being rotated, the three phase fundamental back-EMF was zero. However, as shown in Figure 4-9, a balanced three phase set of voltages were present, corresponding to the switching action of the rotor mounted buck converter.

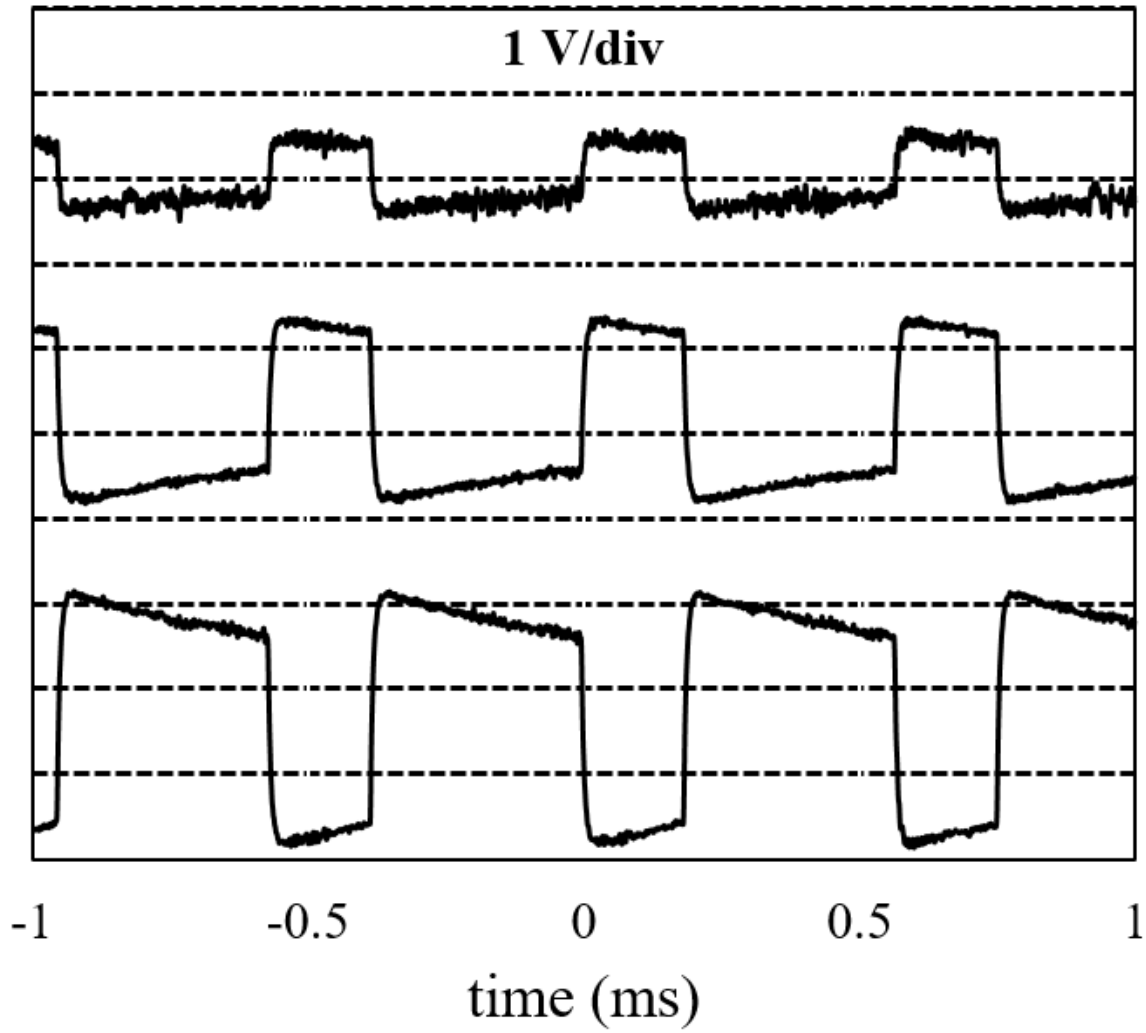

Figure 4-9: Voltage corresponding to buck converter switching is present on three phase stator output from WFSM, providing resolver functionality.

The three phase voltages form a balanced set, i.e. they sum to zero. Their relative magnitudes correspond directly with the electrical position of the rotor, showing that these signals could be used directly to eliminate the need for a resolver or encoder for dynamic control of the WFSM in certain systems.

In an actual implementation, phase current sensors would already be present in a high performance WFSM drive. These current sensors could be used to detect the current ripple that would be transformer-coupled from the rotor to the stator due to this action of the buck converter; thus eliminating the need for a resolver and paving the way for true sensorless operation of the WFSM.

4.3.3 PLL Control Voltage for Position Tracking

As described in Chapter 3, the PLL system relies on a voltage-controlled oscillator, which in this case utilizes an analog control signal V_{control}. This control signal directly corresponds to the frequency, f_{VCO}, at which the oscillator must be operated in order to achieve tank resonance, by some constant of proportionality, k, determined by the VCO circuit. Given knowledge of the tank inductance, L, (which can be assumed to be constant), this frequency control signal can be used to directly calculate coupler capacitance, C, at any given time during operation based on the following relationships:

$$f_{\text{VCO}} = k\, V_{\text{control}} \tag{4.2}$$

$$2\,\pi f_{\text{VCO}} = \frac{1}{\sqrt{LC}} \tag{4.3}$$

$$\sqrt{LC} = \frac{1}{2\pi f_{\text{VCO}}} \rightarrow C = \frac{1}{L(2\pi f_{\text{VCO}})^2} \rightarrow C = \frac{1}{L(2\pi k V_{\text{control}})^2} \tag{4.4}$$

If capacitance is designed to stay relatively constant throughout rotation, the control voltage required to keep the system at resonance would also be fairly constant. However, if the CPC electrodes were intentionally shaped in a way that resulted in predictable capacitive saliency with rotation, knowledge of capacitance could be used to calculate rotor position.

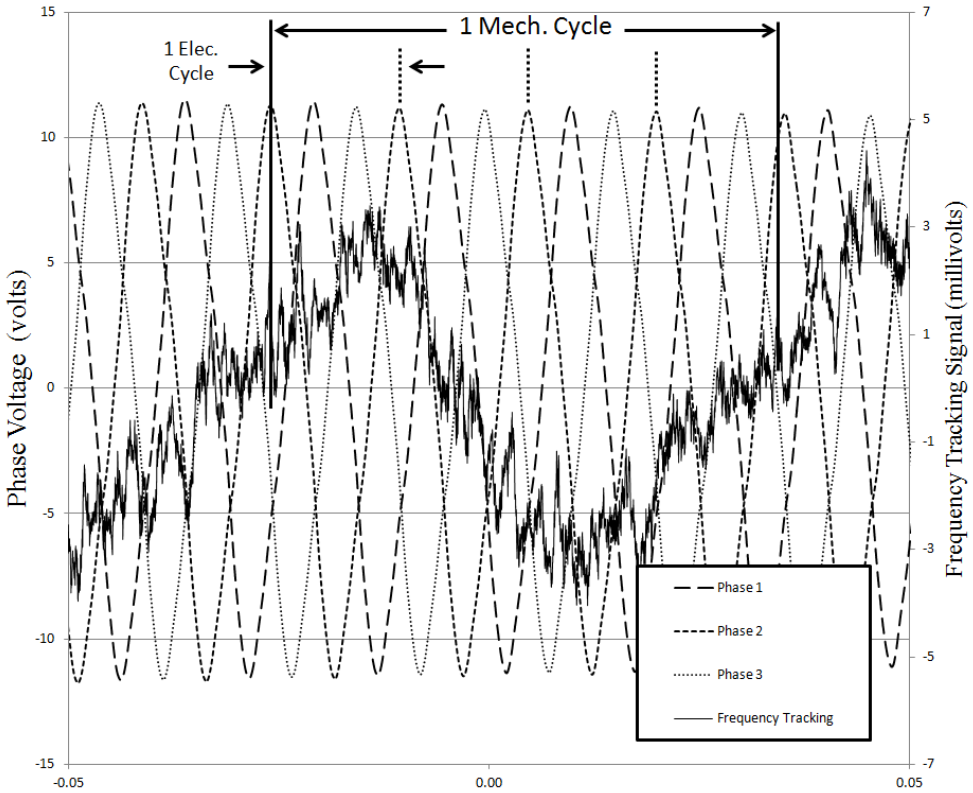

Figure 4-10: Shaft mechanical position tracking signal from PLL VCO superimposed on stator 3-phase BEMF at a slow rotational speed. Because of the machine pole count, 1 mechanical cycle corresponds to 4 electrical cycles.

A plot of VCO control voltage along with three phase back-EMF voltages from the stator of the WFSM is shown in Figure 4-10. In the case of the current capacitive coupler, the electrodes are designed such that capacitance remains essentially constant throughout rotation. Even still, variation of several millivolts is seen, due to slight flatness distortion of the PCB's.

This frequency control signal, by itself, is not sufficient to determine the absolute position and direction of the rotor, since it is only a single periodic signal which changes at the mechanical frequency of the machine. However, if the proper drive homing procedure is used at startup, and the initial direction is known from the inverter drive, then the signal could be used to measure position from that point forward. This PLL control voltage in combination with the three phase current ripple measurement due to rotor side injection via the buck converter, as described in the previous section, would likely be able to determine absolute rotor position.

4.4 Dynamometer Testing

After confirming the CPC system's capability to transfer full rated field power for the WFSM rotor, the WFSM was mounted on a dynamometer test cell to perform testing at high speed. A photograph of the experimental setup is shown in Figure 4-11. The prime mover is a 170kW induction machine (top left in photo), and the WFSM (center) is connected as a generator to a fan-cooled resistive load bank (not shown in photo).

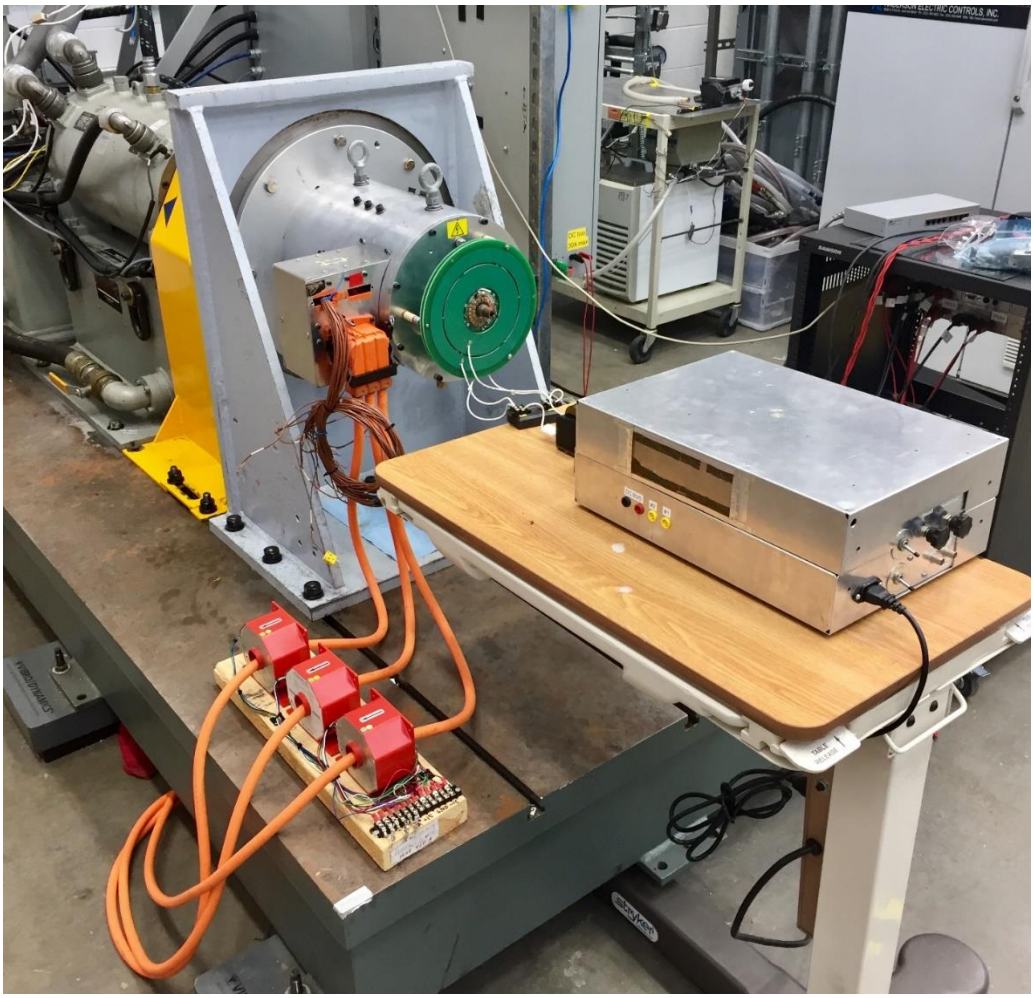

Figure 4-11: Dynamometer test setup for WFSM with CPC excitation.

The CPC control electronics are located in the rectangular aluminum enclosure at right, and stator current sensors are located at the bottom left. During testing, all three phase voltages and currents were measured using an oscilloscope with power analyzer capability, in order to determine output power being generated into the resistive load bank. A schematic showing the connection between WFSM stator and resistive load bank, with measurement points labelled, is shown in Figure 4-12. An oscilloscope with power analyzer functionality was used to display the three currents and three line-to-line voltages. The power analyzer function was then used to display rms power, as will be plotted in the experimental data. The parameters of the WFSM under test [62] are given in Table 5.

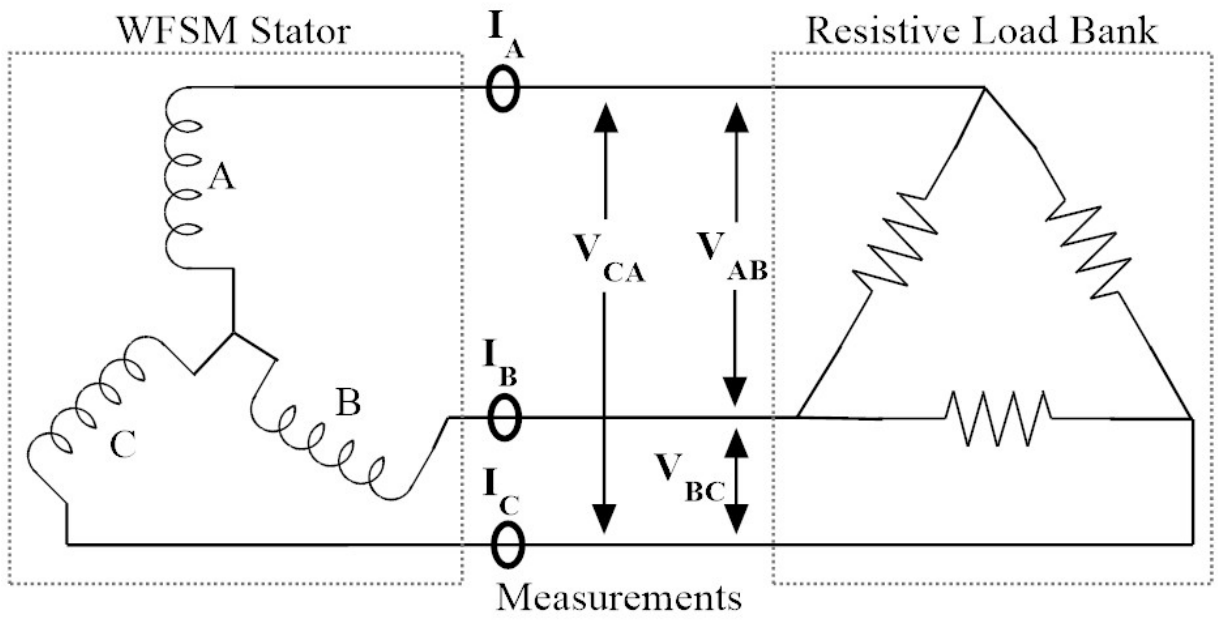

Figure 4-12: Connection between WFSM stator and resistive load. Measurement points shown.

TABLE 5. PARAMETERS OF WOUND FIELD MACHINE UNDER TEST [62]

Parameters∗	FEMM	MagNet	Experimental
L_f [mH]	2330	2386	2278
L_d [mH]	0.969	0.998	0.98
L_q [mH]	0.565	0.597	0.60
L_m [mH]	32.36	32.94	33.46
R_f [Ω]	26.952	26.952	26.5
R_s [Ω]	0.0153	0.0153	0.02

∗ Unsaturated inductance values and resistances at 20 °C.

Machine parameters	Experimental value
Peak motoring torque/Power∗	190.55 N·m / 79.6 kW ∗
Peak motoring efficiency/Torque	95% @ 87.5 N·m @ 4000 r/min
Mass∗∗	40.64 kg
Volume∗∗∗	11.06 L
Volumetric peak torque density∗∗∗	17.22 N . mL^{-1}
Specific peak torque density∗∗	4.69 N·m kg^{-1}
Volumetric peak power density∗∗∗	7.19 kWL^{-1}
Specific peak power density∗∗	1.95 $kWkg^{-1}$

∗Held for over 30 s; can hold essentially continuously.
∗∗Includes stator, rotor, and shaft mass (shaft is oversized).
∗∗∗Cilindrical volume of active materials plus ATF spray cooling rings.

Tests were performed at a variety of shaft speed and field current points, ranging up to the rated speed of the machine, 4000 rpm, and up to the target field current, 4.0 A. The resistive load bank was configured to such that the machine would be operated as a generator near it's 30kW continuous power rating when rated field current was supplied at rated speed.

Measured WFSM output power is plotted as a function of shaft speed at four different CPC tank current values in Figure 4-13.

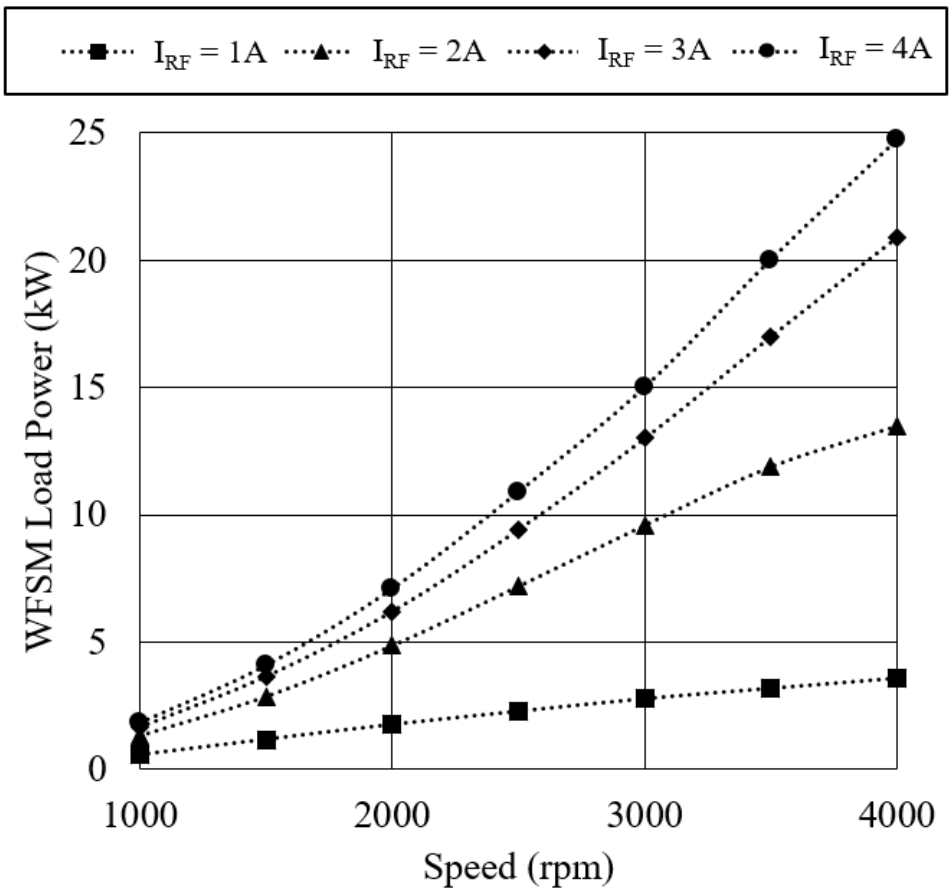

Figure 4-13: WFSM load power as a function of shaft speed at various CPC tank currents (dc field currents).

At the load resistance utilized for this testing, rated speed with 4A field current resulted in 24.7kW power generation, as shown in the plot. Stator line-to-line voltage is plotted as a function of CPC tank current at seven different shaft speeds in Figure 4-14. It should be noted that this machine derives some of its torque from reluctance, and without the aid of closed loop control facilitated by a drive, peak power of 55kW is not feasible. Nevertheless, the excitation system achieved the performance necessary for use in the intended vehicle drive application.

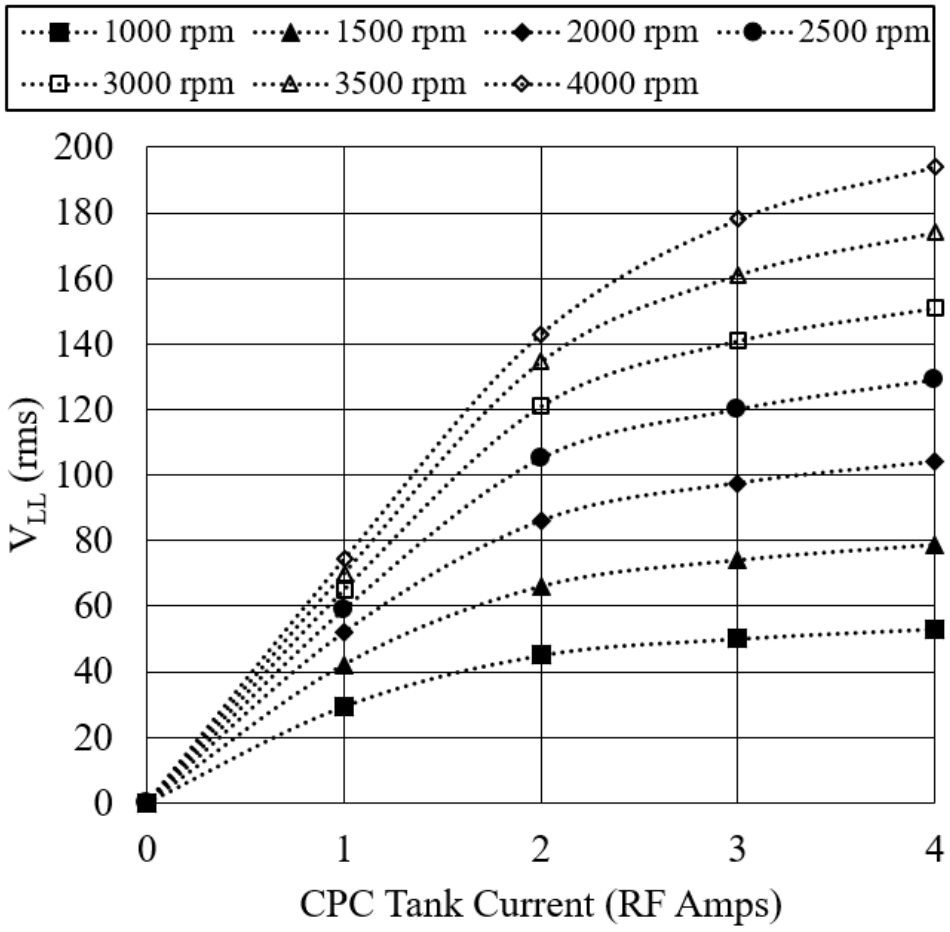

Figure 4-14: Line to line stator terminal voltage (resistive load bank) as a function of RF tank current (dc field current) at various operating speeds.

At higher field currents (approaching 3-4amps), the output voltage begins to plateau due to machine saturation.

Because the CPC rotor board is spinning in these tests, direct measurement of DC field current was not possible. However, as seen in Table 4, rms RF tank current and DC buck converter output current are approximately equal at all operating points, as a result of the combination of buck converter duty ratio and the effects of parasitic capacitances on the power factor between RF tank current and rectifier input voltage (visible as a phase misalignment in Figure 4-6). Thus, the RF tank currents shown in Figure 4-13 and Figure 4-14 can be directly interpreted as being equal to DC field current, given the particular buck converter duty ratio selected. Based on the relationship between DC output current and rms RF tank current,

$$I_{\mathrm{DC}} = \frac{2\sqrt{2}}{\pi D_{\mathrm{buck}}} I_{\mathrm{RF,rms}} \cos\left(\Theta_{\mathrm{RF}}\right) \tag{4.5}$$

A power factor of approximately 0.75 at the rectifier input would explain the 1:1 ratio between RF tank current and DC field current seen experimentally, which agrees with the plots of Figure 4-6.

As a final test, the load resistance was reduced slightly from the value used while collecting the data for Figure 4-13 and Figure 4-14. At this load resistance, 30kW power was generated with 4A field current at 4000rpm, demonstrating full rated power of the WFSM, using only the printed circuit board capacitive power coupler for excitation of the rotating field winding. Scope captures of the three phase line-to-line voltages and currents output from the WFSM during the 30kW test are shown in Figure 4-15.

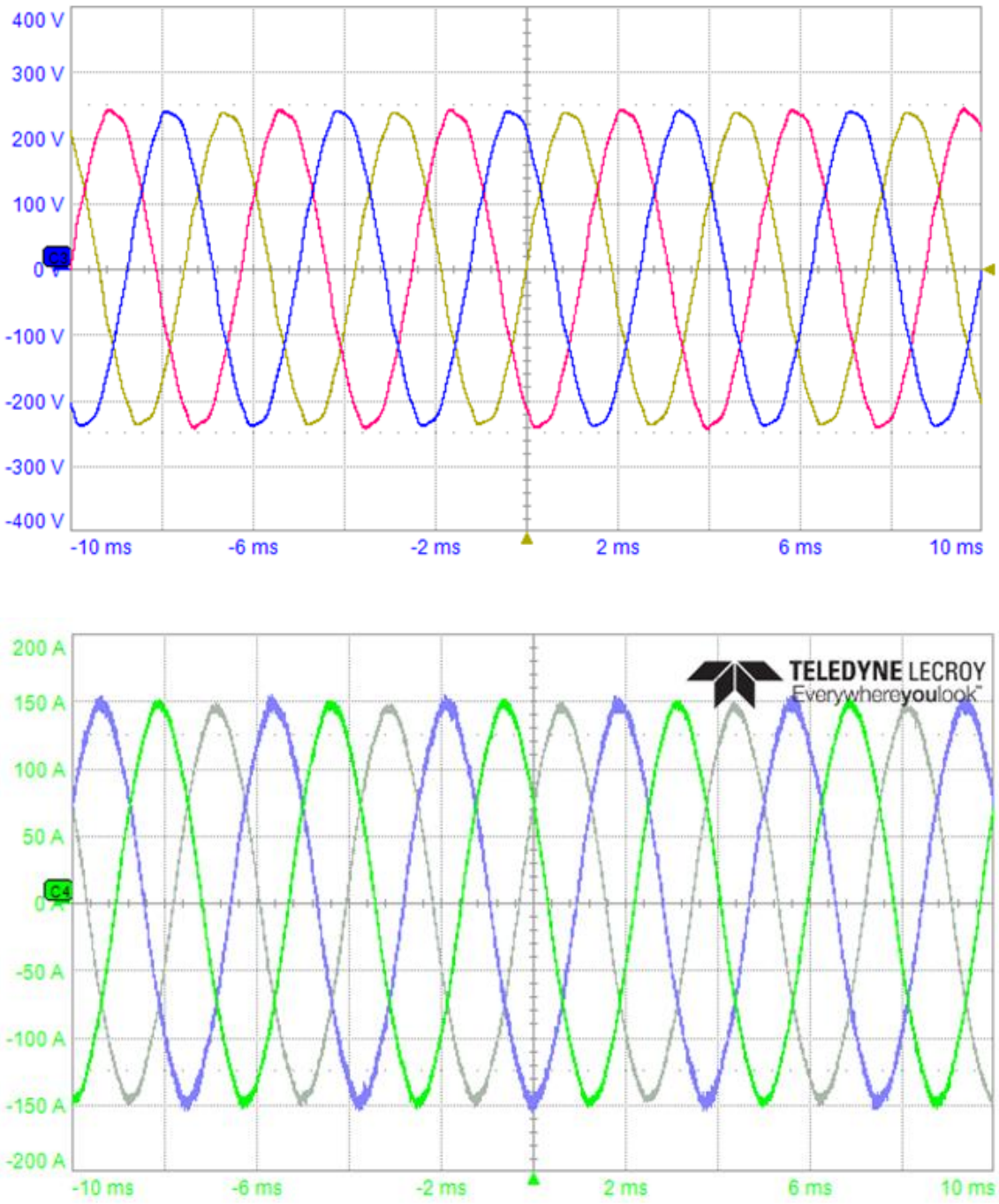

Figure 4-15: WFSM stator line-to-line voltage and current waveforms, while generating 30kW into resistive load.

4.5 Concluding Remarks on Experimental Testing

Extensive bench top and dynamometer testing has shown that the printed circuit board capacitive coupler system, including closed loop frequency control, ferrite core resonant tank inductor, and integrated rotor power converter, is in fact a compact and efficient solution for wound field synchronous machine excitation.

Even at MHz frequencies used, GaN HEMT's in the high frequency inverter did not show any notable heating, due to the soft switching behavior ensured by the phase locked loop frequency controller. This suggests that with proper tuning and frequency control, switching frequency could be pushed even higher in future implementations (i.e. into the 6.78MHz ISM band.)

Efficiency of the CPC system including the rotor-mounted buck converter was nearly identical to efficiency of earlier prototype systems which used higher load impedance without the buck converter for matching. This implies that the efficiency of the buck converter itself is very high. The low operating frequency of the buck converter (~1700Hz) in conjunction with the primarily inductive impedance of the field winding at that frequency (as visualized in Figure 3-6), lead to very efficient operation of the converter.

Although strides were taken to reduce dielectric losses from the earlier coupler printed circuit board prototypes to the final version of the coupler, this will be an ongoing opportunity for improvement in these systems, as dielectric losses show up throughout the system, not just on the coupler boards.

Figure 4-16 shows an example of dielectric heating appearing in a terminal block used for interconnections between the resonant tank inductors and the CPC capacitor electrodes. Bear in mind that the voltages (and therefore the electric fields developed) in this part of the circuit are very high compared to the dc bus voltage, due to the resonance of the tank.

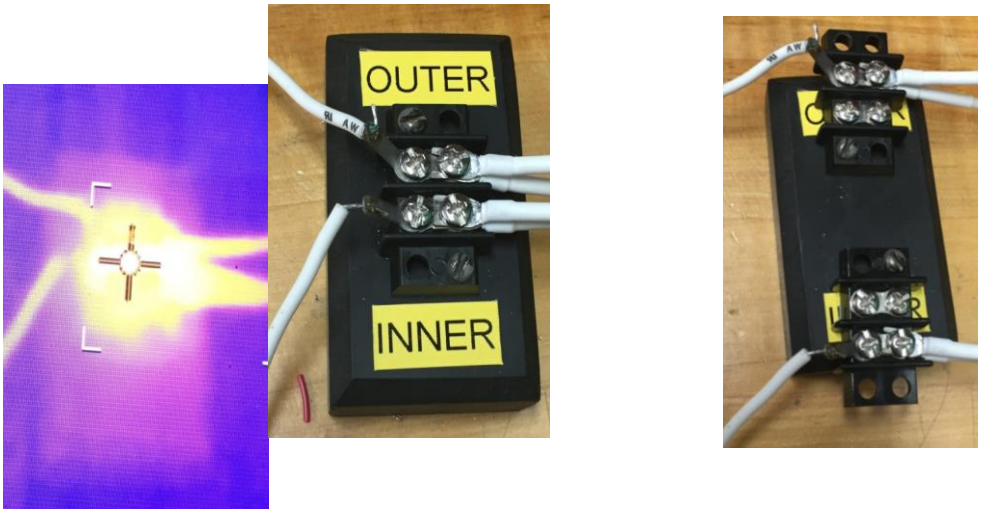

(a) (b)

Figure 4-16: Thermal image showing dielectric heating of terminal block insulator material between leads connecting resonant tank inductors to CPC (a), and corrective measure taken to separate them, eliminating the issue (b).

In this case, the issue showed up on a piece of hardware which was used for ease of connection during bench top testing in the lab. However, similar problems could be expected in a production setting, due to various types of off-the-shelf electrical connectors, terminal strips/blocks, or interconnecting cables, based on proximity of high frequency / high voltage conductors that are separated by lossy dielectric materials. Careful design must be carried out for every component of the system in order to ensure the best efficiency possible. Integration of the inductors as surface mount components in strategic locations on the CPC PCBs would be ideal in future iterations as the high tank voltages would be removed from cabling and connectors.

Chapter 5 Conclusion, Contributions, and Future Work

5.1 Conclusion

A brushless excitation system for a wound field synchronous machine has been designed and experimentally demonstrated to provide full field excitation to a 55kW WFSM, using only low cost printed circuit boards. Several loss mechanisms were investigated experimentally as well as through FEA simulation, and then design changes were made to mitigate the losses based on observations. The final result was a contactless rotational power coupling capable of transferring 675 watts power at an efficiency of >90%, providing full rated 4.0A to the field winding of the WFSM under test. This type of coupler can be scaled to larger power levels by increasing coupler area and/or operating frequency. A compact ferrite-core resonant inductor has been constructed, which proved to be an improvement over air core inductors (the current state of the art for CPT) in both compactness and electrical performance. Automatic frequency control was implemented using a phase locked loop which will allows the CPC system to operate at peak efficiency over a variety of conditions, without user intervention. A dc-dc buck converter was included on the same PCB as the integrated rectifier/coupler, which allows the relatively high characteristic impedance PCB CPC to be operated into lower impedance loads such as a typical WFSM field winding, with high efficiency. The PLL system, as well as the rotor mounted dc-dc converter both provide opportunities for position self-sensing without the need for an encoder or resolver.

5.2 Contributions

The following is a list of the main contributions described within this thesis, made in the area of capacitive power transfer and wound field synchronous machine excitation. A more detailed review of each will follow:

1. A WFSM brushless exciter was created which uses the same printed circuit boards as both the rotating rectifier and electric field power coupling structure.
2. A step by step design process was laid out as a guideline for engineering a printed circuit board capacitive power coupler for rotational applications.
3. FEA was used to investigate two coupler PCB design rules, which when implemented resulted in a 58% reduction in ESR of the coupler resonant tank circuit.
4. Multiple prototypes were designed, manufactured, tested, and improved upon, resulting in a kW-scale power coupler which exhibits required performance at high efficiency.
5. Automatic Frequency Control was implemented using a phase locked loop, which ensures maximum switching efficiency at high frequency.
6. A Buck type DC-DC converter was included in the rotor board power electronics for load impedance matching between the CPC and the field winding resistance.
7. A ferrite cored split-winding inductor was constructed which was approximately 10% the volume of equivalent-value air core tank inductors. Experimentally demonstrated 4.5kVAR, rms at 1.68MHz and resulted in measured 43% reduction in tank circuit ESR.
8. The framework for future implementation paths of two Methods for Sensorless Position Estimation were Experimentally Verified. Innate rotor side injection via the buck converter and saliency tracking of the CPC.

Contribution 1: *A WFSM Brushless Exciter using Only Printed Circuit Boards*

A capacitive power coupler was designed based solely on conventional low cost printed circuit manufacturing techniques for both mechanical and electrical functionality. The simplicity of this structure stands out when compared to other capacitive power coupler topologies which require precision machining of electrode surfaces, special coatings, or dielectric and lubricating fluids. The use of air as a dielectric eliminates the need for any kind of lubricating fluid, as there is no contact between rotor and stator components. Because of this, the lifespan of the coupling structure is theoretically only limited by the bearings of the electric machine on which it is mounted.

Because the air gap is on the order of 0.5 – 1 mm, there is no need for intricate fixtures or alignment procedures to mount the coupler boards to the machine rotor or stator. They can simply be affixed using conventional hardware to properly located mounts, much in the same way that the rest of the electric machine's components are assembled. Thus the use of a printed circuit board CPC does not have any significant impact on the complexity of assembling a WFSM, unlike many other types of exciters currently being used for the purpose.

The technology is scalable over a wide range of power levels and physical geometries, because of the versatility of PCB manufacturing. Coupler structures can be stacked/cascaded axially if needed, for high power high speed applications where large radius boards would not perform well mechanically. The use of well established printed circuit board manufacturing techniques and surface mount components make this type of brushless exciter well suited for low cost mass production, as would be required by the automotive and heavy equipment industry.

Contribution 2: *Step by Step PCB CPC Design Process*

As a second contribution, a clear step by step design process has been laid out for sizing and designing the geometry and electronics for a printed circuit board style capacitive power coupler. The process is summarized here:

- The maximum electric field that can exist between coupling capacitor plates is determined by the dielectrics between them.
- A minimum gap between rotor and stator plates is chosen based on flatness of the plates, and mechanical rigidity of the mounting.
- Based on the max electric field and capacitor gap, peak capacitor voltage can be calculated.
- Knowing voltage limitation and required current based on load, operating frequency and coupling coupling area must be chosen next.
    - The selection of frequency and area depend on a constraint hierarchy:
        - If frequency is the primary constraint (as limited by the power electronics and other components), coupling area must be increased to compensate (i.e. cascaded disks, larger coupling structures).
        - If space/compactness is the primary constraint, and frequency can be made higher (as is usually the case with modern GaN semiconductors), coupler area can be reduced to fit within the space constraint, with a corresponding increase in frequency.
- Once the total coupling capacitor area and operating frequency are selected, the inner and outer radii of each concentric ring shaped electrode must be calculated in order to achieve equal capacitance between them.

    - A simple approximation tool for fringe fields was presented, which proved accurate enough for this work.

- Once all electrode dimensions are known, printed circuit boards with those electrodes as copper traces are designed, including rotating rectifier and other power electronics as needed.
- If necessary for lower impedance loads (WFSM field) a rotor mounted buck converter is included, and its switching frequency and duty ratio selected based on the characteristics of the load (the degree of impedance mismatch between the load and the CPC resonant tank circuit).

Contribution 3: *FEA used to investigate PCB Design Rules for Loss Minimization*

Finite element analysis in Ansys Maxwell was performed to investigate the potential effects of two different PCB design strategies intended for reduction of dielectric losses. The first was the slotting/milling away of FR4 circuit board substrate material between adjacent CPC electrodes, leaving air, a lossless dielectric between. Early prototypes used inner layers of a 4-layer PCB to make connection between outer capacitor electrodes and rectifier components located near the inside diameter. The second design strategy was elimination of overlapping traces in a multi-layer board, and switching to a simple 2-layer board where connections to outer electrodes are brought through gaps in inner electrodes. Both Maxwell simulations showed 3-4x reduction in electric displacement field intensity in the region of interest on the board. When implemented experimentally, these changes resulted in a 58% reduction of ESR in the resonant tank circuit.

Contribution 4: *Multiple Prototypes Designed, Manufactured, and Tested*

Several prototypes (both three phase and single phase configurations) were manufactured by a PC board house and fully analyzed and tested in the lab. Problems and inefficiencies that were encountered with one prototype were used to make design changes and optimizations for the next prototype, until a final version which was able to supply the target 4.0A load current (~675w) at a more than acceptable efficiency >90% was realized. The development of the various prototypes is summarized in the photographs of Figure 5-1.

Prototype 1 Rotor

Prototype 2 Rotor

Prototype 3 Rotor

Final Prototype Rotor

Prototype 1 Stator

Prototype 2 Stator

Prototype 3 Stator

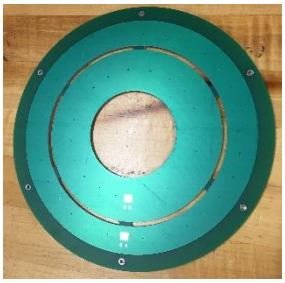

Final Prototype Stator

Figure 5-1: Photos to summarize development of printed circuit board capacitive power couplers, progressing left to right. Rotor boards (top row) and stator boards (bottom row) are shown for each of the prototypes manufactured.

Contribution 5: *Automatic Frequency Control using Phase Locked Loop*

It has been shown that peak system efficiency depends on soft switching of the high frequency inverter, in order to avoid switching losses in the GaN transistors. Additionally, the capacitive coupling interface is relatively high impedance when its reactance is not cancelled by an inductor, thereby limiting power throughput. Resonance, or operation near resonance, is a fundamental requirement. Up to this time, soft switching has been accomplished by manually tuning the resonant inductors and inverter frequency until approximately zero current switching is accomplished as seen on an oscilloscope.

In order to ensure soft switching of the GaN inverter transistors and rotating rectifier diodes, a phase locked loop circuit has been implemented for control of the GaN inverter switching frequency. Even as the values of resonant tank circuit components vary slightly, as in variation of coupling capacitance with rotation due to imperfect flatness of coupling PCB's, the PLL constantly adjusts operating frequency to remain at resonance. Using basic analog circuit design techniques, the PLL controller has been built in such a way as to avoid the need for expensive high-performance digital controllers which would be required to actively monitor and control the phase relationship between inverter output voltage and current at MHz frequencies.

Contribution 6: *Buck-type DC-DC Converter on Rotor for Impedance Matching*

A simple “low-side switch” buck converter circuit was added to the rotor rectifier/coupler board to allow the relatively low impedance 40 Ω rotor winding to appear as a higher impedance ~90 Ω to the output of the CPC high frequency rectifier. The rotor mounted buck converter only requires one additional diode and one MOSFET to be added to the rotor circuit. The control power for the MOSFET, which is only on the order of microwatts, is powered from the high voltage DC bus, thus making the converter fully self-sufficient. No communication is required between the rotating buck converter and the stationary CPC control electronics, as the buck converter is simply used as an open-loop fixed duty ratio “dc-dc transformer”. The present rotor field winding self-resonates due to parasitic capacitance at a fairly low frequency of around 2kHz, limiting the buck converter operating frequency. The inclusion of the buck converter between the high frequency rectifier and load did not result in any measurable reduction in system efficiency, suggesting high buck converter efficiency.

Contribution 7: *Ferrite Cored Resonant Tank Inductor*

A high quality factor ferrite core inductor was designed and constructed based on the general form factor of [72], but configured for kVAR operation in a resonant tank circuit. Overall dimensions of the inductor were increased over the [72] design using parametric ratios in order for wire with thicker high-voltage capable insulation to be used. Also, Kapton film was used to insulate ferrite core pieces from one another as well as from the windings, to prevent leakage current flowing as a result of the higher turn-to-turn voltages produced in a resonant tank inductor. These films also sized the air gap as shims. As shown in experimental results, this cored inductor actually performed better (lower ESR) than the equal valued air inductor. This can be attributed to the fact that the inclusion of a ferrite core allows the same inductance to be produced using fewer turns of wire, around a smaller form. Therefore, proximity losses are reduced, as well as ac conduction losses, due to the reduction in length of wire that is required and the management of fringe fields. The inductor, comprised of a split winding on a common core, was experimentally tested at 4Arms, 4.5kVARrms at 1.68MHz. The use of this inductor resulted in an additional 43% reduction in resonant tank ESR over the use of air inductors in an identical tank circuit. The combination of the effects of FEA-derived PCB design rules (Contribution 3) and the use of this ferrite core inductor resulted in an overall reduction in tank ESR from 6.6 Ω to 1.6 Ω, a 75% reduction.

Contribution 8: *Framework for Two Methods for Position/Speed Estimation Experimentally Demonstrated*

Rotor position and speed measurements are critical for the dynamic control of synchronous electric machines. Traditionally, this has been accomplished using digital encoders or analog resolvers mounted to the shaft of the machine. Encoders and resolvers add cost to the machine, as well as providing an additional failure point, as they do not hold up well in harsh environments often encountered by electric machines exposed to things like chemicals, extreme vibration, or moisture.

As discussed in Chapter 4, the PLL control voltage signal can be used to track saliency in coupler capacitance, due to the resulting shift in tank resonant frequency. A coupler electrode geometry which intentionally introduces a predictable capacitive saliency could be used to provide rotor position information based on measurement of the PLL control voltage.

Secondly, the presence of a low frequency buck converter on the rotor introduces a signal injection to the rotor field winding. This signal couples via transformer action to the three phase stator. The proportion of this coupled signal which appears on each of the three stator phases can be used to calculate rotor electrical position directly, thus using the WFSM as its own resolver for rotor electrical angle.

5.3 Future Work

*The following improvements could be made to further the ease of adopting the technology described in this paper for a wide variety of applications in industry**:***

1. Push operating frequency into the 6.78MHz ISM Band
2. Shrink overall size and thickness of PCB CPC assembly further
3. Utilize miniature off-the-shelf PCB-mount inductors for resonant tank
4. Optimize WFSM field winding for higher buck converter switching frequency
5. Use CPC enabled attributes to commutate the machine when configured as a motor drive and eliminate resolver or encoder.
6. Package the CPC and associated electronics within the WFSM.

Suggested improvements #2 and #3 should follow naturally from the transition to ISM frequencies described in #1, due to the fact that passive component values and sizes will shrink in size with an increase in frequency. A brief description of each improvement will follow:

Future Work 1: *Increase Operating Frequency to 6.78MHz ISM Band (priority objective)*

The ability to reduce resonant component values is an obvious advantage that would stem from raising operating frequency from ~1.7MHz as described in this paper, to the 6.78MHz ISM band. Issues of EMI would be less significant due to the fact that 6.78 MHz and its harmonic 13.56 MHz are specifically allocated by the FCC for such purposes as this, and therefore operation at these frequencies is allowed.

Additionally, by requiring smaller coupling capacitance, a 6.78 MHz system would allow for larger operating clearances between coupling disks, and smaller outer radii allowing these systems to be operated in higher speed, higher vibration systems.

Future Work 2: *Shrink Overall Size of PCB CPC Assembly (bonus)*

As mentioned above, increasing operating frequency into the 6.78 MHz ISM band would allow reduction in required coupling capacitance to achieve the same power transfer levels. By reducing required capacitance, CPC disk dimensions could be reduced. The disks could be made smaller in diameter to fit into more confined spaces on WFSM's (i.e. within the inner diameter of the winding oil spray nozzles on an oil spray cooled machine). Because the disk size would be smaller, flatness would be less of a concern, and thus much thinner printed circuit boards could be used than the ones described in this paper.

Future Work 3: *Utilize Miniature Off-the-Shelf PCB Mount Inductors (bonus)*

Not only would raising operating frequency shrink coupling capacitor size, but it would also reduce the size of the tank inductors. Inductors with an inductance value and VAR capability suitable for the current CPC system are not commercially available. This necessitated the adaptation of the [72] design for this work. However if frequency is increased into the 6.78 MHz ISM band, where resonant tank inductor value will only need to be in the integer microhenry range, it is likely that miniature off-the-shelf printed circuit board mount inductors could be used in the resonant tank, which would dramatically reduce system cost when compared to the custom made core pieces used in the inductor which was designed for use at the lower frequency of 1.68MHz in this paper.

Future Work 4: *Optimize Rotor Winding for Higher Buck Converter Switching Frequency*

A large proportion of the power electronics section around the inner diameter of the CPC rotor board is occupied by the filter capacitors required to store energy at the input of the buck converter. The sizing calculations for this filter capacitance is described in Chapter 3, and is scaled by the output current, switching frequency, and duty ratio of the buck converter.

The selection of buck converter operating frequency was based on the fact that the field winding of the current WFSM rotor begins to self resonate above 2000Hz. This is because it was wound with a high number of turns of fine wire, in order to better suit it for use with previous CPT work, prior to the introduction of the rotor-mounted buck converter.

Because of the impedance matching afforded by the rotor mounted buck converter, future implementations could utilize a more conventional lower resistance field winding, which would have a much higher self-resonant frequency. This would allow a higher buck converter operating frequency, therefore the size of the filter capacitances, and the CPC rotor board, could be further reduced.

Future Work 5: *Use CPC Attributes for Encoder/Resolver Functionality*

Two different methods of rotor position estimation were described in the experimental results and contributions of this thesis. During the experimental work, the WFSM was only tested as a generator, not as a motor drive. Future experimentation should demonstrate the use of CPC system attributes, including capacitive saliency tracking via PLL and rotor signal injection from the buck converter, to commutate the WFSM, while operating it as a motor with a variable speed drive, without the need for an encoder or resolver.

Future Work 6: *Package the CPC and Electronics within the WFSM*

The coupler prototypes described in this thesis were experimentally tested with the coupling boards mounted on the outside of the test WFSM for ease of measurements and adjustments. Though they were tested outside the WFSM, the coupler boards were in fact sized to fit within the test machine. Future work should include mounting the CPC within the WFSM housing. In addition to reducing the length of the overall machine by moving the CPC inside, the machine housing can be used to aid in EMI shielding; especially if the GaN inverter and resonant inductors can be moved onto the CPC stator PCB, within the WFSM housing. The goal should be a compact and low cost fully integrated PCB coupler, including rotor and stator side electronics, which can be installed within a WFSM in place of a bulky electromagnetic coupler. Increasing the operating frequency and reducing coupler and resonant inductor size, as described in Future Work 1 – Future Work 3, will aid in designing coupler systems small enough to fit within the WFSM housing.

Appendix

Appendix A – PLL Control

The following is a schematic of the entire PLL controller, which receives its input signal from the tank current sensing transformer and provides a complementary pair of 50% duty ratio signals to the gate drives of the GaN inverter. Close up schematics of the key sections will be shown after the overall schematic, for ease of readability.

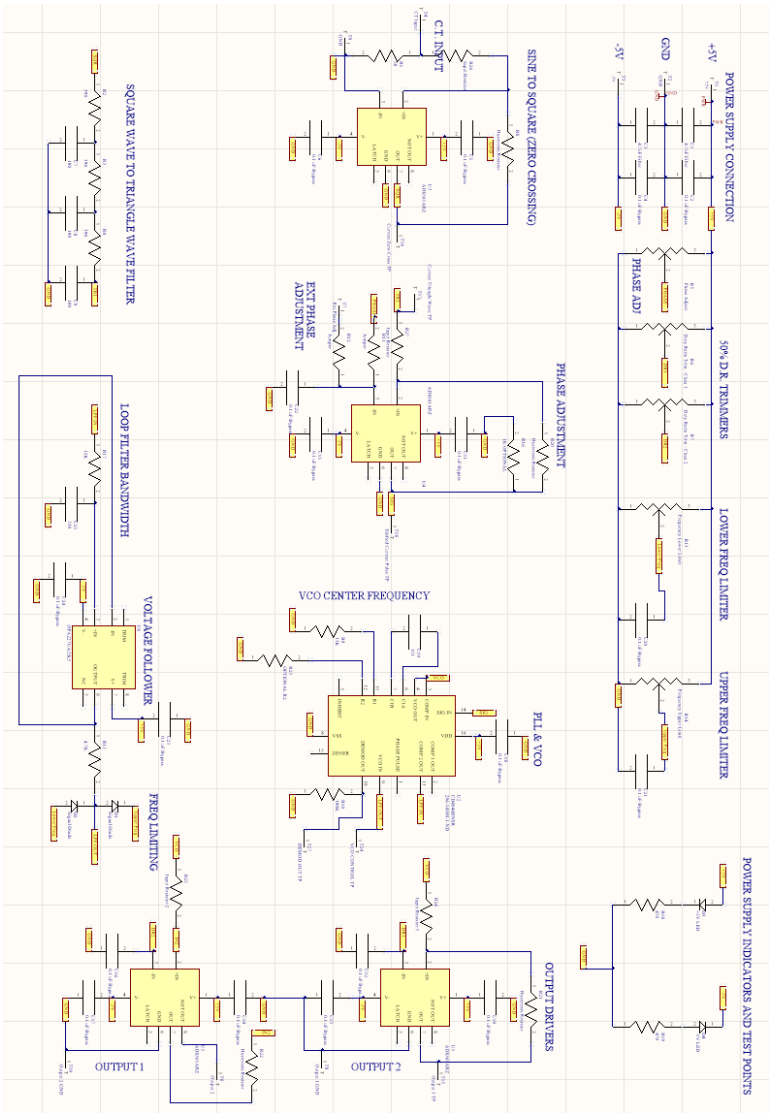

Current Sensing Input Comparator

The input comparator measures the signal voltage created across the 50 ohm input resistor by the tank current transformer. By comparing to zero (ground reference) the current sine wave is converted into a 50% duty ratio square wave.

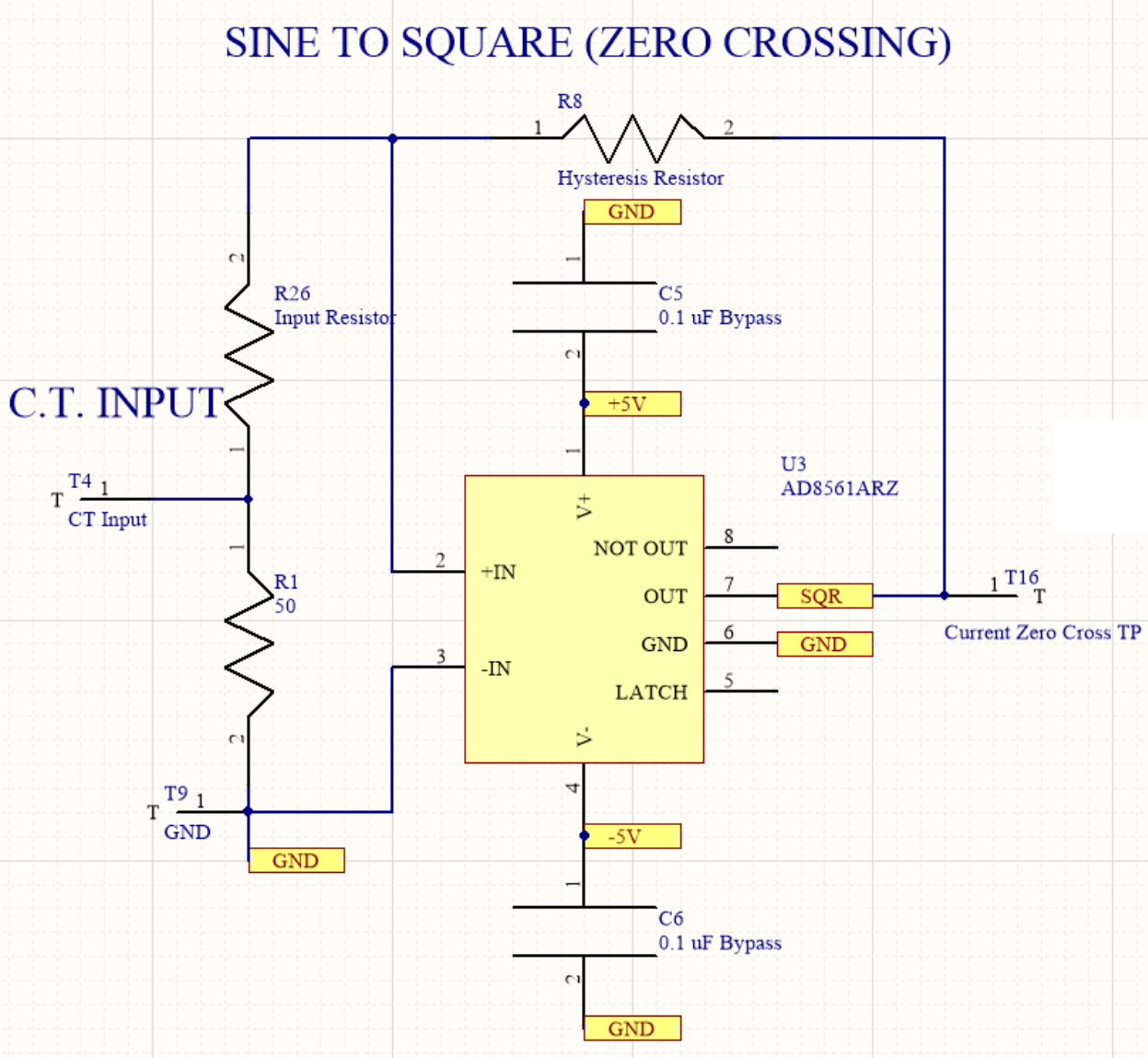

Square Wave to Triangle Wave Filter

Square wave from input comparator is fed into an RC-RC-RC filter, which outputs a triangle wave whose phase is tied to the phase of the measured current signal.

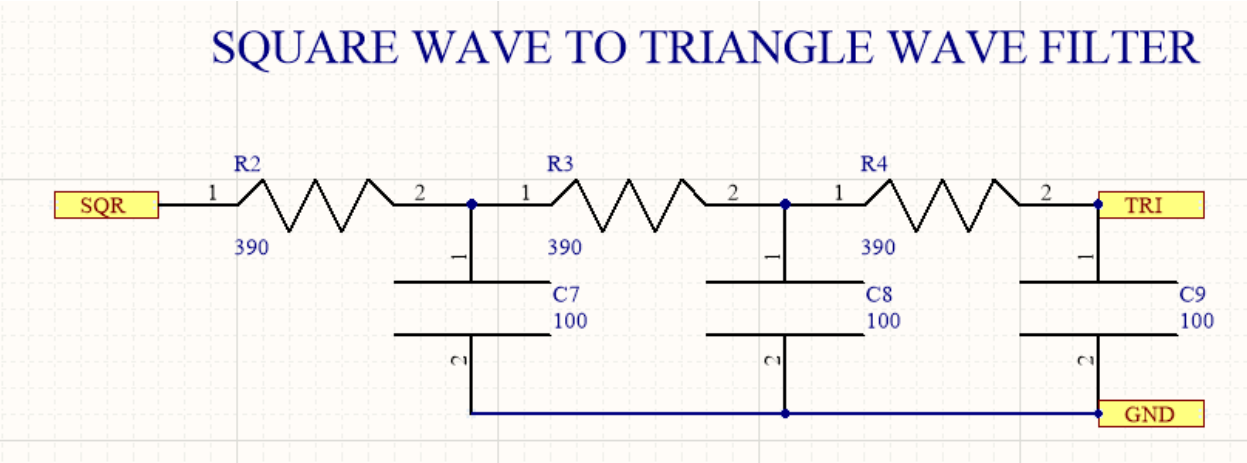

Phase Adjusting Triangle Wave Ramp Comparator

The triangle wave ramp is compared to an adjustable DC reference voltage by a second comparator. The phase between the output of the second comparator and the tank current is adjustable by varying the reference voltage. This reference voltage adjustment is the “Phase Adjustment” potentiometer which is the only manual control of the PLL.

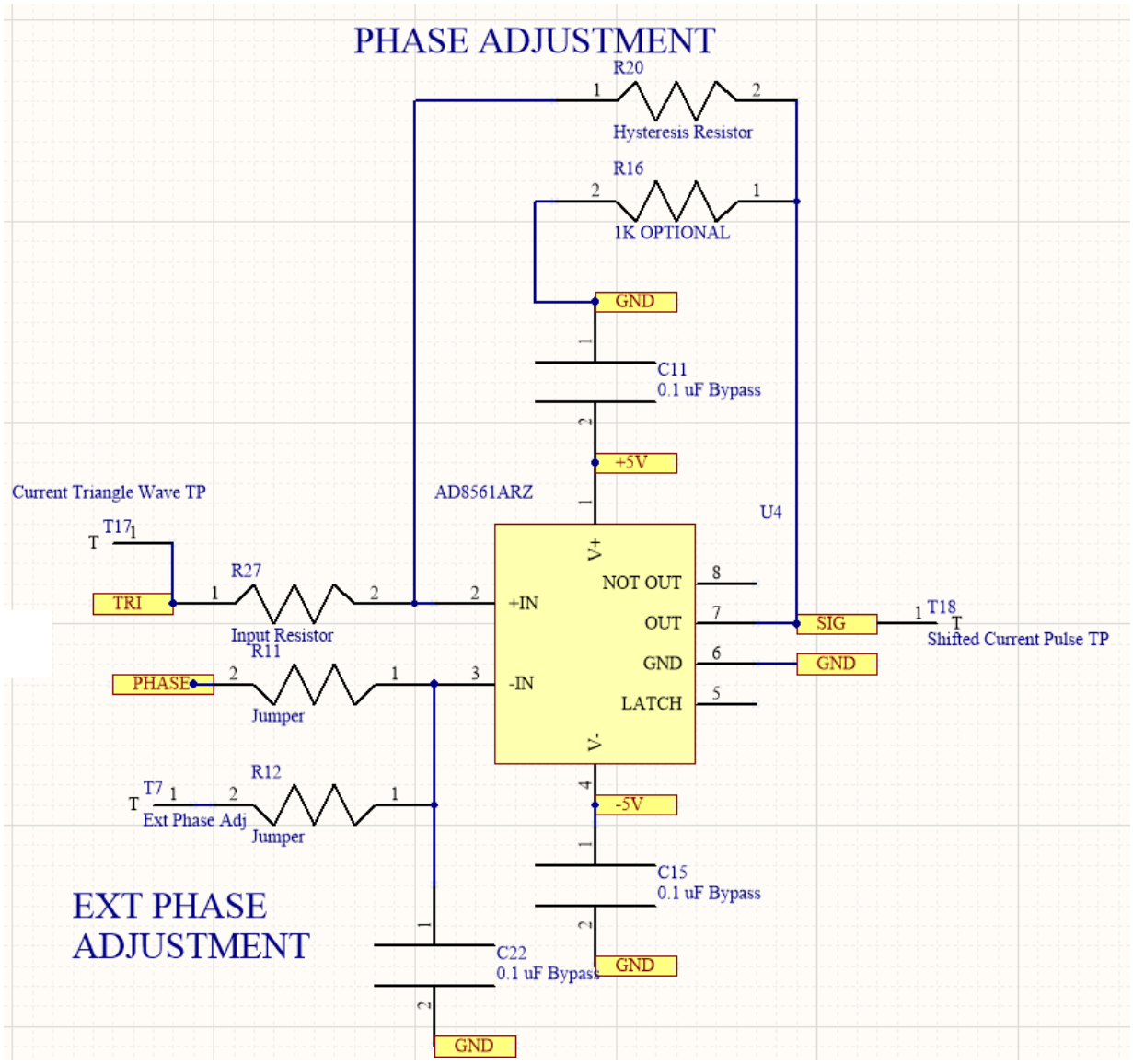

Phase Comparator and Voltage Controlled Oscillator

The PLL IC, type 4046, is the heart of the PLL gate controller. It contains both phase comparator and voltage controlled oscillator. It compares phase between its own output (feeding the inverter gates) and the output of the phase adjustment comparator.

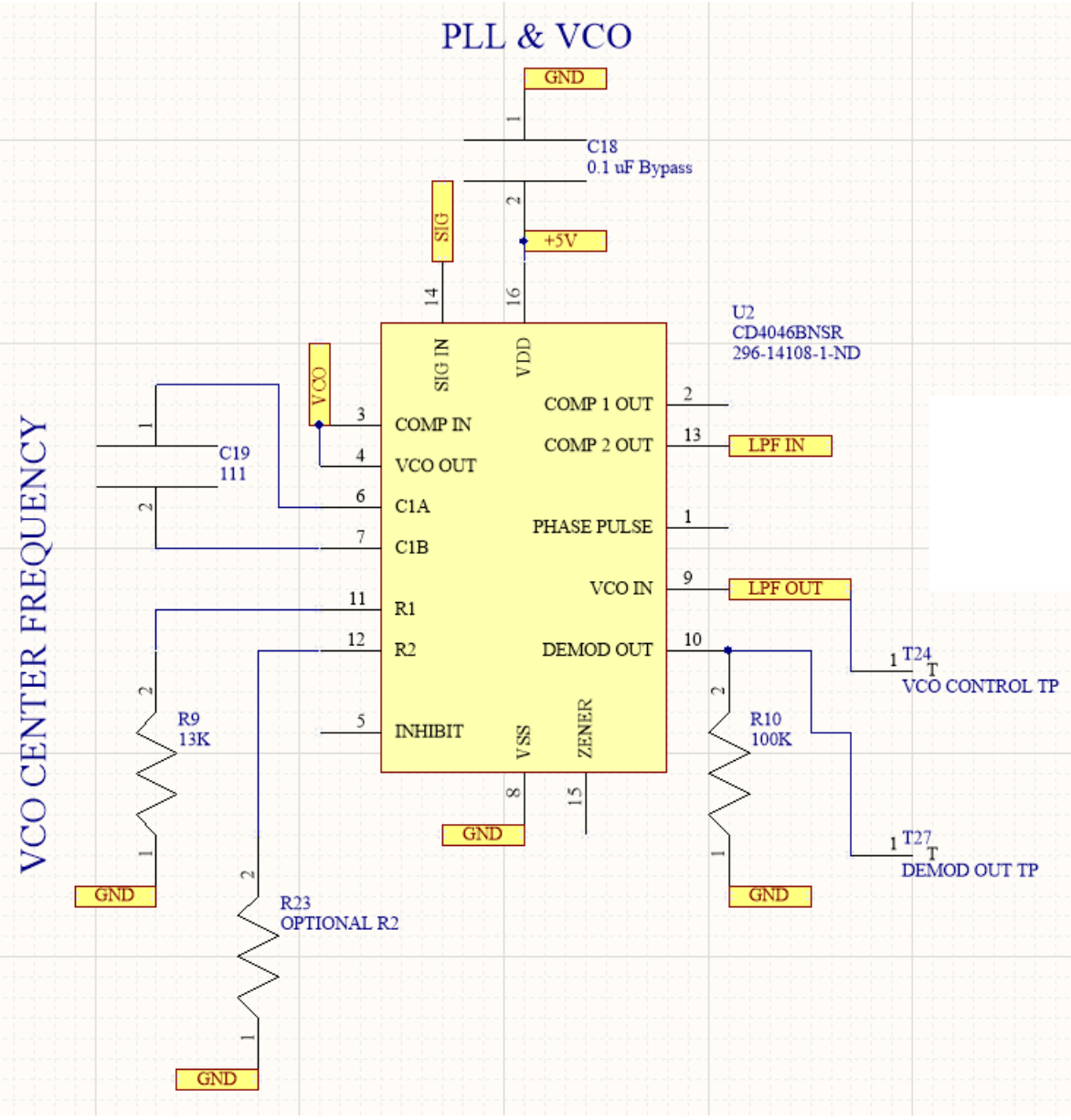

PLL Active Loop Filter

RC time constant of loop filter sets PLL bandwidth. Op Amp wired as voltage follower acts as a buffer between the passive filter and VCO input. The output voltage of the active filter is diode clamped between a pair of DC reference voltages, which set the upper and lower limits on VCO frequency.

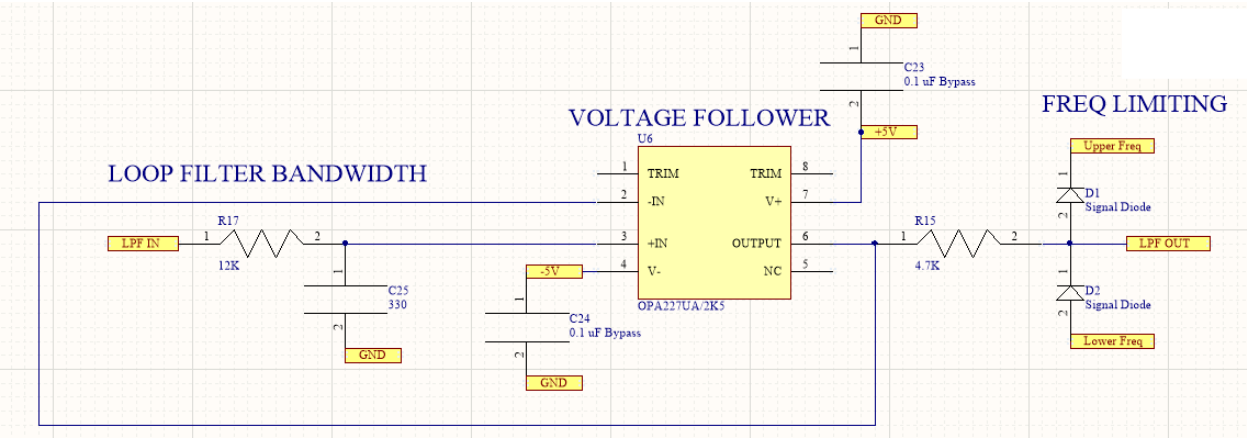

Output Buffers

The output square wave from the 4046 PLL VCO IC is sent to a pair of high speed comparators which provide signals to GaN inverter gate drivers

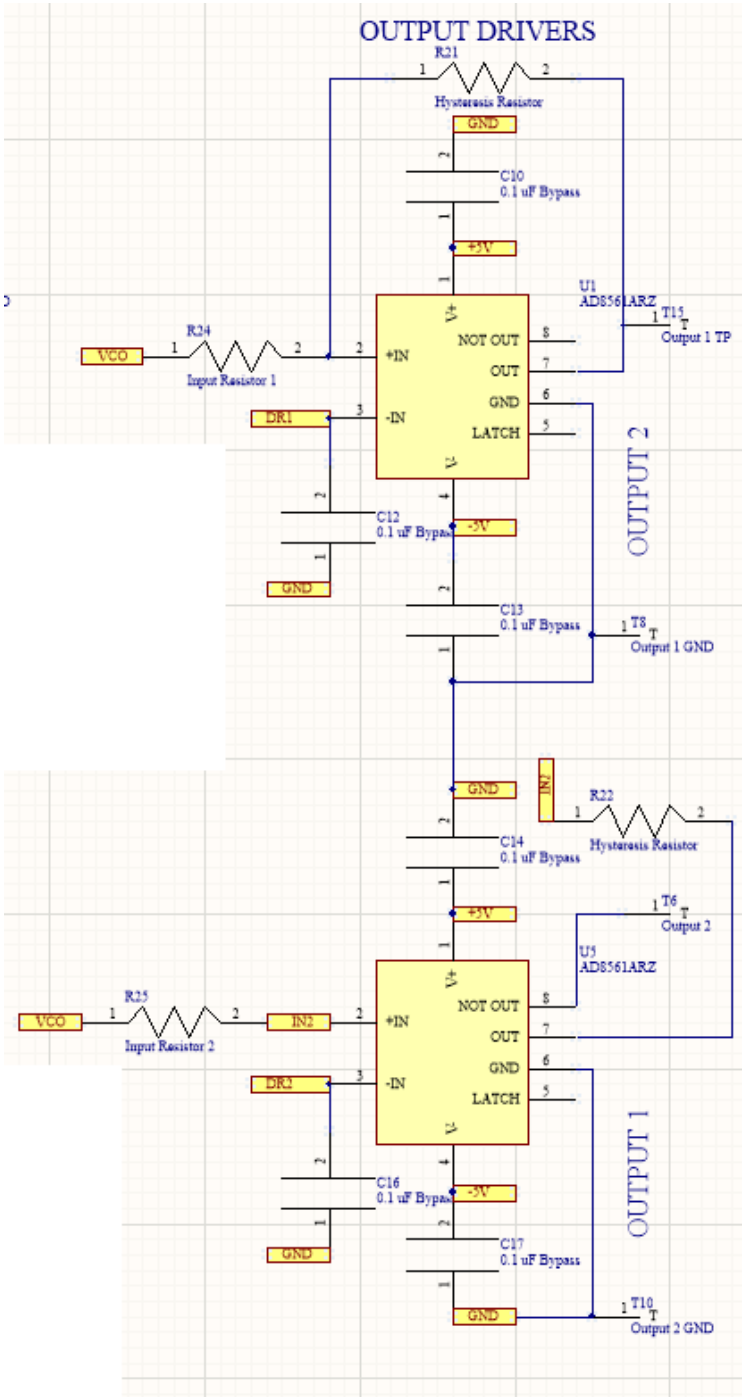

Appendix B – Rotor Electronics

The following is a schematic of the electronic circuitry located on the CPC rotor board. This circuit receives input AC from the coupling electrodes, and contains the high frequency rectifier, ceramic filter capacitor bank, and buck converter. Its DC output is connected to the WFSM field winding.

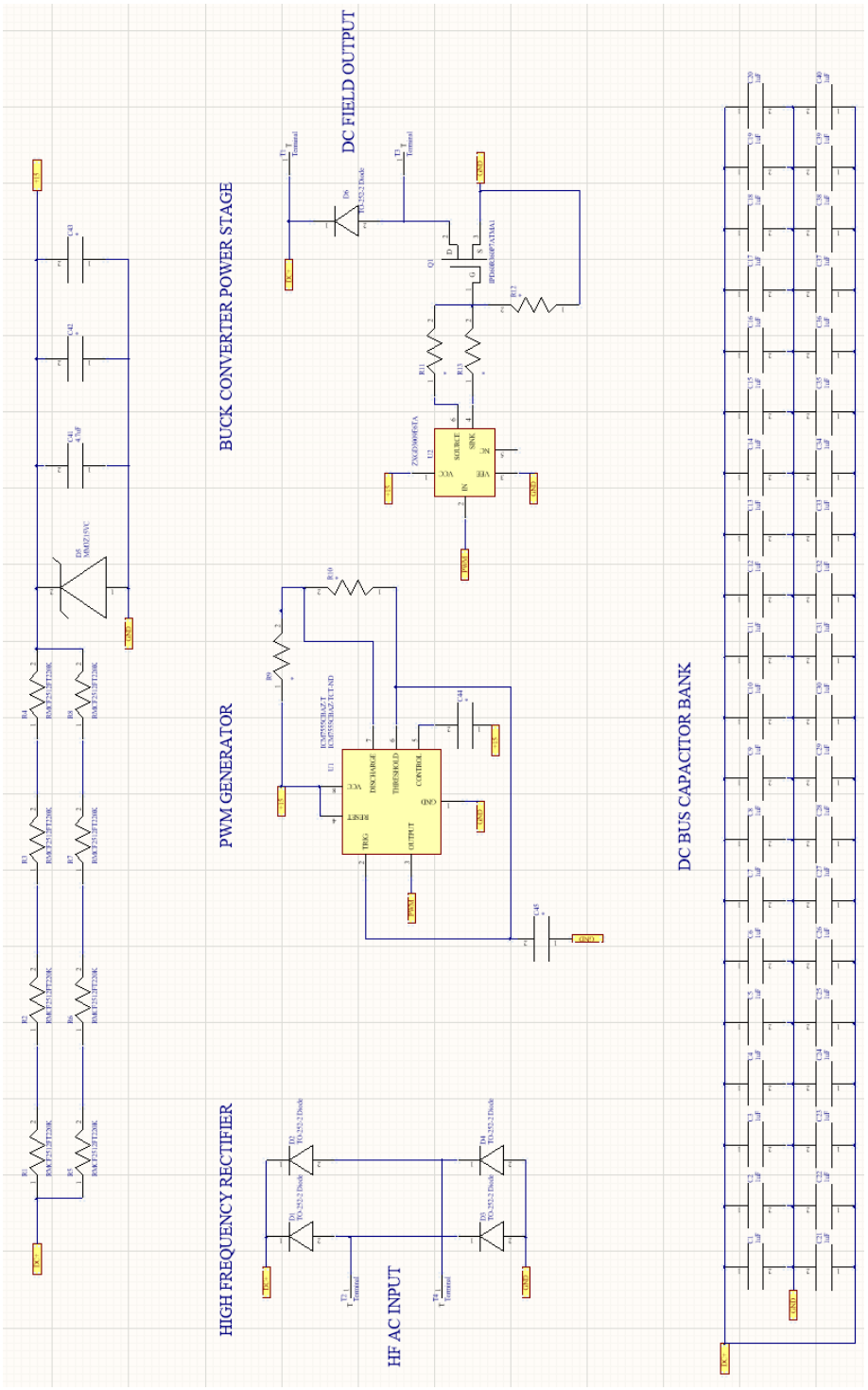
HIGH FREQUENCY RECTIFIER
BUCK CONVERTER POWER STAGE
PWM GENERATOR
DC FIELD OUTPUT
HF AC INPUT
DC BUS CAPACITOR BANK

High Frequency Rectifier

At the input to the rotor board is a silicon carbide diode full bridge, which rectifies AC from the coupler electrodes into DC on the 40uF filter capacitance (not shown).

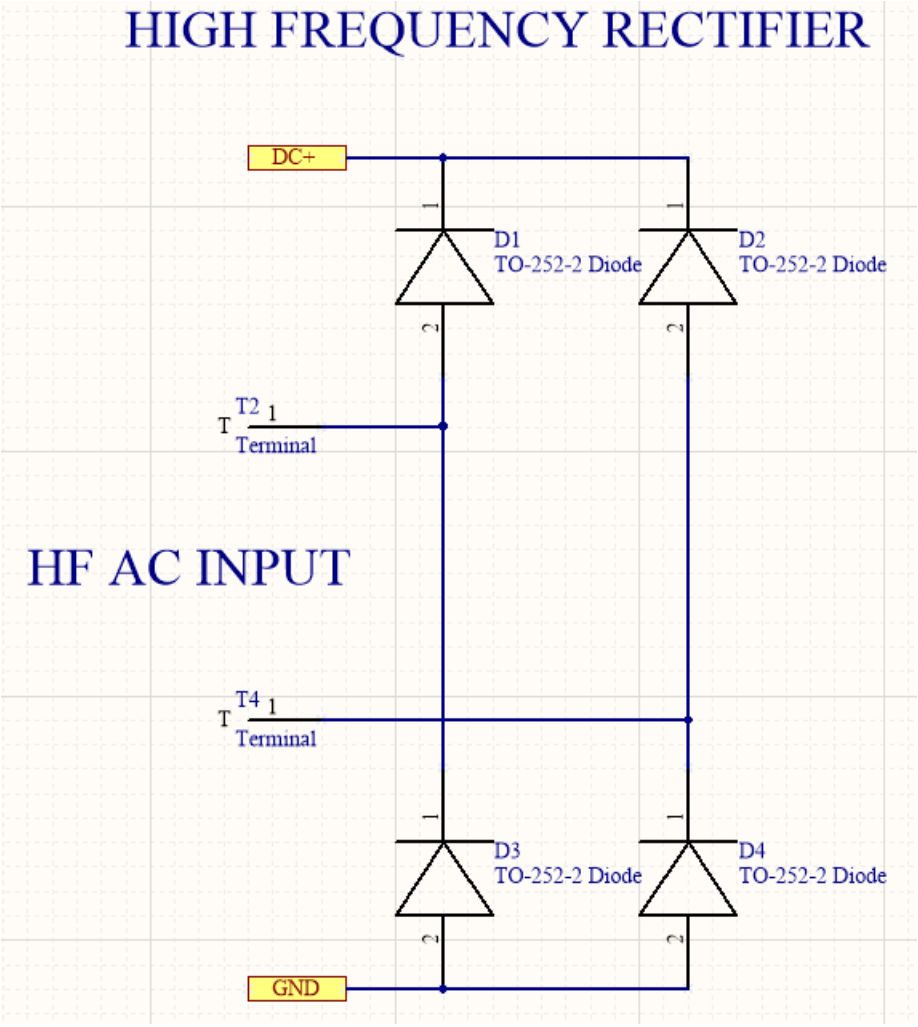

Buck Converter PWM Generator

The buck converter PWM signal is generated by a 555 timer IC, whose timing resistors and capacitor are configured for the desired frequency and duty ratio.

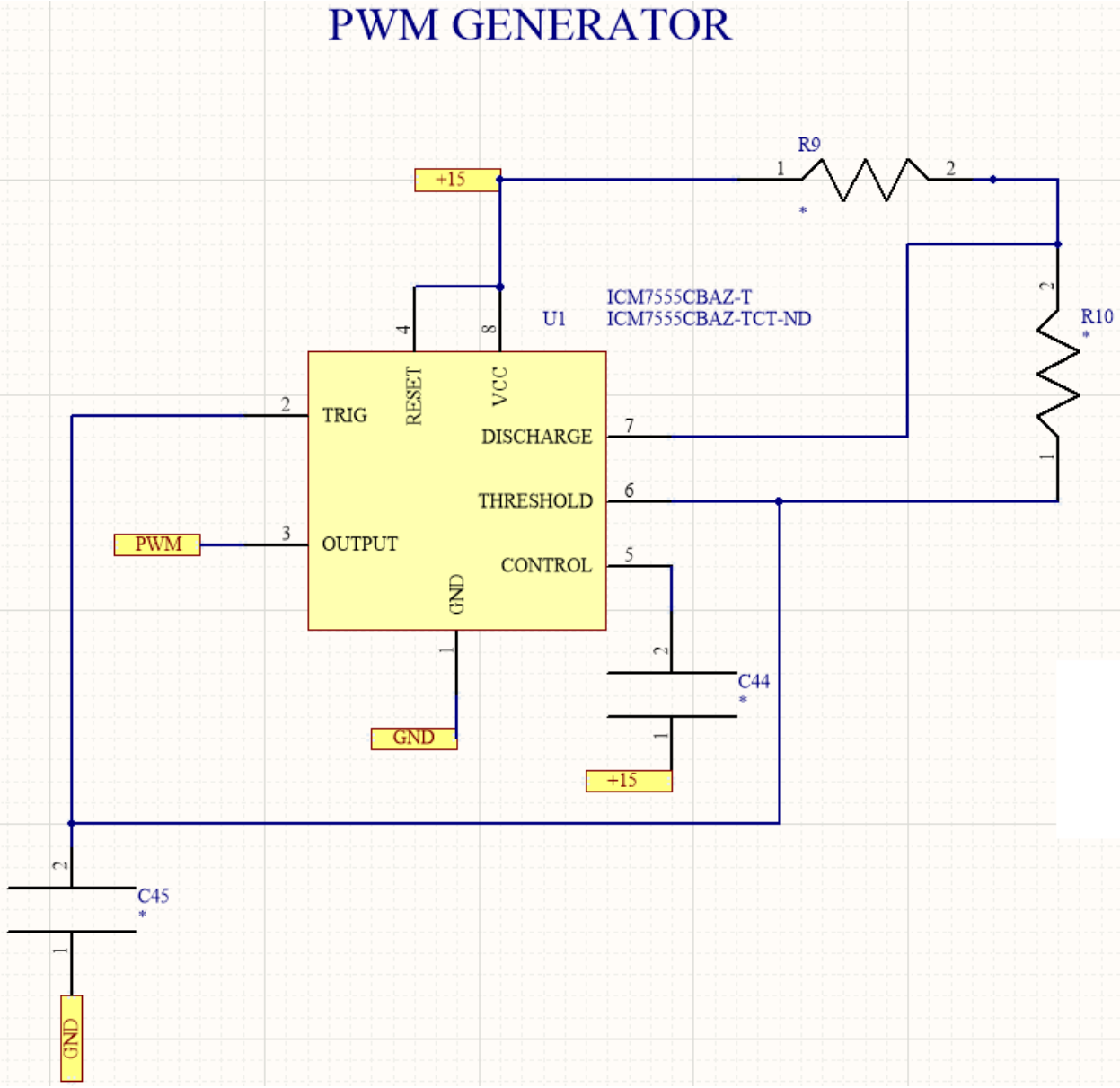

Buck Converter Power Stage

Finally, the PWM signal from the 555 oscillator is fed to a totem pole gate drive IC which drives the buck converter MOSFET.

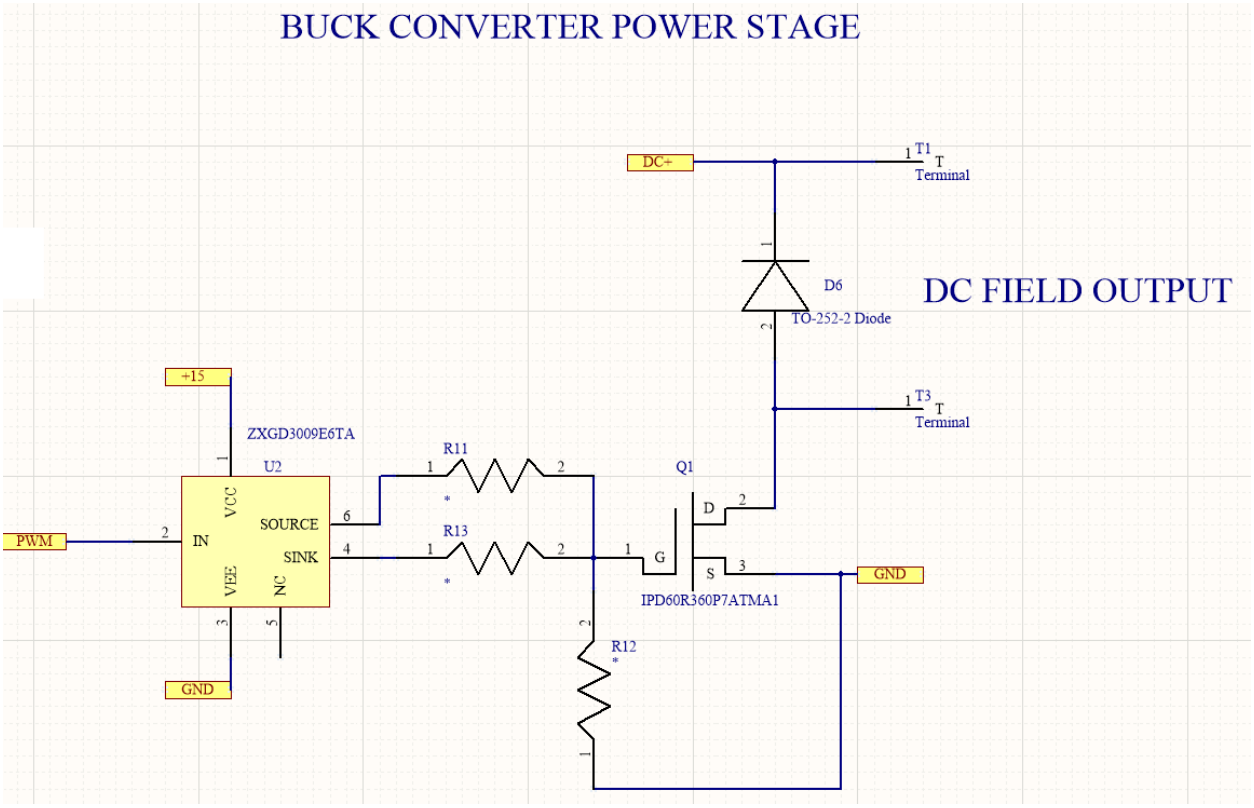

Bibliography

[1] D. C. Ludois, K. Hanson, and J. K. Reed, "Capacitive power transfer for slip ring replacement in wound field synchronous machines," in *IEEE Energy Conversion Congress and Exposition*, 2011, pp. 1664–1669.

[2] J. Dai, S. Hagen, D. Ludois, and I. Brown, "Synchronous Generator Field Excitation Via Capacitive Coupling Through a Journal Bearing," presented at the IEEE Energy Conversion Congress and Exposition (ECCE), 2016.

[3] D. C. Ludois, J. K. Reed, and K. Hanson, "Capacitive Power Transfer for Rotor Field Current in Synchronous Machines," *IEEE Trans. Power Electron.*, vol. 27, no. 11, pp. 4638–4645, Nov. 2012.

[4] R. D. Hall and R. P. Roberge, "Carbon brush performance on slip rings," in *Pulp and Paper Industry Technical Conference (PPIC), Conference Record of 2010 Annual*, 2010, pp. 1–6.

[5] "SLIP RINGS AND CARBON BRUSHES of synchronous generator," *Electrical Academia*, 18-Aug-2018. .

[6] J. K. Nøland, S. Nuzzo, A. Tessarolo, and E. F. Alves, "Excitation System Technologies for Wound-Field Synchronous Machines: Survey of Solutions and Evolving Trends," *IEEE Access*, vol. 7, pp. 109699–109718, 2019.

[7] D. R. Fenwick and W. F. Wright, "Review of trends in excitation systems and possible future developments," *Proc. Inst. Electr. Eng.*, vol. 123, no. 5, pp. 413–420, May 1976.

[8] N. Jiao, W. Liu, T. Meng, J. Peng, and S. Mao, "Design and Control of a Two-Phase Brushless Exciter for Aircraft Wound-Rotor Synchronous Starter/Generator in the Starting Mode," *IEEE Trans. Power Electron.*, vol. 31, no. 6, pp. 4452–4461, Jun. 2016.

[9] A. Griffo, R. Wrobel, P. H. Mellor, and J. M. Yon, "Design and Characterization of a Three-Phase Brushless Exciter for Aircraft Starter/Generator," *IEEE Trans. Ind. Appl.*, vol. 49, no. 5, pp. 2106–2115, Sep. 2013.

[10] W. F. Wright, R. Hawley, and J. L. Dinely, "Brushless Thyristor Excitation Systems.," *IEEE Trans. Power Appar. Syst.*, vol. PAS-91, no. 5, pp. 1848–1854, Sep. 1972.

[11] D. C. Aliprantis, S. D. Sudhoff, and B. T. Kuhn, "A brushless exciter model incorporating multiple rectifier modes and Preisach's hysteresis theory," *IEEE Trans. Energy Convers.*, vol. 21, no. 1, pp. 136–147, Mar. 2006.

[12] B. Sarlioglu and C. E. Huggett, "Method and system for providing single-phase excitation techniques to a start exciter in a starter/generator system," US6998726B2, 14-Feb-2006.

[13] C. Deng, G. Zhu, and R. D. Lorenz, "MHz frequencies, kW, 30 cm gap wireless power transfer with low air gap flux density and high efficiency using surface spiral winding coils," in *IEEE Applied Power Electronics Conference and Exposition (APEC)*, 2017, pp. 1606–1613.

[14] G. Zhu and R. D. Lorenz, “Achieving low magnetic flux density and low electric field intensity for an inductive wireless power transfer system,” in *IEEE Energy Conversion Congress and Exposition (ECCE)*, 2017, pp. 4022–4029.

[15] G. Zhu, A. Athavale, and R. D. Lorenz, “Methods to Reduce Air-Gap Center Region Magnetic and Electric Fields for Large Gap Inductive Wireless Power Transfer Systems,” in *IEEE Energy Conversion Congress and Exposition (ECCE)*, 2018, pp. 89–96.

[16] T. Diekhans and R. W. De Doncker, “A Dual-Side Controlled Inductive Power Transfer System Optimized for Large Coupling Factor Variations and Partial Load,” *IEEE Trans. Power Electron.*, vol. 30, no. 11, pp. 6320–6328, Nov. 2015.

[17] T. Shimonodan, H. Omori, N. Kimura, T. Morizane, and M. Nakaoka, “A novel type of large-gap WPT EV charging apparatus with a superimposed control signal communication,” in *IEEE PELS Workshop on Emerging Technologies: Wireless Power Transfer (WoW)*, 2017, pp. 1–6.

[18] J. Shin *et al.*, “Design and Implementation of Shaped Magnetic-Resonance-Based Wireless Power Transfer System for Roadway-Powered Moving Electric Vehicles,” *IEEE Trans. Ind. Electron.*, vol. 61, no. 3, pp. 1179–1192, Mar. 2014.

[19] B. Song *et al.*, “Design of a high power transfer pickup for on-line electric vehicle (OLEV),” in *IEEE International Electric Vehicle Conference*, 2012, pp. 1–4.

[20] A. Munir and B. T. Ranum, “Wireless power charging system for mobile device based on magnetic resonance coupling,” in *International Conference on Electrical Engineering and Informatics (ICEEI)*, 2015, pp. 221–224.

[21] L. Olvitz, D. Vinko, and T. Švedek, “Wireless power transfer for mobile phone charging device,” in *Proceedings of the 35th International Convention MIPRO*, 2012, pp. 141–145.

[22] J. Legranger, G. Friedrich, S. Vivier, and J. C. Mipo, “Comparison of Two Optimal Rotary Transformer Designs for Highly Constrained Applications,” in *IEEE International Electric Machines Drives Conference*, 2007, vol. 2, pp. 1546–1551.

[23] J. Liu and T. A. Lipo, “Synchronous machine field excitation utilizing a single phase matrix converter excited rotary transformer,” in *IEEE Energy Conversion Congress and Exposition (ECCE)*, 2017, pp. 1197–1204.

[24] H. Krupp and A. Mertens, “Rotary Transformer Design for Brushless Electrically Excited Synchronous Machines,” in *IEEE Vehicle Power and Propulsion Conference (VPPC)*, 2015, pp. 1–6.

[25] J. Legranger, G. Friedrich, S. Vivier, and J. C. Mipo, “Design of a Brushless Rotor Supply for a Wound Rotor Synchronous Machine for Integrated Starter Generator,” in *IEEE Vehicle Power and Propulsion Conference*, 2007, pp. 236–241.

[26] K. D. Papastergiou and D. E. Macpherson, “An Airborne Radar Power Supply With Contactless Transfer of Energy #x2014;Part I: Rotating Transformer,” *IEEE Trans. Ind. Electron.*, vol. 54, no. 5, pp. 2874–2884, Oct. 2007.

[27] C. Stancu, T. Ward, K. Rahman, R. Dawsey, and P. Savagian, “Separately excited synchronous motor with rotary transformer for hybrid vehicle application,” in *IEEE Energy Conversion Congress and Exposition (ECCE)*, 2014, pp. 5844–5851.

[28] G. Jawad, Q. Ali, T. A. Lipo, and B.-I. Kwon, "Novel Brushless Wound Rotor Synchronous Machine With Zero-Sequence Third-Harmonic Field Excitation," *IEEE Trans. Magn.*, vol. 52, no. 7, pp. 1–4, Jul. 2016.

[29] T. C. Martin and N. Tesla, *The Inventions, Researches and Writings of Nikola Tesla: With Special Reference to His Work in Polyphase Currents and High Potential Lighting*. Electrical Engineer, 1894.

[30] A. P. Hu, C. Liu, and H. L. Li, "A Novel Contactless Battery Charging System for Soccer Playing Robot," in *15th International Conference on Mechatronics and Machine Vision in Practice*, 2008, pp. 646–650.

[31] J. Dai and D. C. Ludois, "A Survey of Wireless Power Transfer and a Critical Comparison of Inductive and Capacitive Coupling for Small Gap Applications," *IEEE Trans. Power Electron.*, vol. 30, no. 11, pp. 6017–6029, Nov. 2015.

[32] Dai, Jiejian, "Power Electronics Design for High Power Capacitive Power Transfer," PhD Thesis, University of Wisconsin - Madison, 2017.

[33] B. Regensburger, A. Kumar, S. Sinha, J. Xu, and K. K. Afridi, "High-Efficiency High-Power-Transfer-Density Capacitive Wireless Power Transfer System for Electric Vehicle Charging Utilizing Semi-Toroidal Interleaved-Foil Coupled Inductors," in *IEEE Applied Power Electronics Conference and Exposition (APEC)*, 2019, pp. 1533–1538.

[34] B. Regensburger, A. Kumar, S. Sinha, and K. Afridi, "High-Performance 13.56-MHz Large Air-Gap Capacitive Wireless Power Transfer System for Electric Vehicle Charging," in *IEEE 19th Workshop on Control and Modeling for Power Electronics (COMPEL)*, 2018, pp. 1–4.

[35] F. Lu, H. Zhang, H. Hofmann, and C. Mi, "A CLLC-compensated high power and large air-gap capacitive power transfer system for electric vehicle charging applications," in *IEEE Applied Power Electronics Conference and Exposition (APEC)*, 2016, pp. 1721–1725.

[36] T. M. Mostafa, D. Bui, A. Muharam, R. Hattori, and A. P. Hu, "Capacitive Power Transfer System with Reduced Voltage Stress and Sensitivity," *Appl. Sci.*, vol. 8, no. 7, p. 1131, Jul. 2018.

[37] B. G. P. Harnwell, *Principles of Electricity and Electromagnetism*. McGraw-Hill Interamericana, 1949.

[38] B. Ge, D. C. Ludois, and R. Perez, "The use of dielectric coatings in capacitive power transfer systems," in *IEEE Energy Conversion Congress and Exposition (ECCE)*, 2014, pp. 2193–2199.

[39] J. Dai, S. Hagen, and D. Ludois, "Linear Motion System Cable Elimination Via Multiphase Capacitive Power Transfer Through Sliding Journal Bearings," presented at the IEEE Applied Power Electronics Conference (APEC), 2017.

[40] B. Regensburger, A. Kumar, S. Sinha, and K. K. Afridi, "Impact of Foreign Objects on the Performance of Capacitive Wireless Charging Systems for Electric Vehicles," in *IEEE Transportation Electrification Conference and Expo (ITEC)*, 2018, pp. 892–897.

[41] B. Regensburger *et al.*, "High-performance large air-gap capacitive wireless power transfer system for electric vehicle charging," in *2017 Transportation Electrification Conference and Expo (ITEC)*, 2017, pp. 638–643.

[42] H. Zhang, F. Lu, H. Hofmann, W. Liu, and C. Mi, “A large air-gap capacitive power transfer system with a 4-plate capacitive coupler structure for electric vehicle charging applications,” in *IEEE Applied Power Electronics Conference and Exposition (APEC)*, 2016, pp. 1726–1730.

[43] B. Regensburger, S. Sinha, A. Kumar, J. Vance, Z. Popovic, and K. K. Afridi, “Kilowatt-scale large air-gap multi-modular capacitive wireless power transfer system for electric vehicle charging,” in *IEEE Applied Power Electronics Conference and Exposition (APEC)*, 2018, pp. 666–671.

[44] A. Kumar, S. Pervaiz, Chieh-Kai Chang, S. Korhummel, Z. Popovic, and K. K. Afridi, “Investigation of power transfer density enhancement in large air-gap capacitive wireless power transfer systems,” in *IEEE Wireless Power Transfer Conference (WPTC)*, 2015, pp. 1–4.

[45] S. Sinha, B. Regensburger, K. Doubleday, A. Kumar, S. Pervaiz, and K. K. Afridi, “High-power-transfer-density capacitive wireless power transfer system for electric vehicle charging,” in *IEEE Energy Conversion Congress and Exposition (ECCE)*, 2017, pp. 967–974.

[46] N. Q. Atiyah, D. C. Atilla, C. Aydin, and Y. A. Mukhlif, “The Analysis of Variation in Plate Geometry for Capacitive Power Transfer Pads Utilized in Electric Vehicles,” in *2018 18th Mediterranean Microwave Symposium (MMS)*, 2018, pp. 291–294.

[47] H. Zhang, F. Lu, H. Hofmann, W. Liu, and C. C. Mi, “Six-Plate Capacitive Coupler to Reduce Electric Field Emission in Large Air-Gap Capacitive Power Transfer,” *IEEE Trans. Power Electron.*, vol. 33, no. 1, pp. 665–675, Jan. 2018.

[48] D. Rozario, V. K. Pathipati, A. Ram, N. A. Azeez, and S. S. Williamson, “Modified resonant converters for contactless capacitive power transfer systems used in EV charging applications,” in *IECON - 42nd Annual Conference of the IEEE Industrial Electronics Society*, 2016, pp. 4510–4517.

[49] C. Li, X. Zhao, C. Liao, and L. Wang, “A graphical analysis on compensation designs of large-gap CPT systems for EV charging applications,” *CES Trans. Electr. Mach. Syst.*, vol. 2, no. 2, pp. 232–242, Jun. 2018.

[50] S. Sinha, A. Kumar, B. Regensburger, and K. K. Afridi, “A New Design Approach to Mitigating the Effect of Parasitics in Capacitive Wireless Power Transfer Systems for Electric Vehicle Charging,” *IEEE Trans. Transp. Electrification*, pp. 1–1, 2019.

[51] H. Zhang, C. Zhu, and F. Lu, “Long-Distance and High-Power Capacitive Power Transfer based on the Double-Sided LC Compensation: Analysis and Design,” in *IEEE Transportation Electrification Conference and Expo (ITEC)*, 2019, pp. 1–5.

[52] R. Narayanamoorthi, “Modeling of Capacitive Resonant Wireless Power and Data Transfer to Deep Biomedical Implants,” *IEEE Trans. Compon. Packag. Manuf. Technol.*, vol. 9, no. 7, pp. 1253–1263, Jul. 2019.

[53] H. Zhang, F. Lu, H. Hofmann, and C. Mi, “An LC compensated electric field repeater for long distance capacitive power transfer,” in *IEEE Energy Conversion Congress and Exposition (ECCE)*, 2016, pp. 1–5.

[54] S. Hagen, "Capacitive Power Transfer Through Rotational and Sliding Bearings," M.S. Thesis, University of Wisconsin - Madison, Madison, WI, 2016.

[55] C. Liu, A. P. Hu, and N. K. C. Nair, "Coupling study of a rotary Capacitive Power Transfer system," in *IEEE International Conference on Industrial Technology, 2009. ICIT 2009*, 2009, pp. 1–6.

[56] F. Lu, H. Zhang, H. Hofmann, and C. C. Mi, "An Inductive and Capacitive Integrated Coupler and Its LCL Compensation Circuit Design for Wireless Power Transfer," *IEEE Trans. Ind. Appl.*, vol. 53, no. 5, pp. 4903–4913, Sep. 2017.

[57] F. Lu, H. Zhang, H. Hofmann, and C. C. Mi, "An Inductive and Capacitive Combined Wireless Power Transfer System WithLC-Compensated Topology," *IEEE Trans. Power Electron.*, vol. 31, no. 12, pp. 8471–8482, Dec. 2016.

[58] J. Dai and D. C. Ludois, "Capacitive Power Transfer Through a Conformal Bumper for Electric Vehicle Charging," *IEEE J. Emerg. Sel. Top. Power Electron.*, vol. 4, no. 3, pp. 1015–1025, Sep. 2016.

[59] T. M. Mostafa, A. Muharam, and R. Hattori, "Wireless battery charging system for drones via capacitive power transfer," in *IEEE PELS Workshop on Emerging Technologies: Wireless Power Transfer (WoW)*, 2017, pp. 1–6.

[60] D. C. Ludois, J. Reed, and M. Erickson, "Aerodynamic fluid bearings for capacitive power transfer and rotating machinery," in *IEEE Energy Conversion Congress and Exposition (ECCE)*, 2012, pp. 1932–1937.

[61] D. C. Ludois, M. J. Erickson, and J. K. Reed, "Aerodynamic Fluid Bearings for Translational and Rotating Capacitors in Noncontact Capacitive Power Transfer Systems," *IEEE Trans. Ind. Appl.*, vol. 50, no. 2, pp. 1025–1033, Mar. 2014.

[62] Di Gioia, Antonio *et al.*, "Design and Demonstration of a Wound Field Synchronous Machine for Electric Vehicle Traction With Brushless Capacitive Field Excitation," *IEEE Trans. Ind. Appl.*, vol. 54, no. 2, pp. 1390–1403, Apr. 2018.

[63] R. Knippel, "Rotating Capacitors with Sprial Groove Features for Hydrodynamic Gap Maintenance in Power Conversion Systems," PhD Thesis, University of Wisconsin - Madison, Madison, WI.

[64] M. Kline, "Capacitive Power Transfer," M.S. Thesis, University of California - Berkeley, 2010.

[65] J. Dai and D. C. Ludois, "Biologically inspired coupling pixilation for position independence in capacitive power transfer surfaces," in *IEEE Applied Power Electronics Conference and Exposition (APEC)*, 2015, pp. 3276–3282.

[66] R. Knippel, "Printed Circuit Board Structural Properties and Spiral Groove Trace Conductors for Hydrodynamic Gap Maintenance in Axial Flux Rotating Machines," presented at the IEEE Energy Conversion Congress and Exposition, Baltimore, MD, 2019.

[67] "Parylene Information Sheets." Cornell.

[68] "Parylene 101." Diamond MT, 2001.

[69] S. Hagen, R. Knippel, J. Dai, and D. C. Ludois, “Capacitive coupling through a hydrodynamic journal bearing to power rotating electrical loads without contact,” in *IEEE Wireless Power Transfer Conference (WPTC)*, 2015, pp. 1–4.

[70] Keysight Technologies, *Keysight 16451B Dielectric Test Fixture Operation and Service Manual*, Fifth. 2000.

[71] W. B. Boast, *Principles of electric and magnetic fields*, 2nd edition. Harper, 1956.

[72] R. S. Yang, A. J. Hanson, D. J. Perreault, and C. R. Sullivan, “A low-loss inductor structure and design guidelines for high-frequency applications,” in *IEEE Applied Power Electronics Conference and Exposition (APEC)*, 2018, pp. 579–586.

[73] “G3YNH info: Current transformers. Part 1.” [Online]. Available: http://g3ynh.info/zdocs/bridges/Xformers/part_1.html. [Accessed: 20-Nov-2019].

[74] “Power Electronics solutions for Ceramic Capacitors from Johanson Technology.” [Online]. Available: https://www.johansondielectrics.com/. [Accessed: 20-Nov-2019].

[75] J. Dai, S. S. Hagen, and D. C. Ludois, “High-Efficiency Multiphase Capacitive Power Transfer in Sliding Carriages With Closed-Loop Burst-Mode Current Control,” *IEEE J. Emerg. Sel. Top. Power Electron.*, vol. 7, no. 2, pp. 1388–1398, Jun. 2019.